INTERPLAY BETWEEN CHEMICAL AND MAGNETIC DISORDER IN SELECTED ALLOYS CLOSE TO A FERROMAGNETIC QUANTUM PHASE TRANSITION

A dissertation submitted to
Kent State University in partial
fulfillment of the requirements for the
degree of Doctor of Philosophy

by
Adane Samuel Gebretsadik

August, 2018

© Copyright
All rights reserved
Except for previously published materials

Dissertation written by

Adane Samuel Gebretsadik

B.Sc., Addis Ababa University, 2000

M.Sc., Addis Ababa University, 2003

M.Sc., Royal Institute of Technology & Ghent University, 2009

M.A., Kent State University, 2013

Ph.D., Kent State University, 2018

Approved by

_____, Chair, Doctoral Dissertation Committee
Dr. Almut Schroeder

_____, Members, Doctoral Dissertation Committee
Dr. Carmen Almasan

_____
Dr. Maxim Dzero

_____
Dr. Robert J. Twieg

_____
Dr. Mietek Jaroniec

Accepted by

_____, Chair, Department of Physics
Dr. James T. Gleeson

_____, Dean, College of Arts and Sciences
Dr. James L. Blank

Table of Contents

List of Figures vi

List of Tables xiii

Acknowledgments xv

1 **Introduction** 1

1.1 Magnetic properties of d- and f-metals 3

1.2 Quantum phase transitions 7

1.3 Impact of disorder on quantum phase transition 11

1.4 Fermi liquid and non-Fermi liquid behavior 15

1.5 Specifics of target systems 17

1.5.1 $Ni_{1-x}V_x$ 17

1.5.2 $CePd_{1-x}Rh_x$ and $CePt_{1-x}Rh_x$ 21

2 **Experimental methods** 23

2.1 Sample growth 24

2.2 X-ray powder diffraction 27

2.3 Neutron scattering 30

2.4 Atomic pair distribution function (PDF) 34

2.5 Magnetic ac-susceptibility 37

2.6 Muon spin rotation (μSR) 39

2.6.1 Muon production, decay, and polarization 40

2.6.2 Evolution of the muon spin and principles of the μSR experiment 40

3 **Structural study of Ni-V using PDF method** 44

3.1 Random atomic distribution model 46

3.2 Alternative cluster and super structure models 48

3.3 Discussion 52

4 **Magnetic clusters in Ni-V** 53

4.1 Magnetization study of quantum Griffiths phase 54

4.2 μSR study of quantum Griffiths phase 55

4.2.1 Results of $x = 10\%$ 57

4.2.2 Results of $x = 11\%$ 58

4.3 SANS results 61

4.4 Discussion 63

5 **Structural and magnetic study of CeRh-alloys** 65

5.1 Magnetic ac-susceptibility 65

5.2 Structure analysis with EXPGUI 67

5.3 Structure of minority phases $Ce(Pt_{1-x}Rh_x)_2$ and Ce_3Pd_4 71

5.4 PDF analysis of $CePt_{1-x}Rh_x$ using PDFgui 73

5.5 The lattice parameters of $CePt_{1-x}Rh_x$ 76

5.6 PDF analysis of $CePd_{1-x}Rh_x$ using PDFgui 79

5.7 The lattice parameters of $CePd_{1-x}Rh_x$ 81

5.8 Discussion 83

6 **Origin of disorder in ferromagnetic CeRh-alloys** 85

6.1 Investigation of the local Ce-environment 85

6.2 Discussion 91

7 **Summary and outlook** 94

A **Important instrument and lattice parameters** 98

A.1 NOMAD specifications 98

A.2 Lattice parameters of second phase $Ce(Pt_{1-x}Rh_x)_2$ 99

A.3 Lattice parameters of second phase Ce_3Pd_4 99

A.4 Periodic table of selected metallic elements 100

References 101

List of Figures

1.1 Doniach's generic phase diagram for the phase transition between an RKKY induced magnetically ordered phase and the Kondo screened, paramagnetic phase as a function of the local exchange-coupling parameter J. 5

1.2 Generic phase diagram of a QPT in the vicinity of a quantum critical point (QCP) located at r_c, where r is a tuning parameter changing interaction. The solid line marks the finite- temperature boundary between the ordered and disordered phases and the dashed lines indicate the boundaries of the quantum critical region. 10

1.3 (a) Sketch of diluted magnet with rare region devoid of impurity. Different schematic QPT scenario for quenched disorder showing (b) infinite randomness critical point with a quantum Griffiths regime expected for Heisenberg symmetry and (c) a cluster glass phase expected for Ising symmetry. 13

1.4 (a) Low-field susceptibility of $Ni_{1-x}V_x$ versus temperature T and (b) low temperature magnetization versus magnetic field H. Dotted lines indicate power laws for $T > 10$K and $H > 3000$G in (a) and (b), respectively. Solid lines (shown for $x > 0.12$) represent fits to a model that includes fluctuating and frozen clusters. From Ref. [1]. 18

1.5 Phase diagram of $Ni_{1-x}V_x$ showing paramagnetic (PM), ferromagnetic (FM), and cluster glass (CG) phases. The ferromagnetic transition temperature, T_C, is determined from different methods indicated. . . 19

2.1 Reduced X-ray powder diffraction data for (a) CePt, (b) $CePt_{0.8}Rh_{0.2}$, (c) $CePt_{0.2}Rh_{0.8}$, and (d) $CePd_{0.2}Rh_{0.8}$. The black peak in (a) is the (111) peak from silicon powder sample for calibration. Data collected using Cu-Kα source with $\lambda = 1.5418\mathring{A}$. 30

2.2 PDF of a fcc-lattice. 35

2.3 (a) Schematic diagram of a μSR experiment. A spin-polarized beam of muons is implanted in a sample. After decay, positrons are detected in either a forward (F) or backward (B) detector. (b) The asymmetry $A(t)$ vs time for a uniform magnetic field showing single frequency precession. (c) Muon spin precession in a local magnetic field. 41

3.1 Chemical and magnetic phase diagram of Ni-V. 45

3.2 PDF of $Ni_{0.85}V_{0.15}$ taken at 300K on NOMAD with random fit, the difference Δ = data-fit is shown shifted down by 6 units with $Q_{damp} = 0.033\mathring{A}^{-1}$ and $Q_{broad} = 0.04\mathring{A}^{-1}$. 46

3.3 Comparison of V-cluster model (green) with random model (red) of local PDF. $Ni_{0.85}V_{0.15}$ data (open symbol), models and difference (solid line) are shown. The upper right corner shows the V38 cluster model. 50

3.4 Comparison of different ordered phases, Ni_3V model (black) and Ni_8V model (orange) of local PDF. $Ni_{0.85}V_{0.15}$ powder data (open symbol), models, and differences (solid lines) are shown. On the right side, the structure of Ni_3V and Ni_8V are shown. 51

4.1 Random model of $Ni_{0.89}V_{0.11}$ on fcc lattice with magnetic Ni (blue dots), V (red dots), and "nonmagnetic" Ni if adjacent to V (white space). Green circle marks a magnetic cluster. 53

4.2 Red symbols represent exponents α obtained from low temperature magnetization in the FM phase. Green symbols show exponents α from power laws fit using the magnetization data and open symbols indicate exponents obtained from susceptibility, both in the PM phase. Solid line indicates fit to model $\alpha(x) \sim |x - x_c|^{\nu\psi}$, with $\nu\psi = 0.34$ and $x_c = 11.6\%$. From Ref. [2]. 55

4.3 Zero-field μSR asymmetry $A(t)$ vs time of $Ni_{1-x}V_x$ for several V concentrations x indicated. Symbols represent data taken at low temperatures ($1.5K < T < 10K$). Solid lines represent fits to selected models. Each data is shifted by a constant C to avoid any overlap. From Ref. [3]. 56

4.4 (a) Zero-field μSR asymmetry $A(t)$ vs time of $Ni_{1-x}V_x$ for $x = 10\%$. Symbols represent data taken at several temperatures. Solid lines represent fits to Eq. 4.2. (b) Evolution of amplitudes of the FM component (A_{FM}) and the PM component (A_{PM}) as a function of temperature T. From Ref. [2]. 58

4.5 (a) Zero-field μSR asymmetry $A(t)$ vs time of $Ni_{1-x}V_x$ for $x = 11\%$. Symbols represent data taken at several temperatures. Solid lines represent fits of the form in Eq. 4.4 (b) Evolution of amplitudes of the FM component A_{FM} (blue symbols) and the PM component A_{PM} (red symbols) as a function of temperature T. From Ref. [2]. 59

4.6 (a) Cluster fraction f_{cl} vs x from magnetization and μSR analysis. (b) Relative width R vs x of the Gaussian-broadened Gaussian (GBG) model. From Ref. [2]. 60

4.7 SANS intensity I of Ni-V for $x = 11\%$ as a function of scattering vector Q measured at different temperatures $T_C = 7$K and $T = 1.5$K. For ΔI, data at $B = 5$T are subtracted as background. Data collected on GPSANS at HFIR, ORNL. 62

4.8 SANS intensity of $Ni_{1-x}V_x$ for $x = 10\%$ as a function of scattering vector Q measured at several temperatures. The high field data is subtracted as background. Data collected on GPSANS, ORNL (small circles) and on NG7 SANS, NIST (large circles). 63

5.1 Low temperature magnetic ac-susceptibility of (a) $CePt_{0.8}Rh_{0.2}$ and (b) $CePd_{0.8}Rh_{0.2}$ for different frequencies of the driving field $B < 0.01$G. 66

5.2 The CrB-type structure when viewed in different projections a) c-b plane b) c-a plane, and c) a-b plane. The blue spheres represent the Ce-atoms and the red spheres represent the Rh/Pt or Rh/Pd atoms on the shared sites. 68

5.3 Structure function S of $CePd_{1-x}Rh_x$ and $CePt_{1-x}Rh_x$ for selected Rh concentrations, $x = 0.2$ and $x = 0.8$, at 100K as a function of total time of flight (TOF) reduced with EXPGUI. The black symbols show data and the red line represents the Rietveld fit. The difference between data and fit is shown by a green solid line at the bottom. Blue arrows show additional peaks from the identified minority phases of $Ce(Pt_{1-x}Rh_x)_2$ and Ce_3Pd_4. 69

5.4 Structures of the minority phase (a) $Ce(Pt_{1-x}Rh_x)_2$ and (b) Ce_3Pd_4. Blue spheres show the Ce-atoms and the red spheres show (a) the Pt/Rh atoms and (b) the Pd/Rh atoms. 72

5.5 PDF of powder data of selected Pt-alloys at 100K on NOMAD with (a) single-phase fit & (b) two-phase fit for $CePt_{0.8}Rh_{0.2}$ and (c) single-phase fit & (d) two- phase fit for $CePt_{0.2}Rh_{0.8}$. The difference, Δ = data(blue symbols)-fit(red line), is shown by a wavy green line beneath the peaks with a black straight line showing the offset by 6 units. . . 73

5.6 The weighted residual factor (Rw) from PDF analysis of (a) $CePt_{1-x}Rh_x$ and (b) $CePd_{1-x}Rh_x$ in fit range $1.75\mathring{A} \leq r \leq 20\mathring{A}$ at 100K. The red symbols show single-phase fit with P_1 only, blue symbols show two-phase fit with P_1+P_2, where P_2 is $CeRh_2$-type phase, and green symbols show two-phase fit with P_2=Ce_3Pd_4. Open symbols include additional parameter spd. The fraction of the second phase (f_2) in (c) $CePt_{1-x}Rh_x$ and (d) $CePd_{1-x}Rh_x$ as a function of Rh concentration x. 75

5.7 Refined lattice parameters of $CePt_{1-x}Rh_x$ vs x at T = 100K (blue circles) and T = 259K (red circles) are shown. (a), (b), and (c) show the lattice constants a, b, and c, respectively. (d) presents the unit cell volume, V. 77

5.8 Refined parameters of $CePt_{1-x}Rh_x$ vs x at different temperatures, T = 100K (blue circles) and T= 259K (red circles): (a) and (b) show isotropic ADP of Ce, u_{Ce}, and of Rh/Pt site, u_{Rh}, respectively. (c) and (d) present the atomic position of Ce, y_{Ce}, and of the Rh/Pt site, y_{Rh}, respectively. 78

5.9 PDF of $CePd_{1-x}Rh_x$ at 100K with (a) single-phase fit & (b) two-phase fit of $CePd_{0.8}Rh_{0.2}$ and (c) single-phase fit & (d) two-phase fit of $CePd_{0.2}Rh_{0.8}$. The difference, Δ = data(blue symbols)-fit(red line), is shown by a wavy green line beneath the peaks with a black straight line showing the offset by 6 units. 80

5.10 Refined lattice parameters of $CePd_{1-x}Rh_x$ vs x at T = 100K (blue circles) and T = 259K (red circles). (a), (b), and (c) show the lattice parameters a, b, and c, respectively. (d) presents the unit cell volume, V 81

5.11 Refined parameters of $CePd_{1-x}Rh_x$ vs x at different temperatures, T = 100K (blue circles) and T = 289K (red circles). (a) and (b) show isotropic ADP of Ce, u_{Ce}, and of Rh/Pd site, u_{Rh}, respectively. (c) and (d) present the atomic position of Ce, y_{Ce}, and of the Rh/Pd site, y_{Rh}, respectively. 82

6.1 Variation of bond lengths between different pairs of atoms at 100K in (a) $CePd_{1-x}Rh_x$ and (b) $CePt_{1-x}Rh_x$. (c) displays the Ce-atom (yellow) and its seven nearest neighbors at different distances (different colors). 86

6.2 Isotropic ADP, u_{Rh} and u_{Ce} at 100K of $CePd_{1-x}Rh_x$ and $CePt_{1-x}Rh_x$ vs x, red line shows fit of $u_{Rh}(x)$ of Pt-samples. 89

6.3 PDF of data (blue circles) at 100K of $CeT_{0.2}Rh_{0.8}$ for (a) T=Pt and (b) T=Pd with fit range $2\mathring{A} \leq r \leq 5.6\mathring{A}$. The red lines show a model with two different Ce-environments $(P_1(x)+P_1(1))$ where $P_1(x)$ is $CeT_{0.2}Rh_{0.8}$ and $P_1(1)$ is CeRh. The two-phase fit (P_1+P_2) and the single-phase fit (P_1) are marked by a green and black lines, respectively, where P_1 is $CeT_{0.2}Rh_{0.8}$ and P_2 is $Ce(Pt_{0.2}Rh_{0.8})_2$ in (a) and $CeRh_2$ in (b). The differences, Δ = data-fit are shown below with the same color. 91

List of Tables

2.1 PDF refined fit parameters of $CePt_{0.2}Rh_{0.8}$ powder obtained on NOMAD at 289K with fit range $r_{max} = 20\mathring{A}$, results of $Q_{max} = 24\mathring{A}^{-1}$ compared with $Q_{max} = 30\mathring{A}^{-1}$. 33

3.1 PDF refined fit parameters of $Ni_{0.85}V_{0.15}$ powder obtained on NOMAD at 300K for fcc random model with fit range $r_{max} = 20\mathring{A}$, $Q_{damp} = 0.033\mathring{A}^{-1}$, and $Q_{broad} = 0.040\mathring{A}^{-1}$ compared with the results on pure Ni powder data with $Q_{damp} = 0.018\mathring{A}^{-1}$, and $Q_{broad} = 0.036\mathring{A}^{-1}$. The result for $x = 0$ is obtained from Ref. [4]. 47

3.2 Fit quality of different models describing the local pair correlations in $Ni_{0.85}V_{0.15}$ powder data set at 300K. The weighted residual factor Rw is listed for a fit range $1.75\mathring{A} < r < 7.1\mathring{A}$. 49

5.1 Comparison of Rietveld analysis refined fit parameters of (a) single-phase $CePd_{0.15}Rh_{0.85}$ powder data obtained on GEM at 300K at ISIS reported by Adroja et. al [5] and our $CePd_{0.2}Rh_{0.8}$ powder data obtained on NOMAD at 289K at SNS and (b) CePt powder data obtained at 15K reported by Gomez Sal et. al [6] and our $CePt_{0.8}Rh_{0.2}$ powder data obtained on NOMAD at 100K at SNS. 70

A.1 PDF refined fit parameters of $Ce(Pt_{1-x}Rh_x)_2$ data obtained on NOMAD at 100K with fit range $r_{max} = 20\mathring{A}$, $Q_{max} = 24\mathring{A}^{-1}$, $Q_{damp} \simeq 0.018\mathring{A}^{-1}$, and $Q_{broad} \simeq 0.02\mathring{A}^{-1}$ 99

A.2 PDF refined fit parameters of Ce_3Pd_4 data obtained on NOMAD at 100K with fit range $r_{max} = 20\mathring{A}$, $Q_{max} = 24\mathring{A}^{-1}$, $Q_{damp} \simeq 0.018\mathring{A}^{-1}$, and $Q_{broad} \simeq 0.02\mathring{A}^{-1}$. The second phase used for $x = 0.8$ is $CeRh_2$. . 99

Acknowledgments

First of all, I would like to thank almighty God for giving me the strength and all the necessary tools to complete this dissertation successfully. I would like to thank my advisor and mentor, Prof. Almut Schroeder, for all her unlimited and priceless support she has given me since the very first day I joined her group. This dissertation would not have been possible without her unreserved help, critical comments, and guidance. I enjoyed the educational discussions we had during our meeting and the unforgettable experience during our long trips to various national laboratories. Many thanks to Dr. J-Guy Lussier for his tremendous help I needed and for the enlightening discussions and critical comments after reading my dissertation. I wanted to thank Dr. Kate Page, Dr. Kathryn Krycka, and Dr. Lisa DeBeer-Schmitt for their help and great hospitality while I was conducting experiments at the national laboratories they are working. I would like to thank Prof. Carmen Almasan and Prof. Brett Ellman for giving me an unlimited access to their laboratory facilities. It would not have been easy for me to cut my rhodium slugs without Prof. Brett Ellman's diamond saw. Thanks to Mr. Larry Maurer for helping me seal the quartz tubes and for sharing his amazing life experience with me. Thanks to Greg Putman for ordering gases and for providing me technical assistance whenever I needed. Many thanks to Connie Reho, Kelly Conley, Deborah Davis, and all the administrative staffs of the physics department for their amazing hospitality and help during the course of this dissertation. Although they are in their retirement, I would like to extend my sincere gratitude to Loretta Hauser and Cindy Miller for their unforgettable hospitality and

help. Many thanks to Prof. Kean Declan for understanding my situation and for giving me the time I needed to write my dissertation while I was his teaching assistant. I wanted to thank my colleague Ruizhe Wang for sharing his laboratory experience and technical skills with me and for the useful discussions we had during our meeting. Last but not least, I would like to thank all my family for their love and support. I wanted to thank my mother, Atsede Masresha, for being always with me and making me the person who I am now. Many thanks to my sister, Mulu Gebretsadik, for her tremendous support and help all the time. I would not have made it without her priceless support. I wanted to thank my brother, Dr. Samuel Sitotaw, for his help and for making a huge impact on my life. Finally, I would like to dedicate this dissertation to the memory of my father, Samuel Gebretsadik, who passed away during the course of this dissertation. You are gone now but never forgotten. Your belief in my abilities has made me stronger. I will always miss you.

Chapter 1

Introduction

In recent years, quantum phase transitions (QPTs) that occur at zero temperature when a non-thermal parameter is varied, have become an attractive research field in condensed matter physics [7]. In particular, the study of magnetic QPTs in strongly correlated electron systems where a magnetic ordered phase can be continuously suppressed and finally destroyed at the quantum critical point (QCP) by varying pressure, chemical compositions, or magnetic field has been recognized as a promising route to unravel unconventional properties and find novel phases [7]. At low temperatures, quantum fluctuations accompanying magnetic QCPs compete with thermal fluctuations, and these quantum critical fluctuations can explain the unconventional properties in the neighborhood of conventional phases.

A normal metal can be described as a weakly interacting gas of Fermi particles called quasiparticles with a finite lifetime close to the Fermi energy, commonly known as Fermi liquid (FL) as first postulated by Landau [8]. Close to a magnetic QCP significant deviations called Non-Fermi liquid (NFL) properties are expected. Landau's FL picture has been successful in describing a wide range of systems including heavy fermion compounds (HFC), where the Coulomb interaction in the localized f-electron shells leads to a large renormalized effective masses of $100 - 1000$ electron masses [9]. These HFCs show NFL signatures when driven to a magnetic instability. For example, unusual power laws in resistivity have been seen in $CePd_2Si_2$, $CeCu_2Ge_2$, and $CeIn_3$ close to an antiferromagnetic (AFM) QCP when sufficiently high pressure is

applied [10]. These systems also exhibit superconductivity at very low temperatures close to magnetic QCP. New phases, such as superconductivity, avoiding a QCP with diverging critical fluctuations are common in HFC. While quantum critical fluctuations have been studied in antiferromagnetic systems [9], evidence for a ferromagnetic (FM) QCP remains scarce [11,12]. The existence of a FM QCP was even questioned since it is often avoided in clean materials by undergoing a first order transition. Since most HFCs show AFM order, weak FM d-metals with low transition temperature T_C were studied. For example, clean ferromagnets like MnSi [13] and $ZrZn_2$ [14] show first order transition as the QCP is approached by pressure. It is now understood that a "clean" FM QCP is unstable towards either a first order phase transition or other inhomogeneous magnetic phases [12]. But any amount of disorder can change the QPT and even lead to a stable FM QCP.

It is recognized that disorder plays a crucial role for QPT. Different theories classify the significance of disorder and predict the critical behavior [15]. Also a number of theories with distinct origins have been proposed to explain the observed NFL behavior in various systems [10]. Often the origin of NFL behavior is not straightforward since a combination of mechanisms could be responsible for the unusual properties, like a nearby magnetic phase, a local mechanism (such as multichannel Kondo effect) [16] or distribution of Kondo temperatures [17]. "Disorder" is unavoidable in real samples. Some defects are always present and often inhomogeneities are introduced through the convenient tuning parameter of chemical substitution to change the relevant interaction. It is, therefore, vital to systematically study systems which qualify for a disordered QPT to understand the origin of unconventional behavior [15].

A systematic study of d- and f-metals with controlled disorder is highly desirable

to test simple models and to explore further the suppression of FM in a metal. While FM d-metals are common (e.g. Ni, Fe, Co), FM f-metals in particular FM HFCs are rather rare. Recently, more examples were found, also chemical dilution series that show a QPT (e.g. $URu_{2-x}Re_xSi_2$ [18], $CePt_{1-x}Rh_x$ [19]) have been discovered.

FM alloys that are driven to a QPT by chemical substitution are good candidates to probe a scenario of disordered QCP. Chemical substitution does not only change the interaction among electrons, it also introduces inhomogeneities. But, it remains often unclear how much "disorder" is present in the system and how it affects the NFL behavior in the specific compound. In particular, the impact of the structural defects on the magnetic inhomogeneity of a ferromagnetic alloy in the vicinity of a FM QCP has not been tested systematically. Specific prediction for disordered QPT and better experimental methods to investigate local inhomogeneities are now available.

In this dissertation, I chose two series of alloys (the d-metal alloy $Ni_{1-x}V_x$ and the f-metal Ce-alloys, $CePd_{1-x}Rh_x$ and $CePt_{1-x}Rh_x$) with different magnetic properties and origin. They show signs of a disordered ferromagnetic quantum phase transitions. The main focus is to identify the local inhomogeneities and to reveal the impact of the local structure on the magnetic disorder to understand the origin of "disorder" and relevance for the QPT. Details about these systems and the methods are provided in section 1.5.

1.1 Magnetic properties of d- and f-metals

In general, magnetism in metals can arise typically from elements that contain incomplete shells of d- and f-electrons. Localized and itinerant electrons show a different magnetic response, with different moment sizes and coupling strengths [20]. Localized electrons are bound to the parent atom, a magnetic moment results due

to incomplete shells from orbital and spin contributions. But, the itinerant electrons are not bound to a single atom, and the magnetic moment comes primarily from the spin. In transition metals, the 3d electrons are often considered itinerant, and band models are effective to describe magnetism [20, 21]. The elemental ferromagnets like iron (Fe), cobalt (Co), and nickel (Ni) are examples of band magnets with fractional spins where the ferromagnetism is stable at temperatures much higher than room temperature.

The 4f-electrons, however, occupy an inner shell making them strongly localized and direct interaction are usually not effective. In rare-earth based metallic systems, the indirect exchange interactions between 4f-electrons are mediated by 5d and 6s conduction electrons. Unlike in transition metals, the magnetic ordering temperatures in rare-earth metals are usually lower than room temperature. This indicates that the magnetic interactions in rare-earth based metallic systems (f-metals) are much weaker than in transition based metallic systems (d-metals) [12, 20]. Since in 4f-electron systems the spin-orbit coupling is strong and the crystalline electric effects are weak, the magnetic ground state is often anisotropic. Therefore, a large magnetocrystalline anisotropy, due to the interplay between exchange and crystalline electric field interactions, is a unique property of rare-earth metals in the ordered state [20].

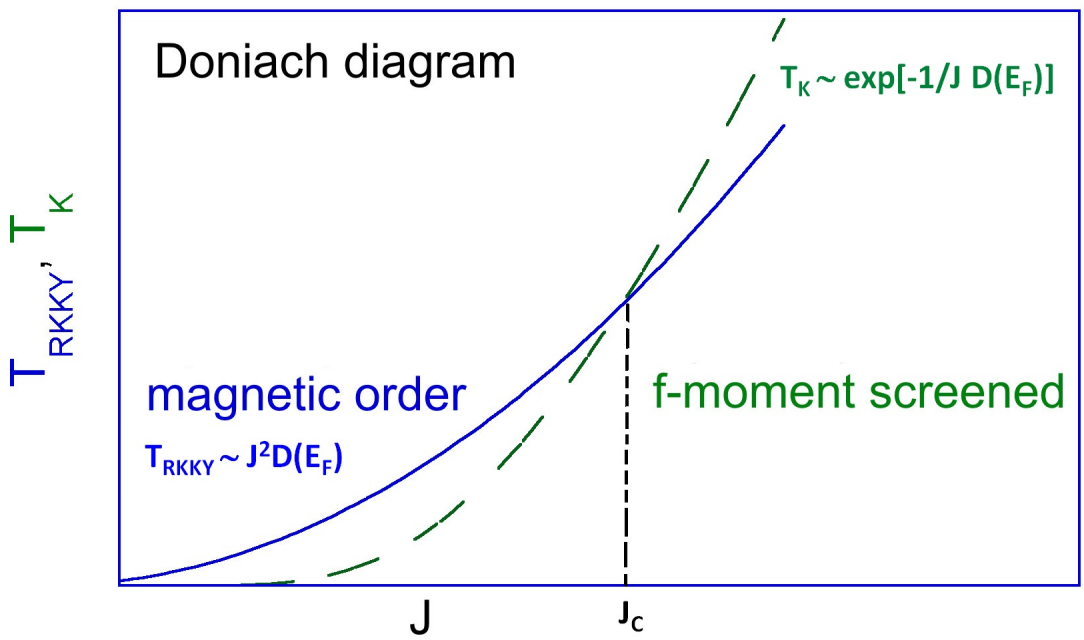

Figure 1.1: Doniach's generic phase diagram for the phase transition between an RKKY induced magnetically ordered phase and the Kondo screened, paramagnetic phase as a function of the local exchange-coupling parameter J.

Tuning magnetic interactions in a metal with localized magnetic moments can lead to a quantum phase transition. The Kondo effect plays an important role since it can also serve as an indirect coupling mechanism of magnetic moments in a metal. The Kondo effect is an unusual scattering mechanism of conduction electrons in a metal due to magnetic impurities [22, 23]. It is a process by which a free magnetic impurity ion becomes screened by the spins of the Fermi sea at low temperatures. As the impurity ion is screened, a portion of conduction electrons are bonded to it and hence the conductivity decreases [23, 24]. Towards low temperatures, an increase in resistivity due to the magnetic impurity is observed. As the dominant contribution to electrical

resistivity in normal metals comes from phonon scattering decreasing for $T \to 0$, the Kondo anomaly is noticed as a minimum in resistivity. In 1964, Kondo showed using a perturbation approach that a scattering process from magnetic impurities could give rise to a logarithmic contribution to the resistivity as a function of temperature [23]. However, Kondo's result is valid only for a temperature regime higher than a characteristic temperature called Kondo temperature ($T_K \sim e^{-1/|J|D(E_F)}$), where J is the coupling constant and D is the density of state at the Fermi level [23, 24].

When there are several localized magnetic moments in a metal, for instance arranged on a lattice (Kondo lattice), the same local spin-exchange coupling J that induces the Kondo effect, induces also a magnetic interaction between the localized spins. The local moments can exchange their spins, mediated by the conduction electrons [24, 25]. Since this effective, long-range spin-exchange coupling involves two elementary scattering events between electron and impurity spins, it is of order J^2 [23,24]. It can be ferromagnetic or antiferromagnetic due to the long-range, spatial oscillations of the conduction electron density correlations. This conduction-electron-mediated spin interaction was first considered by Ruderman and Kittel, Kasuya and Yosida and is therefore called RKKY interaction [25]. The RKKY interaction is usually the leading interaction in Ce-alloys since direct exchange coupling between neighboring local moments is weak due to the exponentially small overlap of the localized wave functions [24].

Fig. 1.1 displays Doniach's generic phase diagram for the phase transition between an RKKY induced magnetically ordered phase and the Kondo screened paramagnetic phase. The phase transition occurs when the RKKY interaction energy ($T_{RKKY} \sim J^2$) of a local moment to all surrounding moments exceeds the Kondo singlet binding

energy ($T_K \sim exp[\frac{-1}{J}]$). We see that the RKKY coupling always dominates for small values of the exchange coupling, J [22,24]. The exchange coupling can be tuned using external parameters such as pressure, chemical compositions, or magnetic field.

In a Kondo lattice, the local Kondo coupling and the RKKY interaction favor different ground states. The Kondo coupling leads to a paramagnetic Fermi liquid state without local moments [26,27]. In this state, the local orbitals, whose spectrum has a Kondo resonance at the Fermi energy, hybridize with each other and eventually become lattice coherent at low temperatures to form Bloch-like quasiparticle states [26]. As a result, a narrow band crossing the Fermi energy is formed. Its bandwidth is controlled by the Kondo resonance width T_K [26]. It thus gives rise to an exponentially strong effective mass enhancement (of roughly $m^*/m \sim \frac{1}{T_K} \sim exp[1/(2JD(E_F))]$), which explains the name heavy fermions. This Doniach model explains why a QPT can be observed in these materials, but does not predict more details of quantum critical properties [22].

1.2 Quantum phase transitions

A phase transition, in general, is an abrupt change in a system that occurs upon variation of a control parameter. The classical phase transitions (CPT) that occur at finite temperatures are driven by thermal fluctuations, tuned by e.g. pressure or temperature [7]. The melting of ice, the boiling of water, and the onset of ferromagnetic order in Ni (at $\sim$ 630K) are some examples of classical phase transitions. Quantum phase transitions (QPTs) are zero-temperature phase transitions which are accessed by variation of non-thermal control parameters such as pressure, magnetic field, or chemical compositions of materials. Although absolute zero is not experimentally accessible, characteristics of the transition should be noticed in the critical regime at

finite temperature [28].

Analogous to classical transitions, quantum phase transition can be of first order or second order. At first order phase transitions, the two phases coexist at the phase boundary. At continuous phase transitions, however, the two phases become indistinguishable at the critical point. Since a new quantity, the order parameter emerges continuously at the critical point, second order phase transitions are also called continuous phase transition.

A phase transition can be described by introducing an order parameter which is zero in the disordered and non-zero in the ordered phase. This was first introduced by Landau based on the assumption that for a given phase transition, the free energy (known as Landau free energy) can be written in powers of the order parameter m as [15, 29]

$$F = F_0 - hm + pm^2 + vm^3 + um^4 + ... \tag{1.1}$$

In a ferromagnetic phase transition, the order parameter m represents the spontaneous magnetization in zero field ($h = 0$). The coefficients, p, v, and u, are system parameters that may depend on external parameters such as pressure, temperature, or chemical composition. F_0 represents the value of the free energy at $m = 0$. The possible values of the order parameter can be determined by minimizing the free energy. If $v \neq 0$, Landau predicts first order transitions. For a continuous phase transition, v and all other odd terms must vanish due to symmetry reason [28, 30].

Here, it is important to note that the Landau theory uses the mean value of the order parameter only, neglecting the fluctuations of the order parameter about the mean. Therefore, this theory can fail in the vicinity of a critical point where fluctuations about the mean are very strong. Close to the critical point, e.g. for

non-zero temperature phase transitions, the fluctuations become very strong and the correlation length diverges as

$$\xi \sim t^{-\nu}, \tag{1.2}$$

where $t = |T - T_C|/T_C$ is the reduced temperature and ν is the critical exponent of the correlation length. In addition to the long-range correlations in space, there are long-range correlations of the order parameter fluctuations in time. The characteristic timescale for a decay of the fluctuations is the correlation time τ_c which diverges when we approach the critical point as [15, 30]

$$\tau_c \sim \xi^z \sim t^{-\nu z}, \tag{1.3}$$

where z is the dynamical critical exponent. Close to the critical point, ξ and τ_c are the only time and length scales, respectively, and their divergence is responsible for critical phenomena. At the critical point ($\xi_c \to \infty, \tau_c \to \infty$), fluctuations occur at all length and time scales thereby becoming time and space invariant. As a result, all observables follow power laws with related critical exponents; (for details see e.g. Ref. in [31], pp 44-45). The values of the critical exponents generally do not depend on the microscopic details but only on the space dimensionality and the symmetries of the system under consideration. For instance, all 3D Heisenberg magnets (FM or AFM) with short range interaction have the same exponents. They belong to the same universality class [28].

The generic phase diagram in Fig. 1.2 shows the critical regime of a classical phase transition with $T_C > 0$ and a quantum phase transition with a quantum critical point at r_c. The external tuning parameter is r; an example is pressure, magnetic field, or concentration of materials.

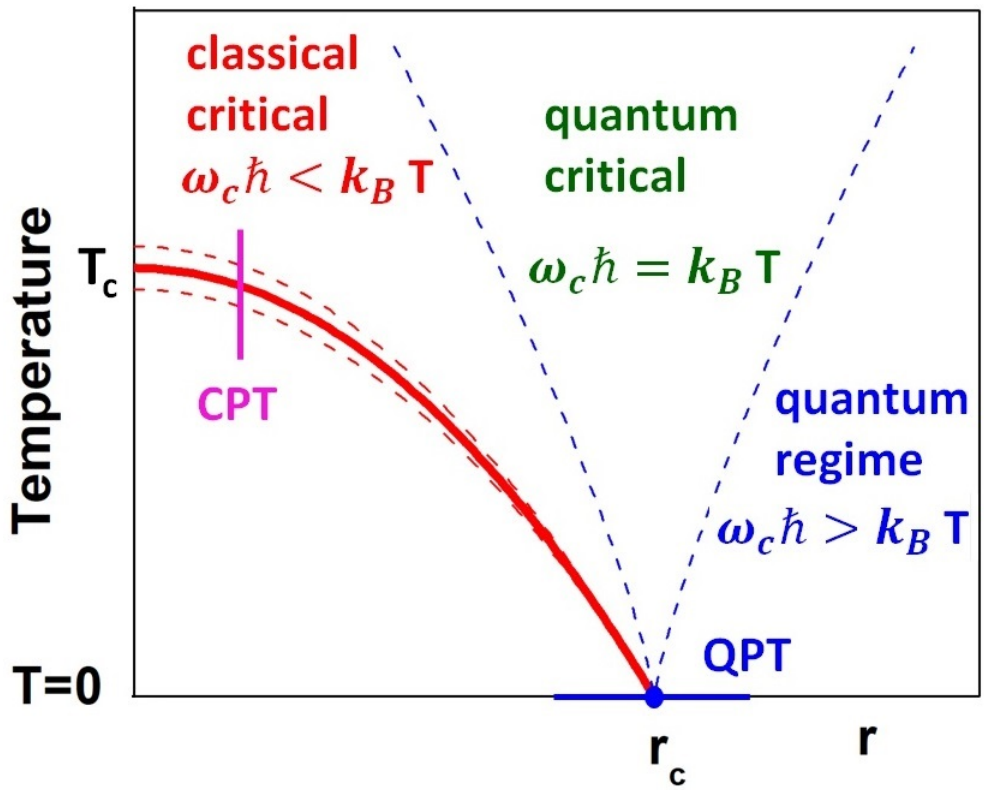

Figure 1.2: Generic phase diagram of a QPT in the vicinity of a quantum critical point (QCP) located at r_c, where r is a tuning parameter changing interaction. The solid line marks the finite- temperature boundary between the ordered and disordered phases and the dashed lines indicate the boundaries of the quantum critical region.

Thermal fluctuations (with energy scale $\sim k_BT$) dominate the thermally disordered regime whereas quantum fluctuations (with energy scale $\sim \hbar\omega$) dominate the quantum disordered region. Both fluctuations become important in the quantum critical region with $\hbar\omega_c \sim k_BT$. Since the quantum critical fluctuations grow with distance from r_c, $\hbar\omega_c \sim |r-r_c|^{\nu z}$, the crossover lines between the quantum critical region and the disordered regions are determined by $k_BT \simeq \hbar\omega_c \sim |r-r_c|^{\nu z}$ [30]. The system dimension and the number of components of the order parameter determine the

strength of fluctuations. Usually, as the system dimension and the number of the order parameter components increase, the significance of fluctuations decreases [28,30]. For classical phase transitions, in sufficiently low dimensions ($d \leq d_c^-$), fluctuations are so strong that they completely destroy the ordered phase at all (nonzero) temperatures, where d_c^- is the lower critical dimension. Below an upper critical dimension (d_c^+), an ordered phase and thus transition exists with specific critical exponents that are influenced by fluctuations and depend on the dimensionality, d [28]. For $d \geq d_c^+$, fluctuations are not important for the critical behavior. The exponents become independent of d and take their mean-field values [28]. For example, for Ising ferromagnets, the critical dimensions are $d_c^- = 1$ and $d_c^+ = 4$, whereas for Heisenberg ferromagnets, $d_c^- = 2$ and $d_c^+ = 4$. For more details see e.g. [28] and the references therein.

The dimensionality cases we considered above are for phase transitions that occur at nonzero temperatures (classical phase transitions). For quantum phase transitions, it was shown by Hertz that both temporal and spacial fluctuations are important to determine quantum critical behavior. QPT can be described as phase transition with an effective higher dimension $d_{eff} = d + z$, where z is the dynamical exponent and d is the spatial dimension [28, 30]. Because of the higher "dimension", mean field models are expected to be more successful for QPT. However, since the dynamics is a relevant critical quantity, QPTs are more diverse and complex. FM QPTs differ from AFM QPTs [32].

1.3 Impact of disorder on quantum phase transition

Real materials always contain some disorder (randomness) in the form of vacancies, impurities, and other defects. The terms "quenched" and "annealed" disorder

indicate if the disorder is static or dynamic [28]. We focus on quenched disorder with time independent defects.

A basis for the discussion of the effect of disorder on classical continuous transitions is given by the Harris criterion [33], which states that if the correlation length exponent ν of a given phase transition obeys the inequality [28, 30]

$$\nu \geq 2/d, \tag{1.4}$$

with the space dimensionality d of the system, then the critical behavior is unaffected by quenched disorder. If a clean critical point violates this inequality, the disorder modifies the critical point leading to three possibilities [30]:

(A) The system goes to a new critical point by changing the value of ν to meet the criteria.

(B) The system will have an unconventional critical point. It leads to non-power law scaling behavior of the critical exponents.

(C) The disorder can destroy the phase transition completely. The system has independent regions that undergo phase change at different critical temperatures resulting in a smeared transition.

CPTs have been studied successfully, still new universality classes are discovered. Often the range of the critical regime is not clear. Far less is known for the QPT. The specific prediction of clean homogeneous QPT in strongly correlated electron systems is already a challenge, to include the impact of disorder in QPT is even more demanding. Disorder seems to have a stronger impact on QPT than CPT and seems unavoidable using experimental tuning parameters to tune quantum fluctuations. In recent years, significant progress has been made on prediction of disordered QPT [28].

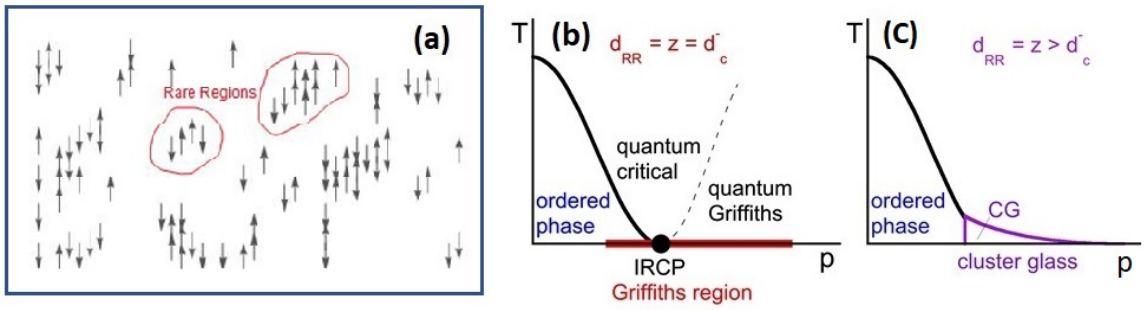

Figure 1.3: (a) Sketch of diluted magnet with rare region devoid of impurity. Different schematic QPT scenario for quenched disorder showing (b) infinite randomness critical point with a quantum Griffiths regime expected for Heisenberg symmetry and (c) a cluster glass phase expected for Ising symmetry.

In a magnetic QPT, disorder can be introduced by diluting a magnetic system with a nonmagnetic impurity. The dilution reduces the magnetic long-range order and thus reduces T_c from its clean bulk value T_0. Arbitrarily large spacial regions (magnetic clusters) that are devoid of impurities will be formed. For temperatures $T_C \leqslant T \leqslant T_0$, these regions will locally order even though the bulk is globally in the paramagnetic phase [15]. Griffiths was the first to show that these rare regions can lead to a singularity in the free energy, the Griffiths singularity, in the entire temperature region $T_C < T < T_0$. This region in now known as the Griffiths region or the Griffiths phase [34, 35], where T_C is the critical temperature for the clean system and T_0 is that of the impure system. While classical Griffiths phase singularities are weak, quantum Griffiths phase singularities are expected to be much stronger. Signatures of a quantum Griffiths phase are anomalous nonuniversal power-law dependencies of the magnetization, susceptibility, and other thermodynamic quantities

on temperature and magnetic field. Analogous singularities are also expected on the ordered side of the phase transition [2, 34]. In recent years, rare regions have been studied in many other disordered classical, quantum, and non-equilibrium systems. The qualitative features of the resulting Griffiths phenomena can be classified according to the effective dimensionality of the rare regions [28, 36]. Depending on the effective dimensionality (d_{RR}) of the rare regions, the following classes can be distinguished [28]:

(A) If the rare regions are below the lower critical dimension of the system ($d_{RR} < d^-$), exponentially weak Griffiths singularities and critical points with conventional scaling are expected.

(B) If the rare regions are right at the lower critical dimension ($d_{RR} = d^-$), but still cannot order independently, the Griffiths singularities are of power-law type and the critical point is an exotic infinite-randomness critical point.

(C) If the rare regions are above the lower critical dimension ($d_{RR} > d^-$), they can undergo the phase transition independently of the bulk system. The global transition is thus smeared.

A quantum Griffiths phase is expected for itinerant Heisenberg magnets (class B) as shown in Fig. 1.3(b), while a cluster glass phase is expected for itinerant Ising magnets (class C) in Fig. 1.3(c). If "z" is temperature dependent both "phases" are predicted at different temperatures [15]. For more detailed explanation, see reviews [28, 30] and references therein.

1.4 Fermi liquid and non-Fermi liquid behavior

At the beginning of the 20th century, P. Drude formulated the free electron model to describe the properties of metals whereby the valance electrons of the atoms in the metal are regarded as a gas of non-interacting conduction electrons [37]. This model essentially ignored the electron-electron Coulomb interaction and the electron-lattice interaction. The Sommerfeld theory, the Drude's model with the proper Fermi statistics, was very successful in describing the properties of alkali metals at low temperatures. For example, it accounts well for the low temperature specific heat and the magnetic Pauli susceptibility of those metals. But, the Sommerfeld model failed to describe transition metals like Fe and Mn, where the valence electrons are more localized [38].

Landau postulated in his Fermi liquid theory that there would be a one-to-one correspondence of the low energy eigenstates of the interacting electrons with those of the non-interacting Fermi gas by switching on the interaction adiabatically [38,39]. The interacting electron, "dressed" by its interaction with a screening cloud of other electrons, can be considered as non-interacting "quasiparticle" with an effective mass $m^* > m_e$, where m_e is free electron mass [39].

The Landau Fermi liquid theory predicts that the temperature dependence of the specific heat (C), the Pauli susceptibility (χ_P), and electric resistivity (ρ) at low temperatures have the same form as their free electron model counter part except that the interacting electrons become heavier "quasiparticles" with an effective mass m^*. This is because these properties only require the presence of a well defined Fermi surface, and are not sensitive to what forms it (electrons or quasiparticles) [39]. These

quantities at low temperatures ($T < T_F$) in the Fermi liquid scenario are given as

$$C = \gamma_0 T, \quad \gamma_0 \sim m^*, \tag{1.4}$$

$$\chi = \chi_0, \quad \chi_0 \sim m^*, \tag{1.5}$$

$$\rho(T) = \rho_0 + AT^2, \sqrt{A} \sim m^*. \tag{1.6}$$

In recent years, experiments performed on a new class of materials called heavy fermions (HF) appeared to confirm the Fermi liquid theory. Heavy fermions are metallic compounds that usually contain a rare earth or actinide atom (U, Ce, Yb) with a partially filled $4f$- or $5f$- electron [40]. Among the first materials discovered were UPt_3, $CeCu_6$, and UCd_{11} [40]. At low temperatures, the f-electrons strongly couple to the conduction band which results in enhancements of the effective mass m^* to values 100-1000 times larger than the electron mass. This mass enhancement is observed in high values of $\gamma_0(m^*)$, $\chi_0(m^*)$, and $A(m^{*2})$ at low temperatures.

Most heavy-fermion materials are in good agreement with the Fermi-liquid expectations. However, many HFs, transition metals, and intermetallic compounds have emerged whose physical properties at low temperatures show remarkable deviations from Fermi liquid theory [10]. Landau's quasiparticle picture is often valid in the limit of small energy transfer during scattering which is enforced by the Pauli principle that confines all scattering particles to the vicinity of the Fermi surface. But if electron interactions become long ranged due to slow propagation or diffusion, leading to a singular energy dependence in the scattering matrix, the decay rate reaches the energy of the excitation losing the particle properties. In this case, quasipariticles and the Fermi surface are not defined and the Fermi liquid concept breaks down [39]. Interacting electron systems violating Fermi liquid requirements are called

non-Fermi-liquids (NFL). Typical thermodynamic properties indicate the "lack" of the renormalized energy scale through weak power laws or logarithmic divergences at low temperatures [10, 39], e.g.,

$$C/T \sim -lnT \quad or \quad C/T \sim T^{-\alpha}, \tag{1.7}$$

$$\rho - \rho_0 \sim T^n, \quad with \quad n < 2. \tag{1.8}$$

Different models have been developed to explain the origin of NFL behavior. The bases for these models, however, stem from one or the combination of concepts such as single ion effect, disorder, and proximity to magnetic instability [10]. NFL behavior is observed to occur at a second-order phase transition where the transition temperature is suppressed to zero close to a quantum critical point.

1.5 Specifics of target systems

1.5.1 $Ni_{1-x}V_x$

The first part of the thesis focuses on the binary d-electron alloy $Ni_{1-x}V_x$. Nickel is itinerant FM with high transition temperature $T_C \simeq 630K$. Replacing nickel (Ni) with nonmagnetic vanadium (V) suppresses the FM transition temperature down to zero at a critical concentration $x_c \sim 0.116$ [1, 2]. This dilution of a magnetic system with a nonmagnetic impurity e.g. Ni by V also introduces magnetic disorder. V suppresses effectively the magnetic moment of the neighboring Ni atoms [41]. A random location of V creates randomly distributed Ni-rich regions responsible for the inhomogeneous magnetism. Even specific predictions for a disordered QCP [34] could be confirmed in this system. For example, power laws in the magnetization and susceptibility have been reported (see Fig. 1.4) with the exponents that are varying with the distance from the critical point [1]. These are signatures of a quantum

Griffiths phase.

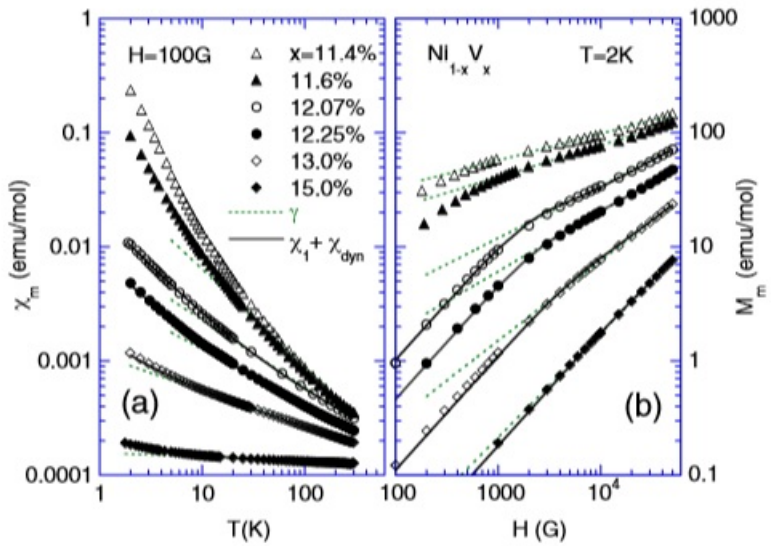

Figure 1.4: (a) Low-field susceptibility of $Ni_{1-x}V_x$ versus temperature T and (b) low temperature magnetization versus magnetic field H. Dotted lines indicate power laws for $T > 10$K and $H > 3000$G in (a) and (b), respectively. Solid lines (shown for $x > 0.12$) represent fits to a model that includes fluctuating and frozen clusters. From Ref. [1].

Ni-V is the system that shows the most convincing evidence of such a quantum Griffiths phase. Also the phase boundary between FM and PM phase, $T_C(x)$, shows the predicted behavior as it presents a "tail" shape [1] approaching the QCP (see Fig. 1.5). Ni-V looks like an ideal model system displaying the properties of a disordered magnetic QCP with Heisenberg symmetry [28]. Towards very low temperatures, the phase diagram becomes more complex. A cluster glass (CG) phase prevents further approach towards the QCP [2]. The origin of this CG phase is still an open question signaling interacting clusters with different distribution or coupling

as ideally assumed.

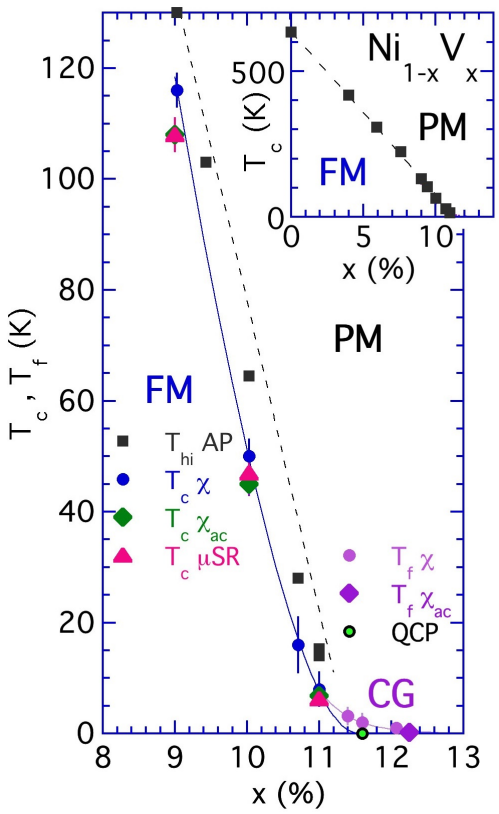

Figure 1.5: Phase diagram of $Ni_{1-x}V_x$ showing paramagnetic (PM), ferromagnetic (FM), and cluster glass (CG) phases. The ferromagnetic transition temperature, T_C, is determined from different methods indicated.

It has been reported that the long-range but weak RKKY interaction can change the condition towards low temperature so that the cluster dimension exceeds the lower critical dimension and a cluster glass is expected [15]. RKKY interaction is feasible in the Ni-V alloy, but chemical clusters or other crystalline defects in the samples can modify the magnetic cluster distribution and contribute to CG freezing. To rule out chemical clusters as the primary cause, a thorough structural analysis is important

to identify the location of V and the quality of the structure. Previous experiments have been performed on Ni-V pellets that revealed good structural quality [42]. These pellets could not fill the sample holder uniformly increasing uncertainties in the analysis. To confirm the major results on ideal uniform samples, Ni-V powder samples are selected for further structural investigation.

In this thesis, I aim to further investigate the Griffiths phase (beyond just power laws observed in bulk measurements) by revealing the microscopic details of magnetic clusters using neutron scattering and muon spin rotation (μSR) measurements. In addition, I want to clarify the origin of the magnetic clusters and determine how the chemical structure is responsible for the magnetic disorder. Chapter 2 introduces the experimental methods. Chapter 3 presents the structural analysis of a selected Ni-V powder sample. This structural powder data promises better resolution to resolve the essential chemical and structural parameters of our samples. The structure and chemical disorder in Ni-V are probed by a wide angle neutron diffraction experiment at a Spallation Neutron Source (SNS) with a detailed pair distribution function analysis.

A μSR study and first magnetic neutron scattering data are presented in Chapter 4. Due to muon's large magnetic moment, polarization in zero field, and their implantation on interstitial sites, μSR is sensitive enough to probe the very small internal magnetic fields and the local distribution in our sample. It can also distinguish static moments from fluctuating ones and therefore is able to identify magnetic clusters across the transition regime. First μSR data in Ni-V show that the FM and PM response can be described by simple models. A detailed analysis close to x_c should reveal fluctuating magnetic clusters in Ni-V. Magnetic small angle neutron

scattering (SANS) data gives direct information about the magnetic cluster size distribution. Early SANS measurements showed that the magnetic moments are too small to see clusters in the paramagnetic regime. However, by focusing on samples close to the critical concentration, an appropriate scattering vector regime, and with a better statistics, a SANS measurement should become effective to reveal the missing important length scales in the vicinity of a disordered quantum phase transition.

1.5.2 $CePd_{1-x}Rh_x$ and $CePt_{1-x}Rh_x$

$CePd_{1-x}Rh_x$ and $CePt_{1-x}Rh_x$ are among the few FM Ce-alloys driven to a nonmagnetic state by doping Ce-ligands. Both systems evolve from a FM ordered state with $T_C \sim 6.6K$ to a nonmagnetic mixed-valent state as the concentration of Rh increases from $x = 0$ to $x = 1$ [11, 19]. The competition between the indirect RKKY interaction and the Kondo screening effect leads to a quantum phase transition [11,43].

The magnetic phase diagram of $CePd_{1-x}Rh_x$ and $CePt_{1-x}Rh_x$ are similar. The transition temperature T_C changes when sufficient Pd [11] or Pt [19] is replaced by Rh, respectively. It is shown that the suppression of a FM phase in the Pd-system varies more rapidly towards $x^* \simeq 0.67$ and finally vanishes towards $x_{cr} \simeq 0.85$ [11]. The details of the magnetic order at higher $x > x^*$ and the nature of the critical point at x_{cr} are not clear. The tail shape of $T_C(x)$ indicates that the system exhibits magnetic inhomogeneity towards higher concentration of Rh. Close to x_{cr}, signs of NFL behavior have been noticed for the Pd-system in heat capacity [44, 45], magnetic susceptibility [46], and neutron scattering measurements [5]. Magnetization and specific heat data for higher Rh concentrations present power laws with different exponents in the magnetic susceptibility as typical signature of a quantum Griffiths phase, see for example in [43].

Less data are available for the Pt-system. Resistivity measurements under pressure reveal a QPT of the pure CePt without chemical substitution [47]. For the Pt-system, the available data of $T_C(x)$ are similar to the Pd-system [48]. Heat capacity and magnetic susceptibility measurements indicate that the well defined FM transition in CePt becomes less sharp with Rh substitution at $x > 0.6$ [48]. χ_{ac} data support that the long-range FM order is compromised by a cluster glass already at $x \simeq 0.5$ [19]. For example, the low temperature ac-susceptibility of the Pt-samples at $x = 0.5$ and $x = 0.6$ measured at various frequencies shows a pronounced maximum at T_f which shifts noticeably towards higher temperatures as the driving frequency increases [19].

A cluster glass phase and a quantum Griffiths phase are both signs of a disordered QPT. Why the Pt-system enters a cluster glass already at $x \simeq 0.5$ and the Pd-system only shows weak glassy properties for $x > 0.7$ with power laws and scaling properties for $x \lesssim x_{cr}$ is not clear. Different structural properties of particular samples especially the local symmetry of the Ce-environment can be responsible for such different behavior. Magnetization data on single crystals show that the magnetic Ce-environment of the Pd-system becomes effectively more isotropic for higher x [49], while the anisotropy for the Pt-system has not been reported.

To figure out the main cause of these differences and the impact of structural disorder on the magnetic inhomogeneity in both f-electron compounds, I chose to study both systems at several Rh concentrations starting with a detailed structural investigation. Collecting data at a wide angle neutron powder diffractometer allows an investigation of the local Ce-environment using the pair distribution function (PDF) analysis. I aim to reveal the origin of magnetic disorder and the difference between the two systems.

Chapter 2

Experimental methods

This chapter presents the experimental techniques and the instruments used in my dissertation. Several experiments have been conducted in our laboratory at KSU, at other laboratories in our Department, and at different National laboratories. Our laboratory offers sample growth facilities and low temperature measurement systems for magnetic susceptibility and resistivity.

The sample growth facility includes a clean sample preparation environment and various important apparatus. A copper-beryllium cutter is used to cut our metals into pieces of a desired mass. It is non-magnetic and hence does not compromise the magnetic properties of our samples. A precision up to $10^{-5}g$ is achieved using a Fisher microbalance to weigh our samples and pieces of metals. A glove box offers an almost oxygen free environment to cut and weigh cerium (Ce) metal since it oxidizes easily in an open air environment.

Our samples are grown using a Mini Arc Melting System in an argon environment and are annealed in vacuum to ensure uniform distribution of atoms. I grew several polycrystalline samples of $Ni_{1-x}V_x$, $CePd_{1-x}Rh_x$, and $CePt_{1-x}Rh_x$ at different vanadium (V) and rhodium (Rh) concentrations. The details of our sample preparation process and the instruments used are discussed later.

2.1 Sample growth

Several polycrystalline samples have been grown from pure elements. $CeT_{1-x}Rh_x$ samples with T=Pd or Pt were made from Ce rod with purity (99.9%), palladium (Pd) foil (99.99%), platinum (Pt) foil (99.997%), and rhodium (Rh) slugs (99.95%). The Ni-V samples were prepared from nickel (Ni) slugs with 99.995% purity and vanadium (V) with 99.8% purity, all purchased from Alfa Aesar. Ce-alloy sample preparation is presented here since the Ni-V sample preparation process is similar and explained elsewhere (see for example in [50]). We started by cutting a Rh slug into several pieces using a rotating diamond saw with the weight of each piece estimated to be enough to make a $\sim$ 250mg sample. According to the desired concentration, each Rh piece is weighed using a very high precision scale. By taking the average of 3 measurements, the corresponding mass of Pd or Pt is calculated using the relation

$$m_P = m_{Rh}\left[\frac{M_P}{M_{Rh}}\right]\left[\frac{x}{1-x}\right], \tag{2.1}$$

where x is the Rh concentration, m_{Rh} is the measured mass of a Rh piece in grams, and m_p is the corresponding required mass of Pt or Pd in grams. M_{Rh}=102.9055 g/mol, M_{Ce}=140.12 g/mol, M_{Pd}=106.42 g/mol, and M_{Pt}=195.08 g/mol are the atomic weight of Rh, Ce, Pd, and Pt, respectively. After calculating and measuring the desired mass of Pd or Pt, the next step is to calculate and measure the mass of Ce needed. We first calculate the number of moles of Ce ($n_{Ce} = n_{Rh} + n_P$) needed by adding the number of moles of Rh and Pd/Pt. The product of the atomic weight of Ce with the calculated number of moles ($m_{Ce} = n_{Ce}M_{Ce}$) gives the desired mass of Ce. Because Ce oxidizes very easily, one has to cut and weight pieces of Ce rod in an almost oxygen free environment. We used a glove box system which consists of a vacuum pump, argon gas attachments, an oxygen trap, and a moisture trap. The

oxygen level is monitored by an oxygen sensor placed in the glove box. All Ce-metal pieces used for our samples were cut and weighed using a scale inside the glove box at oxygen level below 150ppm. After cutting and weighing each piece of metals within 0.1% accuracy, they are transferred to an arc melting system where the metal pieces are placed in a water-cooled copper plate and sealed in the melting chamber. The growth of our samples is done by using a compact Arc Melting System (MAM-1) from Edmund Buehler. This equipment is designed for melting metals by creating a high voltage electric arc with temperature up to 3500^0C. An electric arc is a breakdown of a low pressure gas (e.g. argon gas in between two electrodes) that produces a continuous electrical discharge when a high voltage is applied between the two electrodes made of tungsten. The ionized gas is then ignited when the movable conical tip electrode at the top (serving as a cathode) nearly touches the second electrode fixed in the copper plate at the bottom (anode). The luminous electrical discharge produced between the two electrodes is hot enough to melt metallic materials placed in a water-cooled copper plate.

The melting process begins by cleaning the tungsten electrode tips and the copper plate using sand paper and acetone. The water-cooling system must be turned on at the beginning of the process to cool down the copper plate where the samples and the tungsten anode are situated. A batch of two alloys can be made in a single evacuation as there are three notches on the copper plate. One is used for melting a tantalum slug to make sure that any leftover oxygen is absorbed. Once the metals are put in place and sealed to the melting chamber, the purging process begins. The existing oxygen is evacuated using Leybold Trivac B oil-sealed rotary vane pump below 1mbar and then back filled with argon gas so that the final atmosphere inside the chamber is argon at

ambient pressure. This process should be repeated at least four times, and the screws holding the copper plate need to be checked and tightened after each cycle of purging. The argon gas used is 99.999% pure and gets further purified by a moisture and an oxygen traps installed for this purpose. It is chosen for its purity and low thermal conductivity. The melting process is initiated igniting the arc by pressing the top conical tip (cathode) down so that it nearly touches the anode (tungsten embedded in the copper plate) at the bottom. The intensity of the arc is proportional to the strength of the current which can be controlled by a potentiometer. The compact arc melting system in our laboratory gives a range of current varying from 5A to 200A. Our samples usually melt at a low current $\sim$ 50A. Higher current could result in mass loss due to overheating. Once the arc is ignited, the tantalum slug is melted for the aforementioned purpose and then the two samples are melted. Each sample is turned over and melted three times to improve the compositional homogeneity. The samples are then taken out and weighed again to check for a possible mass loss during the melting process. In general, a mass loss of less than 0.05% is acceptable.

After the samples are grown, they are annealed to improve the homogeneous atom distribution. The samples are wrapped in a piece of tantalum foil (99.998% purity) and labeled to identify them later during unwrapping. Quartz tubes of 10mm inner diameter with one end open are used to seal one or more samples in vacuum. We first clean the tubes using acetone and purge them with pure helium compressed gas to replace some of the existing oxygen inside. The pumping system, consisting of a roughing vacuum pump and a turbo pump, is checked regularly for possible leaks at different junctions using a helium leak detector. The O-rings are checked and replaced if necessary. The tube is then pumped until the vacuum pressure at

the pump reads $\sim 10^{-5}$mbar. The high temperature flame produced by mixing a compressed hydrogen and oxygen gas is hot enough to melt and seal the quartz tube. Two heat sinks made of aluminum metal are clamped onto the tube to protect the samples from the heat generated during the sealing process. The sealed quartz tube can then be transferred to the tube furnace (Lindberg/Blue Mini-Mite). Two samples can be annealed at the same time. Our Ce-alloy samples are annealed at 900°C for seven days. The quartz tubes are then taken out for further cool down after the temperature in the furnace is lowered to 350°C. The samples are weighed and compared with their weight before annealing to check for any mass loss due to vaporization. Selected samples were crushed to powder by using a mortar and pestle for X-ray and neutron powder diffraction experiments.

2.2 X-ray powder diffraction

X-rays were discovered by Wilhelm Roentgen in 1885, and Max von Laue (1912) was the first to realize that they might have the right wavelengths to diffract from crystal lattices [51]. This is possible because their wavelength is in the same order of magnitude (1-100$\mathring{A}$) as the interplanar spacings (d) in crystals. When X-rays of the right wavelength are scattered by a periodic array of atoms in a crystal with a long-range order, they produce constructive interference peaks at specific angles. Each peak in a diffraction pattern represents scattering from a specific set of parallel plane of atoms identified by Miller indices (hkl) and their occurrence is governed by Bragg's law [51, 52]

$$n\lambda = 2d_{hkl} sin\theta_{hkl}, \tag{2.2}$$

where n is a positive integer representing the order of diffraction, λ is the X-ray wavelength used, d_{hkl} is separation of atomic planes identified by the Miller indices (hkl), and θ_{hkl} the scattering angle specific to these planes. The interplanar spacings are directly related to the lattice constants of a crystal lattice. For orthorhombic crystals with lattice constants $a \neq b \neq c$, the interplanar spacings (d_{hkl}) are given as

$$d_{hkl} = \frac{1}{\sqrt{(\frac{h}{a})^2 + (\frac{k}{b})^2 + (\frac{l}{c})^2}}. \tag{2.3}$$

Because X-rays are electromagnetic waves, they interact with electrons in each atom. The diffraction pattern, therefore, contains important information about the atomic arrangement in the crystal. For example, the positions of the diffraction peaks indicate interatomic distances, and the diffraction peak intensities contain information about the atom types and their positions. The widths and shapes of the peaks are related to short range order structures and some instrumental parameters.

Using a simple X-ray tube with a specific metal target, e.g. copper (Cu) and an area detector to locate the diffracted beam, two different methods are effective. The diffraction pattern of polycrystalline samples are concentric rings using the strong monochromatic source (Debye-Scherrer method). Lattice parameters can be determined. The diffraction pattern of single crystals requires the whole weaker continuous spectrum (Laue method). It serves to align crystals. To check the structure of our samples, we performed a powder X-ray diffraction experiment using an X-ray tube with a Cu-Kα source ($\lambda = 1.5418\mathring{A}$) and a 2D camera. Our samples are polycrystalline Ce-alloys with different Rh concentrations crushed to powder using a mortar and pestle. Our setup includes an X-ray tube with a monochromator and a collimator system, a sample holder, an area detector, and a signal processing interface to convert

our data to a computer readable form for further data analysis. The powder samples were spread in a thin layer on a transparent tape and mounted onto the sample holder. All our data were collected at an operating voltage of 40kV and current of 40A with an exposure time of 20 minutes.

The original two dimensional 2D data (Debye-Scherrer rings) were converted to 1D data as displayed in Fig. 2.1. The data conversion is performed by integrating the intensity over the angle at constant radius using FIT2D, a 2D data reduction and analysis program specializing in model fitting, detector calibration, and distortion correction [53].

Fig. 2.1(a) shows the Bragg peaks for CePt sample at zero Rh concentration ($x = 0$). The (111) peak from silicon (black) is included for calibration. The peak heights are very small to compared to the background signal, e.g. the strongest peak at $\sim 40^0$ is about 5% of the total count. The Bragg peaks for the Pt-samples at the lowest and the highest Rh concentrations at $x = 0$ and $x = 0.8$ are shown in Figs. 2.1(a) and (c), respectively. We see that the two prominent peaks get broader as the concentration of Rh increases. The Bragg peaks for the Pd-sample at $x = 0.8$ is shown in Fig. 2.1(d) which resembles the result from the Pt-sample at the same concentration ($x = 0.8$). These few peaks indicate crystalline samples, but do not allow a structure analysis. We therefore employed a higher resolution wide angle scattering technique presented next.

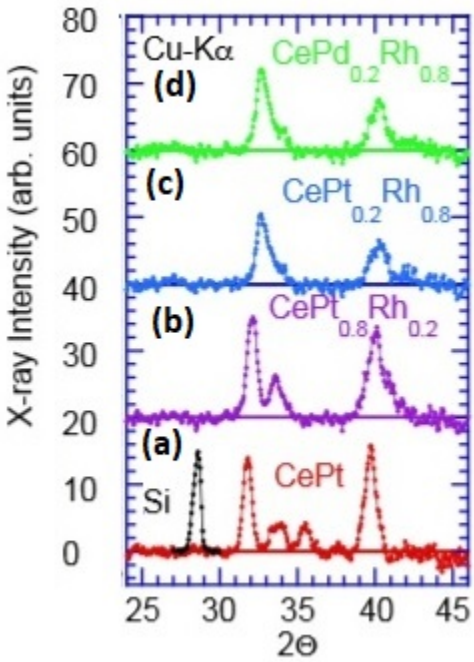

Figure 2.1: Reduced X-ray powder diffraction data for (a) CePt, (b) $CePt_{0.8}Rh_{0.2}$, (c) $CePt_{0.2}Rh_{0.8}$, and (d) $CePd_{0.2}Rh_{0.8}$. The black peak in (a) is the (111) peak from silicon powder sample for calibration. Data collected using Cu-Kα source with $\lambda = 1.5418\mathring{A}$.

2.3 Neutron scattering

Neutron scattering is also an interference based technique that reveals the chemical and magnetic structure of materials and their dynamics on a nanometer scale. Although neutrons are particles, they behave like a wave (wave-particle duality) and hence experience interference effects. With zero electric charge, neutrons barely interact with matter and can easily penetrate deep into a sample and directly interact with the nuclei of atoms. This makes them a suitable bulk probe unlike X-rays which are scattered by electrons not penetrating far beyond the surface [54]. Although

the neutron carries no net charge, it has a magnetic moment. The neutrons magnetic moment interacts with the unpaired electron spins of magnetic atoms through a dipole-dipole interaction. The neutron is, therefore, a powerful probe of magnetic properties of materials [52]. In a neutron scattering process, a beam of neutrons with initial wave vector $\vec{k}_i$ is scattered by a nucleus and emerges with a wave vector $\vec{k}_f$ at an angle 2θ relative to the initial direction of incidence. For an elastic collision, the magnitude of the wave vectors before and after collision is equal. The Bragg condition in reciprocal lattice is therefore [51]

$$Q_{hkl} = |\vec{k}_f - \vec{k}_i| = 2|\vec{k}_i| sin\theta_{hkl}, \tag{2.4a}$$

with $|\vec{k}_i| = 2\pi/\lambda$, where λ is the wavelength of the incident neutron beam. The scattering vector Q, determined by the difference of k_f and k_i, has to match a reciprocal lattice vector or the inverse interplanar spacing, d_{hkl}, between the planes ($Q_{hkl} = 2\pi/d_{hkl}$) to show a Bragg peak.

A small angle neutron scattering (SANS) experiment collects data at small angles i.e. $\theta = 0.01^o - 10^o$ to get the scattered intensity at small scattering vectors with high resolution.

$$Q = |\vec{k}_f - \vec{k}_i| = 2|\vec{k}_i|\theta. \tag{2.4b}$$

SANS can therefore probe and resolve structures (magnetic or nuclear) of large length scale ($d \sim \frac{1}{Q} \simeq \lambda/2\theta$). Typically, structure features in materials ranging from roughly 1nm to over 500nm can be probed.

The intensity of the scattered neutrons is measured as a function of the scattering vector (Q) in a neutron scattering experiment. The scattered intensity depends on the interaction between the neutron and the nucleus which is known to be very short range

$\sim 10^{-13} cm$. Therefore, the scattering can be taken as point like or isotropic and can be characterized by a single parameter called the scattering length b [52]. The scattering cross section for a single nucleus is thus $\sigma = 4\pi b^2$ which is independent of the atomic number unlike X-rays and electrons diffraction [54]. Typically, $b \sim 10^{-13}$cm but varies strongly across the different atoms. Incoherent contribution and absorption have to be considered in planning a neutron scattering experiment. Different neutron scattering instruments have been designed depending on the neutron source. The neutrons used in a scattering experiment can be obtained from a nuclear reactor, where the neutrons arise from the spontaneous fission of U^{235} in which neutrons are produced continuously. Neutrons can be also produced when high energy protons bombard a heavy target (e.g, U, W, Ta, Pb, or Hg) in a spallation source. This typically results in pulsed neutron beams [52, 54].

We performed neutron scattering experiments at different facilities. We used SANS instruments, NG7 SANS at NCNR, NIST and GPSANS at HFIR, ORNL. Both SANS are located at a reactor with a cold moderator.

We also performed a wide angle powder neutron diffraction experiment at the Spallation Neutron Source (SNS), Oak Ridge National Lab (ORNL) on the Nanoscale Ordered Materials Diffractometer (NOMAD). The SNS offers a wide range of neutron energies essential for a wide angle diffraction instrument. The NOMAD is a neutron time-of-flight (TOF) diffractometer designed to perform structural determinations of local order in crystalline and amorphous materials with pair distribution function analysis [4]. A large neutron flux is provided by the spallation neutron source and a broad range of scattering angle detection is achieved by 6 banks each having specific angular coverage. Although laboratory X-ray sources might give important PDF data,

in many cases high energy epithermal neutrons are required to access high values of Q_{max} [55]. A maximum momentum transfer of $Q_{max} = 50\mathring{A}^{-1}$ can be obtained but typically $Q_{max} = 30\mathring{A}^{-1}$ is sufficient corresponding to a real space resolution of $\Delta r = 0.1\mathring{A}$. However, due to the resonance absorption of Rh at $\lambda \approx 0.25\mathring{A}$, a smaller cut off at $Q_{max} = 24\mathring{A}^{-1}$ is used to produce the PDF of the $CeT_{1-x}Rh_x$ data. Comparison of the PDF data of $CePt_{0.2}Rh_{0.8}$ and fit results with different Q_{max} confirmed that $Q_{max} = 24\mathring{A}^{-1}$ is the better choice. $Q_{max} = 24\mathring{A}^{-1}$ produces less ripples in the data and the residual factor Rw of the fit is lower than $Q_{max} = 30\mathring{A}^{-1}$ (see Table 2.1).

Q_{max}	$24\mathring{A}^{-1}$	$30\mathring{A}^{-1}$
$a(\mathring{A})$	3.88	3.88
$b(\mathring{A})$	10.94	10.94
$c(\mathring{A})$	4.28	4.28
$u_{Ce}(\mathring{A}^2)$	0.013	0.013
$u_{Rh}(\mathring{A}^2)$	0.025	0.025
$\delta_1(\mathring{A}^2)$	1.82	1.82
scale	1.33	1.33
Rw(%)	0.21	0.24

Table 2.1: PDF refined fit parameters of $CePt_{0.2}Rh_{0.8}$ powder obtained on NOMAD at 289K with fit range $r_{max} = 20\mathring{A}$, results of $Q_{max} = 24\mathring{A}^{-1}$ compared with $Q_{max} = 30\mathring{A}^{-1}$.

We filled our powder $CePd_{1-x}Rh_x$ and $CePt_{1-x}Rh_x$ samples with different Rh concentrations ($x = 0.2, 0.5, 0.6$ and 0.8) in a 2mm quartz tube each. An identical empty

quartz tube was included for background measurement. After labeling the tubes, we mounted the samples on a multistage sample holder and placed them in a cryostat with a liquid argon environment to reach temperatures down to 100K. We run the first scan to find the exact position of each samples on the sample holder. We performed several runs at temperatures 100K and 289K for 6 days in total. We have also conducted a neutron powder diffraction experiment on $Ni_{0.85}V_{0.15}$ samples at room temperature in a similar set up. The data reduction process is done automatically and saved in different formats for further data analysis.

2.4 Atomic pair distribution function (PDF)

For about a century, crystallographic methods have allowed us to extract important structural information based on Bragg reflections. The fast growing complexity of materials has shown that this crystallographic approach is no longer sufficient to study the structure of materials at atomic level as it only yields the average long range structure [55]. However, deviations from the average structure bring about diffuse scattering which contains information about local structure of the material. One approach to uncover the local structure of a material is the atomic pair distribution function (PDF) method. PDF is a powerful tool to study the local atomic structure based on the total scattering, which includes the Bragg and the diffuse scattering. The PDF presents directly the probability of finding two atoms at a inter-atomic distance or the bond length distribution.

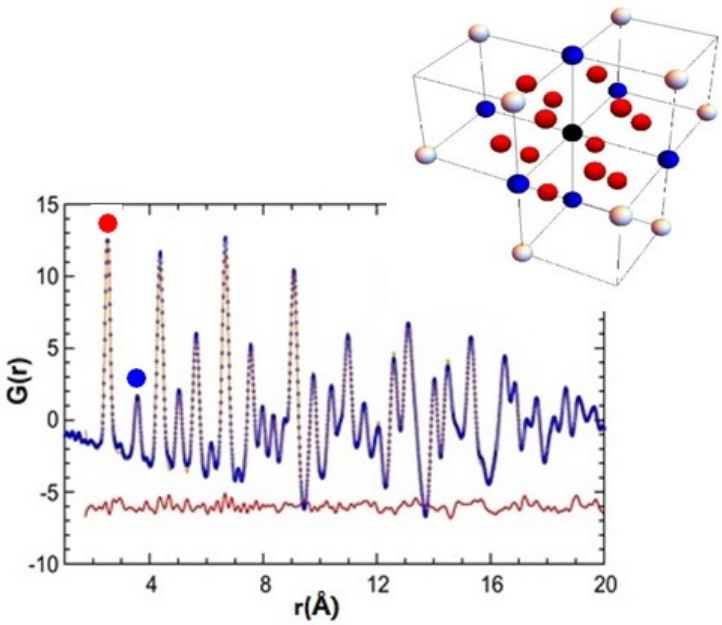

Figure 2.2: PDF of a fcc-lattice.

Fig. 2.2 demonstrates the PDF of a fcc-lattice. Taking the black atom at (0,0,0) as a reference atom, the first and the second nearest neighbor atoms are indicated by red and blue colors, respectively, with inter-atomic distances causing peaks of different height and width. The area below each peak is directly proportional to the number of neighbors at that inter-atomic distance scaled by the scattering length of each atom. The width of each peak corresponds to the distribution of bond lengths caused by the atomic vibrations, correlation parameters, and the instrumental resolution.

The PDF, $G(r)$, is obtained from a neutron or X-ray powder diffraction data through a sine Fourier transform of the normalized total scattering intensity $S(Q)$ [56]

$$G(r) = \frac{2}{\pi} \int_{Q_{min}}^{Q_{max}} [S(Q) - 1] \sin(Qr) dQ, \tag{2.5}$$

where $S(Q)$ is the total structure function containing coherent scattering intensities collected from the material corrected for scattering from empty container, background, and self absorption. $Q = 4\pi sin(\theta)/\lambda$ is the magnitude of the scattering vector, and 2θ is the scattering angle. Since the PDF is related to the bond length distribution of the material weighted by the respective scattering lengths of the constituent atoms, it can be calculated using the relation:

$$G(r) = \frac{1}{r}\sum_i \sum_j \left[\frac{b_i b_j}{\langle b \rangle^2}\delta(r - r_{ij})\right] - 4\pi r \rho_0, \tag{2.6}$$

where the sum is over all pairs of atoms i and j separated by a distance r_{ij}. The scattering length of the ith atom is b_i, $\langle b \rangle$ is the average scattering length of the sample, and ρ_0 is the average pair density function at large distance.

We used PDFgui, a program designed to allow users with a powerful interface for fitting structure models to PDF data [57]. PDFgui is a graphical environment used to refine structural parameters such as lattice constants, isotropic and anisotropic displacement parameters, position and site occupancies. It makes use of a Python package called Matplotlib to plot data from a fit so that the user can easily see the results of the fitting. Since the structural model applies for the specific r-range used, this allows us to study the local structure on different length scales by varying the maximum value (r_{max}). We also used GSAS (General Structure Analysis System), a comprehensive system for the refinement of structural models to both X-ray and neutron diffraction data. The GSAS package can be used with both single-crystal and powder diffraction data (Rietveld analysis), even both simultaneously [58]. We mainly used EXPGUI, a graphical interface for GSAS package which can be used to directly modify the GSAS experiment files with a graphical user interface (GUI) and to invoke the programs inside the GSAS program such as GENLES, FOURIER,

EXPEDT, etc [59].

Ideally, Q-range limits extend from $Q_{min} \rightarrow 0$ to $Q_{max} \rightarrow \infty$. However, due to the finite value of the energy of neutrons produced, we can have only a finite value of maximum momentum transfer Q_{max}. The termination at finite Q_{max} results in a decrease in the real space resolution of the PDF and results in termination ripples. The finite resolution of the instrument in reciprocal space (ΔQ) gives rise to a Gaussian dampening of the PDF peaks given by $exp(-\Delta Q^2 r^2/2)$, where $\Delta Q = Q_{damp}$ is given as an instrument parameter in PDFgui to account for the dampening of peaks as r increases. Another instrumental correction factor to account for changes in the PDF peaks width is Q_{broad}. The PDF peak width stemming from atoms i and j separated by a distance r_{ij} is calculated as [56]

$$\sigma_{ij} = \sigma_{ij}^{'}\sqrt{1 - \frac{\delta_2}{r_{ij}^2} - \frac{\delta_1(T)}{r_{ij}} + Q_{broad}^2 r_{ij}^2}, \tag{2.7}$$

where $u = \sigma_{ij}^{'\,2}$ is an atomic displacement parameter. δ_1 and δ_2 determine the narrowing of nearest neighbor PDF peaks due to correlated motion at high and low temperatures, respectively. The last term containing the parameter Q_{broad} determines the broadening of PDF peaks at very large distances due to the instrument resolution. A detailed description of the instrument is found in [4] and some of the important instrument parameters are given in the Appendix.

2.5 Magnetic ac-susceptibility

AC magnetic susceptibility, χ_{ac}, notices magnetic phase transitions in very small magnetic fields. It gives information about slow magnetization dynamics that may not be accessible in DC measurements, where the field is held constant during the measurement time. χ_{ac} measures the magnetization response, M, created through

a small time dependent magnetic field, H, $\chi = \frac{dM}{dH}$. Varying the frequency of the field, χ_{ac} reveals slow magnetization dynamics. No time dependence is expected in magnetic systems, e.g. in antiferromagnets. But, spin glass (SG) freezing and slow motion of FM dynamics can be recognized at low frequencies. The AC magnetic susceptibility is a complex quantity having an imaginary and real components. The real part called the dispersion ($\chi^{'} = \chi\ cos\varphi$) is in phase with the driving field and the imaginary component, called the absorption ($\chi^{"} = \chi\ sin\varphi$) is out-of-phase, where $\chi = \sqrt{\chi^{'2} + \chi^{"2}}$ is the magnitude and φ is the phase shift relative to the driving field.

Here we measure χ_{ac} through the induction method using a self made pick up coil with a primary coil of Nb-Ti wire which becomes superconducting below 7K. Through an ac-current in a primary coil, an alternating flux is picked up in a secondary coil pair leading to an induction voltage at the end of the so called pick up coil. Ideally, the voltage created in this secondary coil is zero since the two coils of the total coil are wound in opposite direction and therefore compensate. The extra induced voltage due to the sample located in one of the secondary coil is proportional to its magnetic susceptibility

$$V_{ind} = L_{ps} I_0 \omega \chi_{ac}. \tag{2.8}$$

$L_{sp} = \mu_0 \frac{N_s N_p}{l_s l_p} A_s l_s \simeq 0.5$H is the calculated mutual inductance for a long solenoid, where $N_p = 10026$ and $N_s = 8850$ are the number of turns for the primary and the secondary coils, respectively. I_0 is the initial input AC current amplitude, $l_p = 8.64$cm and $l_s = 2.16$cm are the lengths of the primary and secondary coils, respectively, $\omega = 2\pi\nu$ the angular frequency of the driving field, $\mu_0 = 4\pi \times 10^{-7} N/A^2$ is the magnetic permeability, and $A_s = 3.87 cm^2$ is the area of the secondary coil. We calibrated the coil with a superconductor Nb and compared also the signal of a Ni-V sample with

the magnetization data of a SQUID magnetometer. We found consistently half of the calculated value of L_{sp}. The voltage of $1mV$ indicates therefore $\chi \simeq 10$memu, for $I = 0.1$mA at $\nu = 400$Hz with $B_{ac} = 0.01$G. We use LockIn amplifier to pick up phase sensitive the induction voltage of $\chi^{'}$. $\chi^{"}$ signal is too small here to be resolved from the background and is not presented.

2.6 Muon spin rotation (μSR)

A muon is a spin-1/2 particle with a positive or negative charge ($\pm e$) where e is charge of an electron. Beams of polarized muons are produced at different experimental facilities outside the US., e.g. at TRIUMF (Canada), PSI (Switzerland), and ISIS (United Kingdom). The precession and relaxation of their spin can be utilized to investigate the spatial and temporal distribution of magnetic fields in a sample of interest. Since the negative muon μ^- is attracted by the positive nuclei and becomes much less sensitive to the magnetic field of the electron cloud, the positive muon μ^+ is typically used in a μSR experiment as it sits farther away from nuclei [60]. μSR is an abbreviation for muon spin rotation, muon spin resonance, or muon spin relaxation.

Bulk measurements such as magnetization and magnetic susceptibility only probe the uniform response with no spatial information, they can therefore only give first indications of magnetic clusters in our sample. Complimentary techniques such as μSR and neutron scattering should reveal more microscopic information such as the length scales and dynamics of the magnetic clusters. Due to muon's large magnetic moment ($\mu_\mu \simeq 3.2\mu_p \simeq 8.9\mu_n$), polarization in zero field, and their implantation on interstitial sites, μSR is sensitive enough to probe very small internal magnetic fields (down to 10^{-5}T) and their local distribution in a sample [60] [61]. It is an excellent method to recognize small magnetic moments.

2.6.1 Muon production, decay, and polarization

High energy proton beams (600-800MeV) of kinetic energy are fired into a target (typically graphite) to produce pions (π^+), and within very short lifetime ($\sim 26ns$), pions decay into muons as [60]

$$\pi^+ \longrightarrow \mu^+ + \nu_\mu, \tag{2.9}$$

where ν_μ is a muon-neutrino. The pion is spinless and the neutrino helicity is (-1) i.e. its spin and linear momentum are antiparallel. Conservation of linear and angular momenta dictates that the muon is fully polarized. After successive inelastic scattering (involving Coulomb interactions) and collisions with atoms in the sample, the muons finally localize in interstitial sites and decays after some time t with probability $\sim e^{-t/\tau_\mu}$, where $\tau_\mu = 2.2\mu s$ is the lifetime of the muon. The muon decay process involves the emission of a positron and two neutrinos

$$\mu^+ \longrightarrow e^+ + \nu_e + \bar{\nu_\mu}. \tag{2.10}$$

The above decay process involves weak interaction and thus does not conserve parity. In addition, momentum must be conserved which leads to the emission of a positron predominantly along the direction of the muon spin when it decays [60].

2.6.2 Evolution of the muon spin and principles of the μSR experiment

The primary purpose of a μSR experiment is to determine the polarization of the implanted muons and extract important information about the spatial and temporal local magnetic field distribution of a sample.

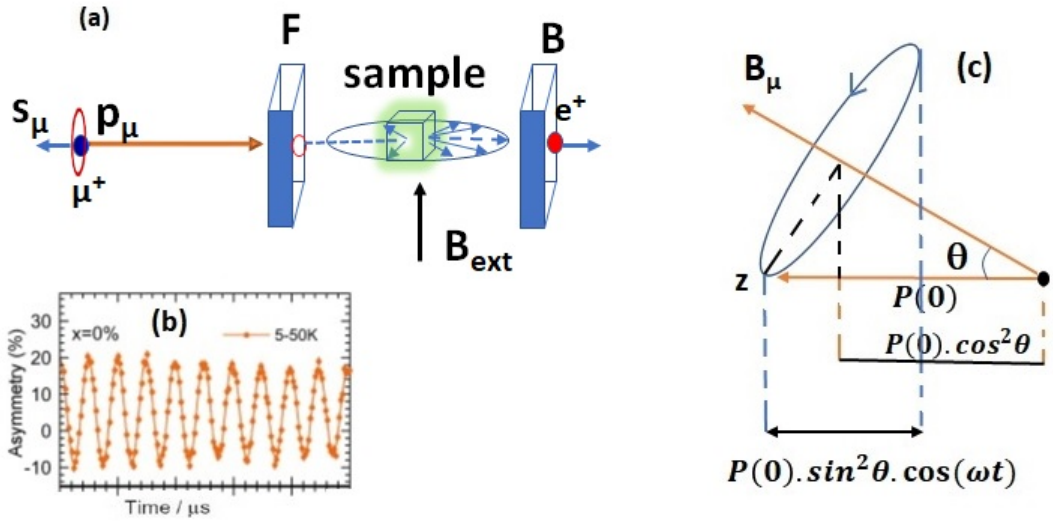

Figure 2.3: (a) Schematic diagram of a μSR experiment. A spin-polarized beam of muons is implanted in a sample. After decay, positrons are detected in either a forward (F) or backward (B) detector. (b) The asymmetry $A(t)$ vs time for a uniform magnetic field showing single frequency precession. (c) Muon spin precession in a local magnetic field.

Fig. 2.3 demonstrates the schematic diagram of a typical μSR experiment. A muon with its spin aligned antiparallel to its momentum is implanted in a sample (see for example Fig. 2.3(a)). Depending on the local magnetic field of the muon location, the muon spin starts precessing (see Fig. 2.3(c)) and decays with a lifetime ($\tau = 2.2\mu s$) by emitting a positron in the direction of its spin. The positron is then detected by either the forward (F) or backward detector (B) and the respective number of positrons are counted. The time evolution of the number of positrons detected in the backward and forward detectors is given by exponential functions $N_B(t)$ and $N_F(t)$, respectively. The difference is recorded as the asymmetry. The time evolution of the muon's polarization function is experimentally obtained by examining the asymmetry

function given by [60, 62]

$$A(t) = aP_i(t) = \frac{N_F(t) - \alpha N_B(t)}{N_F(t) + \alpha N_B(t)}, \tag{2.11}$$

where α is a calibration parameter correcting the asymmetry between the front and back detectors due to differences in efficiency and other factors. It is one of the adjustable parameters in a μSR data analysis using a program called WIMDA [63] and its value is typically between 1 and 2 depending on the instrument used. a is the initial asymmetry at $t = 0$, and $P_i(t)$ is the normalized polarization function with the label i denoting the direction in Cartesian coordinates along which the muon polarization is measured. An example of an asymmetry spectrum as a function of time for a ferromagnet (with single precession frequency) is shown in Fig. 2.3(b).

The polarization function $P_i(t)$ of a muon implanted in a sample in a local magnetic field (B_{loc}) can be determined solving Larmor's equation and certain local filed distribution result in simple polarization functions. If all the muon spins precess in the same magnetic field oriented at an angle θ from the initial muon spin ($S_\mu(0)$), the projection of the muon spin along its initial direction (the normalized polarization function) produces [60, 61]

$$P_i(t) = \frac{\mathbf{S}_\mu(\mathbf{t}).\mathbf{S}_\mu(\mathbf{0})}{S_\mu^2(0)} = \left[cos^2\theta + sin^2\theta\ cos(\omega_\mu t)\right], \tag{2.12}$$

where $\omega_\mu = 2\pi\nu_\mu = \gamma_\mu|\mathbf{B_{loc}}|$ is the Larmor frequency, $\gamma_\mu = 851.6\ Mrad\ s^{-1}T^{-1}$ is the muon gyromagnetic ratio. $P_i(t)$ displays the properties of the magnetic field at the muon site and this is the result on which the entire μSR experiment is based. The polarization function in Eq. 2.12 depends on the size and orientation of the local magnetic field, that can be applied externally or present internally. The simplest case is a constant field with all muons submitted to the same local field on average. If

the initial muon spin is perpendicular to the direction of the local field, the first term in Eq. 2.12 vanishes and the polarization function reduces to $P_i(t) = cos(\omega_\mu t)$. This indicates that the muons precess with an angular frequency ($\omega_\mu = \gamma_\mu |\mathbf{B_{loc}}|$) and the local field can be easily obtained experimentally from the precession frequency. For a general distribution of local fields $D_V(\mathbf{B_{loc}})$, the polarization function becomes [60,61]

$$P_i(t) = \int \left[cos^2\theta + sin^2\theta \; cos(\omega_\mu t)\right] D_V(\mathbf{B_{loc}}) d^3\mathbf{B_{loc}}. \tag{2.13}$$

If, for example, the local magnetic field follows a Gaussian distribution with width (Δ/γ_μ) centered around zero, the resulting polarization function reduces to

$$P_Z(t) = \frac{1}{3} + \frac{2}{3} e^{-\Delta^2 t^2/2} \left(1 - \Delta^2 t^2\right), \tag{2.14}$$

where Δ^2 gives the variance of the field distribution. Eq. 2.14 is commonly known as the Kubo-Toyabe function [64]. In Chapter 4, we will see that this form is a good description for the disordered ferromagnet and will discuss other distribution functions. Our μSR experiments were performed on the DOLLY instrument at the Swiss Muon Source (SμS), Paul Scherrer Institut and on the MuSR instrument at the ISIS facility. We collected data of several Ni-V concentrations wrapped in silver foil [2, 3].

Chapter 3

Structural study of Ni-V using PDF method

Nickel (Ni) is one of the few elemental ferromagnets with a critical temperature T_C well above room temperature ($T_c \simeq 627°C$) [65]. Substitution of Ni by an other d-metal like vanadium (V) suppresses the magnetic order leading to a quantum phase transition from a ferromagnetic (FM) ground state to a paramagnetic (PM) ground state. The transition temperature (T_c) is reduced with increasing V concentration down to zero at the quantum critical point ($x_c \simeq 0.116$) [1]. V has less d-electrons than Ni. This charge contrast creates magnetic inhomogeneities. Randomly distributed Ni-rich regions form interrupted by V locations. Independent Ni-rich regions are called here magnetic clusters.

Previous studies of bulk magnetization data revealed the existence of these magnetic clusters which are indications of a quantum Griffiths phase [1]. Since the distribution of magnetic clusters is expected to depend strongly on the location of the V atoms and the local Ni-environment, an investigation of the magnetic and chemical structure of our samples is required to reveal the origin of magnetic clusters. This chapter focuses on a detailed chemical structure investigation of Ni-V.

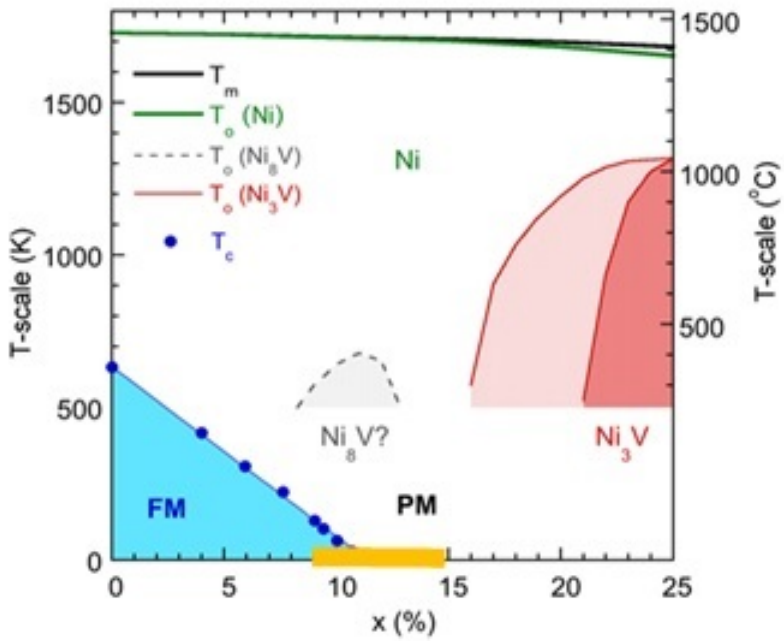

Figure 3.1: Chemical and magnetic phase diagram of Ni-V.

$Ni_{1-x}V_x$ is expected to crystallize in the face-centered cubic (fcc) structure for lower V concentration ($x \leq 0.15$) where magnetic clusters are relevant (see the solid yellow line in Fig. 3.1). Ordered structures in the binary Ni-V alloy are only present at higher V concentrations. The Ni_3V [66] superstructure forms at $x = 0.25$ (see Fig. 3.1). Although the phase diagram of Ni-V shows that a fcc-lattice with random occupation is very likely for $x \leq 0.15$, it is impossible to rule out V clusters and short range correlation in specific samples. It is known that the growth and annealing conditions can modify the structure and local composition in Ni-alloys. To look at the local environment of Ni, we use the PDF analysis, a powerful technique to study the local structure of materials at various length scale. In the following sections, I will present the experimental details and the results obtained from the PDF analysis.

The data were collected on NOMAD, SNS at room temperature at a Ni-V powder sample with $x = 0.15$. These results are also compared with the results obtained from $Ni_{0.85}V_{0.15}$ pellets at low temperature, on NPDF [42, 67].

Major results from this chapter are summarized in Ref. [42].

3.1 Random atomic distribution model

The pair distribution function G(r) of the $Ni_{0.85}V_{0.15}$ powder data at $x = 0.15$ is shown in Fig. 3.2. A single phase fcc-lattice with random site occupation describes the data very well within the fit range of $1.5\AA < r < 20\AA$. The difference between the data (blue dots) and the fit (orange line) is very small and shown by the red line underneath with a weighted residual factor (Rw) of 8.42%.

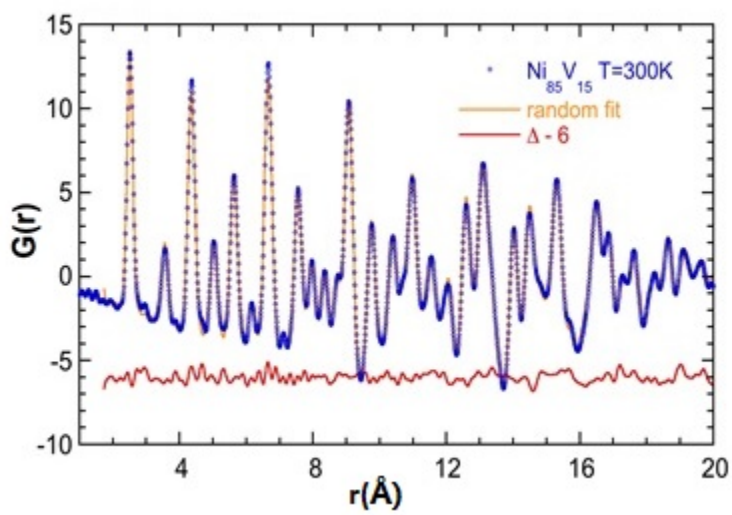

Figure 3.2: PDF of $Ni_{0.85}V_{0.15}$ taken at 300K on NOMAD with random fit, the difference Δ = data-fit is shown shifted down by 6 units with $Q_{damp} = 0.033\AA^{-1}$ and $Q_{broad} = 0.04\AA^{-1}$.

The instrumental parameters were adjusted to improve the fit quality. The refined parameters such as the lattice constant (a), the isotropic atomic displacement parameter (u), the correlation parameter (δ_1), and the corresponding weighted residual values (Rw) are shown in Table 3.1. The results obtained from a different Ni powder data on NOMAD are included for comparison [4]. Here, we used higher Q-values than their default values for a better fit, consistent with the expected strain introduced in our sample during the fast cooling process (quenching).

x	0%	15%
$a(\mathring{A})$	3.5252	3.5608
$u(\mathring{A}^2)$	0.0011	0.0077
$\delta_1(\mathring{A}^2)$	—	1.69
scale	—	0.693
Rw(%)	6.2	8.4

Table 3.1: PDF refined fit parameters of $Ni_{0.85}V_{0.15}$ powder obtained on NOMAD at 300K for fcc random model with fit range $r_{max} = 20\mathring{A}$, $Q_{damp} = 0.033\mathring{A}^{-1}$, and $Q_{broad} = 0.040\mathring{A}^{-1}$ compared with the results on pure Ni powder data with $Q_{damp} = 0.018\mathring{A}^{-1}$, and $Q_{broad} = 0.036\mathring{A}^{-1}$. The result for $x = 0$ is obtained from Ref. [4].

As can be seen in Table 3.1, $Ni_{0.85}V_{0.15}$ has larger lattice parameters a and u than the pure Ni. This is expected and understood through the introduction of larger V atoms with atomic radius r_V compared to the smaller Ni atoms with radius r_{Ni}. The isotropic ADP (u) is the mean square atomic displacement of atoms from equilibrium position of one element averaged over time and site. It consists of both static part and dynamic part, $u = \langle u^2_{dyn} \rangle + \langle u^2_{stat} \rangle$. Since the strongest scattering signal comes

from Ni, we consider only the isotropic ADP of Ni, $u = u_{Ni}$ and we set $u_V = u_{Ni}$ in all our models. The dynamic ADP dominates at high temperature as in our case due to thermal motion while at low temperature, zero point motion and static defects contribute significantly. Table 3.1 shows an increase of isotropic ADP as compared to the result obtained from pure Ni data. The increase includes static defects due to the introduction of the larger V atoms.

Previously, the x-dependence of the structural parameters was studied on several pellets of $Ni_{1-x}V_x$ at low T [42]. The low temperature data show that the lattice constant (a) of the fcc-lattice increases linearly with V concentration x, $a(x) = a_0(1+bx)$, with the fit parameters, $a_0 = 3.5153\mathring{A}$ and $b = (r_V - r_{Ni})/r_V \approx 0.05$, consistent with Vegard's law. The atomic displacement parameter follows the expected bond length variance of two neighbors with $u(x) = \frac{1}{2}\sigma = u_0 + \frac{1}{8}b^2a_0^2x(1-x)$ for random occupation with the same values of a_0 and b obtained in fitting $a(x)$ [42].

3.2 Alternative cluster and super structure models

In the previous section, we have seen that the PDF of our sample is well explained by a fcc-lattice with random occupation of V and Ni as ideally expected in the concentration regime, $x < 0.25$. However, possible deviations such as the formation of V-clusters in the fcc-lattice or a chemical ordered structure of V and Ni forming an alternate pattern with isolated V sites should be considered and compared with the random model. We note that the PDF is very sensitive to local correlations and can discriminate between these different V and Ni environments. V-clusters and chemical ordered structures lead to different local Ni-Ni coordination. In a random occupation, the average nearest Ni-neighbors of a Ni-site are reduced from $z = 12$ at $x = 0$ to $z = 12(1-x) = 10.2$ at $x = 0.15$. We therefore test alternative Ni-environments

caused by V-clusters or partial chemical structure formation by focusing on the PDF of the same $Ni_{0.85}V_{0.15}$ sample in a narrow range of $r \simeq 7\mathring{A}$.

For a V-cluster model, we constructed a supercell containing 256 atoms of which 38 V are placed together in a spherical arrangement on an expanded fcc-lattice ($4 \times 4 \times 4$ cubic unit cells). The V-clusters are about $7\mathring{A}$ in size, $14\mathring{A}$ apart center to center, and $7\mathring{A}$ apart edge to edge. By analyzing the short range correlation with $r_{max} \simeq 7\mathring{A}$, slightly below the distance between the clusters, allows us to study the effect of a V-cluster without the cluster-cluster correlation introduced in this periodic model. Fig. 3.3 shows both the random fit and the V38 model fit with reduced $r_{max} \simeq 7\mathring{A}$ for $Ni_{0.85}V_{0.15}$. Both models do not show obvious deviations in peak intensity. A change can be noticed in the difference between data and fit for the first peak. The cluster model (green line) shows more deviations than the random model (red line). The V-cluster model results in a higher Ni-Ni first neighbor coordination (z) than the random model.

Model	Rw(%)
fcc-random	6.93
V38 cluster	8.22
Ni_8V	7.96
Ni_3V	12.30

Table 3.2: Fit quality of different models describing the local pair correlations in $Ni_{0.85}V_{0.15}$ powder data set at 300K. The weighted residual factor Rw is listed for a fit range $1.75\mathring{A} < r < 7.1\mathring{A}$.

However, the better fit with reduced Rw value (as shown in Table 3.2) and lower

z is found to be the random fit compared to the cluster model. The instrumental parameters are kept the same for all models ($Q_{damp} = 0.018\mathring{A}^{-1}$ and $Q_{broad} = 0.02\mathring{A}^{-1}$), and the fit regime is $1.75\mathring{A} < r < 7.1\mathring{A}$. It is worth mentioning that other cluster models with smaller cluster sizes give similar result (Rw$\sim$ 8%).

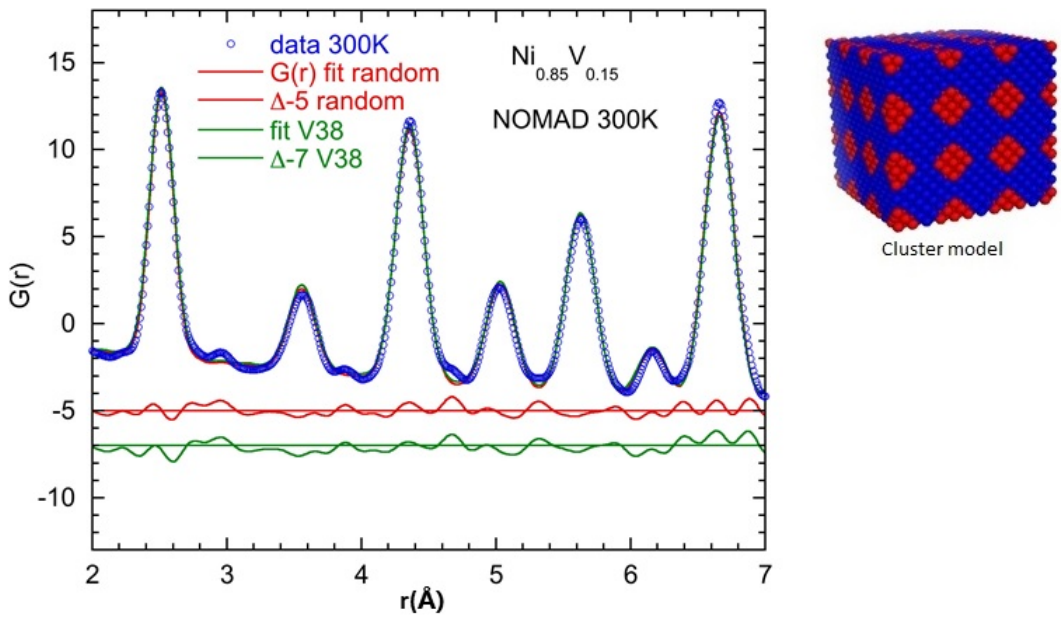

Figure 3.3: Comparison of V-cluster model (green) with random model (red) of local PDF. $Ni_{0.85}V_{0.15}$ data (open symbol), models and difference (solid line) are shown. The upper right corner shows the V38 cluster model.

Other deviations from randomly occupied fcc-lattice are chemical ordered super structures. According to the phase diagram, Ni_3V is one of the possible ordered structures that forms from the disordered fcc phase below $T_0 = 1045°C$ in a concentration range $x \simeq 0.25$ depending on sample growth and annealing conditions [66]. It crystallizes in the SO_{22} structure, a body centered tetragonal structure with 2 fcc unit cells along the c-direction. V has only Ni neighbors and Ni has 4 V neighbors resulting

in a very small coordination number, $z = 8$. We probed the short range correlation preparing the Ni_3V structure using a $(1 \times 1 \times 2)$ fcc supercell with V-atoms at the origin and body center. Fig. 3.4 shows the obvious deviations in $G(r)$ at the first peak (see for example the difference between data and fit presented by a black line) resulting in the largest residual Rw shown in Table 3.2 ($Rw = 12.3\%$).

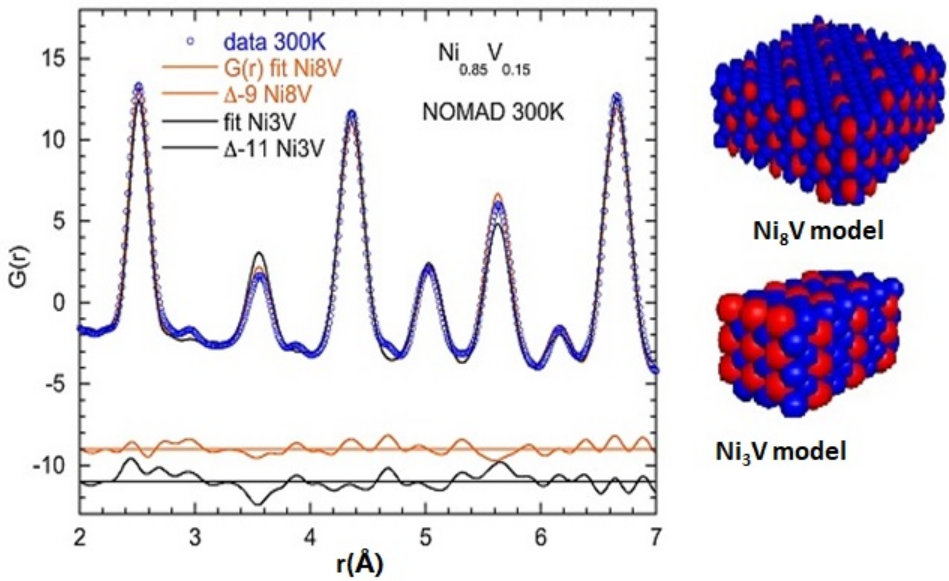

Figure 3.4: Comparison of different ordered phases, Ni_3V model (black) and Ni_8V model (orange) of local PDF. $Ni_{0.85}V_{0.15}$ powder data (open symbol), models, and differences (solid lines) are shown. On the right side, the structure of Ni_3V and Ni_8V are shown.

Another potential chemical ordered structure is Ni_8V. A larger radius ratio between the two metallic elements is required to stabilize long range order, but short range order could be relevant. Ni_8V and Ni_8Ta have a large enough radius ratio to order in this "Ni_8Nb" structure. Replacing Nb or Ta partially with V maintains the ordered structure and a chemical disorder-order transition at $T_0 = 405°C$ has been

extrapolated for pure Ni_8V [68]. The Ni_8Nb-structure is a body centered tetragonal structure with the Nb or V-site having no similar neighbors whereas the Ni-site has 1 or 2 Nb(V) neighbors resulting in an average Ni-Ni first neighbor count of $z = 10.5$ which is close to the Ni-Ni coordination $z = 10.2$ resulting from pure random distribution of atoms for $x = 0.15$. Once again, we probed the short range correlation preparing the Ni_8V structure using a $(3 \times 3 \times 1)$ fcc-supercell with V at the origin and face center. The PDF data of $Ni_{0.85}V_{0.15}$ is modeled for a short range ($r_{max} \simeq 7\mathring{A}$) in PDFgui under the same condition as the random model. The difference between data and model is shown in Fig. 3.4 by an orange line. The residual $Rw = 7.96\%$ is small but still larger than the residual $Rw = 6.93\%$ for the random model.

3.3 Discussion

We have demonstrated that the local PDF is a powerful method to probe the local Ni-environment in the $Ni_{0.85}V_{0.15}$ sample. No secondary ordered phase beside the fcc-lattice is found. The fcc-lattice with random occupation is the best model. V-cluster models and ordered phases remain the worst description. These results do not support phase segregation of V and Ni rich regions. Other ordered phases are not observed, possible short range correlations must be weak for $x = 0.15$. These PDF powder data strongly support the previous subtle results of the pellet samples that Ni-V remains a solid solution with a random V distribution up to $x = 0.15$ and that in particular V-cluster formation can be ruled out.

Chapter 4

Magnetic clusters in Ni-V

As we discussed in the previous chapter, substitution of Ni by V leads to magnetic inhomogeneities relevant to the quantum critical properties of Ni-V. It is expected that V strongly suppresses the magnetic moment of the neighboring Ni atoms and creates magnetic Ni-rich regions and large nonmagnetic regions. If the Ni-rich regions are sufficiently separated, they remain independent magnetic clusters marked by the green circle (as shown in Fig. 4.1).

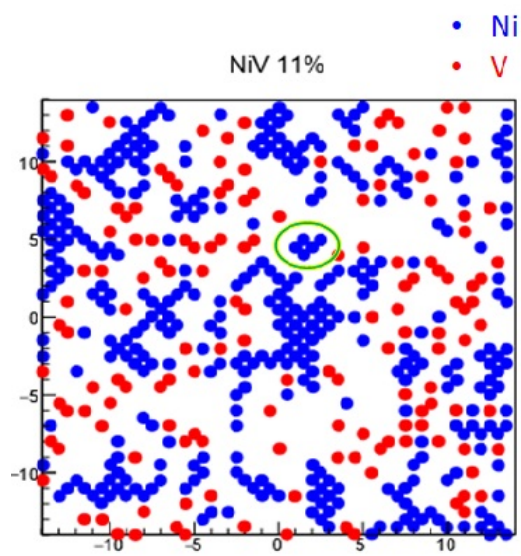

Figure 4.1: Random model of $Ni_{0.89}V_{0.11}$ on fcc lattice with magnetic Ni (blue dots), V (red dots), and "nonmagnetic" Ni if adjacent to V (white space). Green circle marks a magnetic cluster.

The spatial distribution of these magnetic clusters and their fluctuations should

be responsible for the unconventional properties close to the quantum critical point (QCP) [1, 2]. Signs of non-Fermi liquid behavior were observed in this system [1]. In particular, a quantum Griffiths phase was recognized by anomalous nonuniversal power-laws in the magnetization observed by varying temperature and magnetic fields [1]. To explore further the range of the quantum Griffiths phase and more details of the magnetic cluster, different complimentary bulk and local magnetic investigations are necessary. First, I report the relevant magnetization and μSR results from our group. Then, I focus on the specific μSR studies to reveal the fluctuating magnetic clusters.

4.1 Magnetization study of quantum Griffiths phase

First signatures of fluctuating magnetic clusters in Ni-V were noticed above the quantum critical concentration ($x \geq 11.6\%$) in the PM regime [1]. To follow the notation of published results, the V concentration x is given here in percentage, ranging from $x = 0$ to 15%. The dependence of the low-temperature magnetization M on the magnetic field H is well described by anomalous power laws $M \sim H^{\alpha}$ on the paramagnetic side in a wide range of magnetic fields. The exponent α is strongly x dependent, it increases with distance to the quantum critical point [1]. Similar power laws ($M - M_0 \sim H^{\alpha}$) successfully describe the low temperature magnetization data on the ferromagnetic side ($x < 11.6\%$), where M_0 is the spontaneous magnetization. α is strongly x dependent and decreases towards zero at the critical concentration $x_c \simeq 11.6\%$ (see Fig. 4.2) [2].

The difference $\Delta M = M_{high} - M_0$ indicates the contribution of magnetic clusters to the ordered state at high field, where M_{high} is the magnetization at the highest

magnetic field, $H = 50$kOe. This magnetic cluster contribution becomes more relevant towards the critical concentration. The ratio, $f_{cl} = \Delta M/M_{high}$, gives the fraction of the magnetic clusters in the ferromagnetic phase.

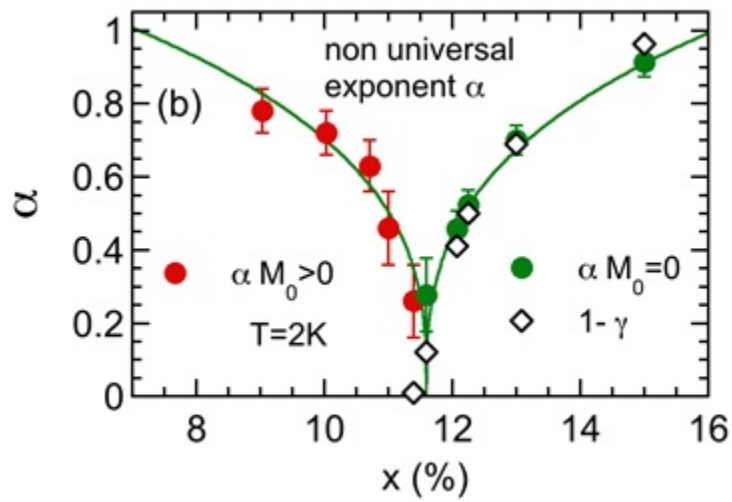

Figure 4.2: Red symbols represent exponents α obtained from low temperature magnetization in the FM phase. Green symbols show exponents α from power laws fit using the magnetization data and open symbols indicate exponents obtained from susceptibility, both in the PM phase. Solid line indicates fit to model $\alpha(x) \sim |x - x_c|^{\nu\psi}$, with $\nu\psi = 0.34$ and $x_c = 11.6\%$. From Ref. [2].

In the following sections, we will have a detailed microscopic insight into these magnetic clusters in the ferromagnetic phase utilizing the advantage of μSR in accessing the distribution of local magnetic fields in the sample.

4.2 μSR study of quantum Griffiths phase

Fig. 4.3 presents an overview of the muon asymmetry data of $Ni_{1-x}V_x$ for several V concentrations x at low temperatures in zero-field. In pure Ni ($x = 0$), the

asymmetry shows a nearly undamped single frequency precession verifying a uniform ferromagnetic order.

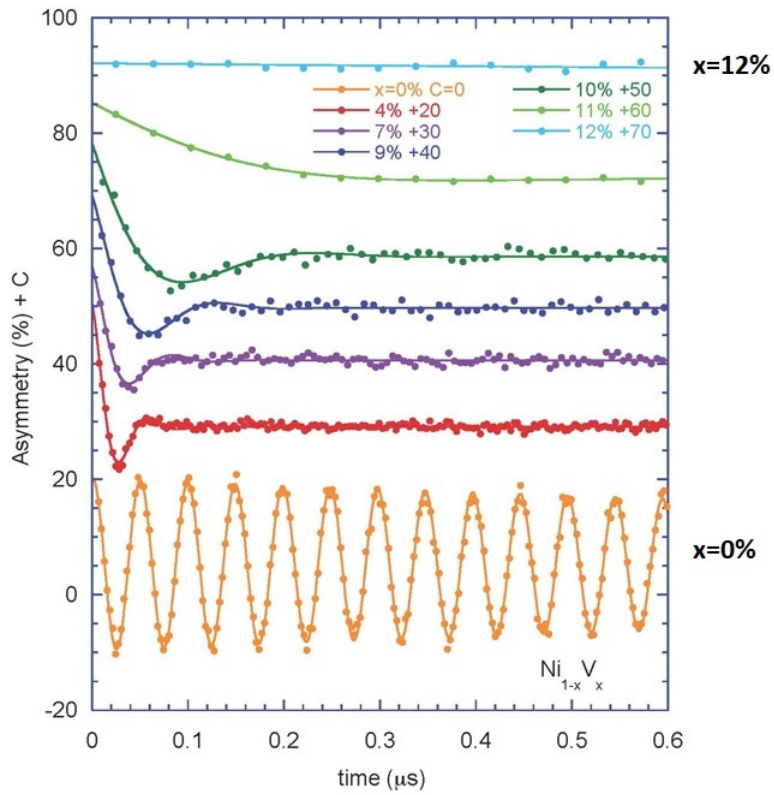

Figure 4.3: Zero-field μSR asymmetry $A(t)$ vs time of $Ni_{1-x}V_x$ for several V concentrations x indicated. Symbols represent data taken at low temperatures ($1.5K < T < 10K$). Solid lines represent fits to selected models. Each data is shifted by a constant C to avoid any overlap. From Ref. [3].

At the highest V concentration ($x > x_c$), however, a very weak depolarization is observed that can be modeled by a simple exponential decay as

$$A(t) = A_{PM} P_{PM} = A_{PM} e^{-\lambda t}, \tag{4.1}$$

where A_{PM} is the amplitude of the asymmetry and $\lambda \sim 1/\nu$ is the depolarization rate, a measure of the fluctuation rate (ν) of magnetic clusters. As can be seen in

Fig. 4.3, the other concentrations ($0 < x < 12\%$) show a single dip without further oscillations. The dip gets shallower towards higher concentrations and finally disappears beyond the critical concentration. This can be understood as the effect of multiple frequency oscillations with some distribution width(s), Δ_i. Here, we mainly focus on two concentrations ($x = 10\%$ and $x = 11\%$) that are close to the quantum critical point but on the ferromagnetic side of the phase transition.

4.2.1 Results of $x = 10\%$

The asymmetry A(t) extracted from the μSR data for $x = 10\%$ is presented in Fig. 4.4(a) at several temperatures. At low temperatures, it shows a single dip without further oscillations revealing inhomogeneous ferromagnetic order. A Gaussian distribution of local magnetic fields of width Δ fits the asymmetry well at low temperature with a form $A(t) = A_{FM}P_{FM}$ with

$$P_{FM} = P_{KT}(t;\Delta) = \frac{1}{3} + \frac{2}{3}e^{-\Delta^2 t^2/2}\left(1 - \Delta^2 t^2\right). \tag{4.2}$$

P_{KT} is the well known Kubo-Toyabe (KT) depolarization function described in Eq. 2.14. For all temperatures, $A(t)$ can be modeled by two components and a small additional constant background contribution (A_{BG}) as

$$A(t) = A_{PM}(T)P_{PM} + A_{FM}(T)P_{FM} + A_{BG}, \tag{4.3}$$

where $A_{PM}(T)$ and $A_{FM}(T)$ are temperature dependent amplitudes of the paramagnetic and the ferromagnetic components, respectively. The small temperature-independent contribution (A_{BG}) stems mainly from the silver sample holder.

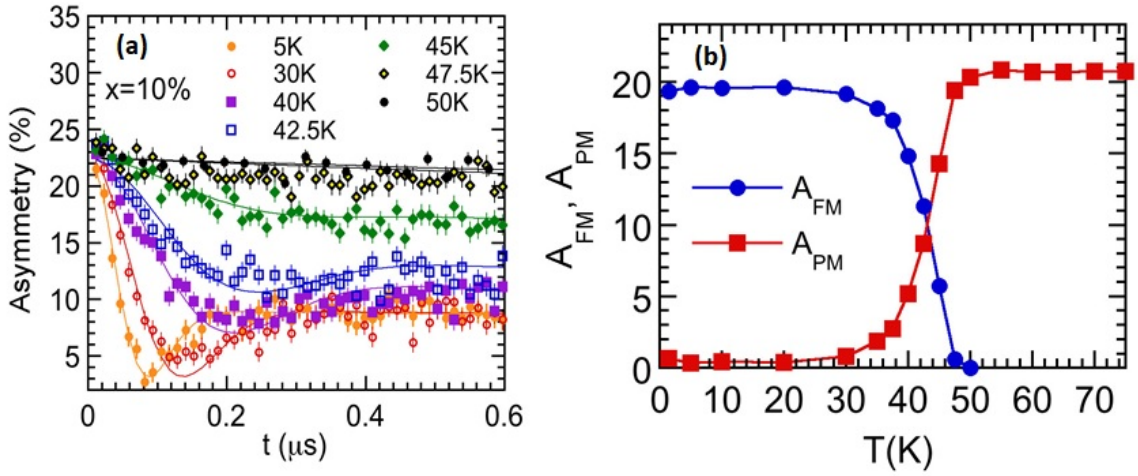

Figure 4.4: (a) Zero-field μSR asymmetry $A(t)$ vs time of $Ni_{1-x}V_x$ for $x = 10\%$. Symbols represent data taken at several temperatures. Solid lines represent fits to Eq. 4.2. (b) Evolution of amplitudes of the FM component (A_{FM}) and the PM component (A_{PM}) as a function of temperature T. From Ref. [2].

The temperature dependence of the amplitudes A_{FM} (blue symbols) and A_{PM} (red symbols) are shown in Fig. 4.4(b). $A_{FM} > 0$ marks the onset of the ferromagnetic order at $T_C \simeq 47K$. The FM order dominates the magnetic cluster contribution represented by A_{PM} at sufficiently low temperatures. The FM ordered fraction evaluated by the ratio $f_{FM} = A_{FM}/(A_{FM} + A_{PM})$ is close to 100% at low temperature.

4.2.2 Results of $x = 11\%$

Approaching the quantum critical point from the FM side of the quantum phase transition, we next focus on the $x = 11\%$ sample. Magnetization measurements indicate that it is a ferromagnet and no indication of a cluster glass transition is noticed in magnetic ac-susceptibility measurements [69]. The zero-field asymmetry is plotted as a function of time for several temperatures in Fig. 4.5(a). It shows a strong

depolarization with a shallow dip making the static Kubo-Toyabe fit impossible even at the lowest temperature.

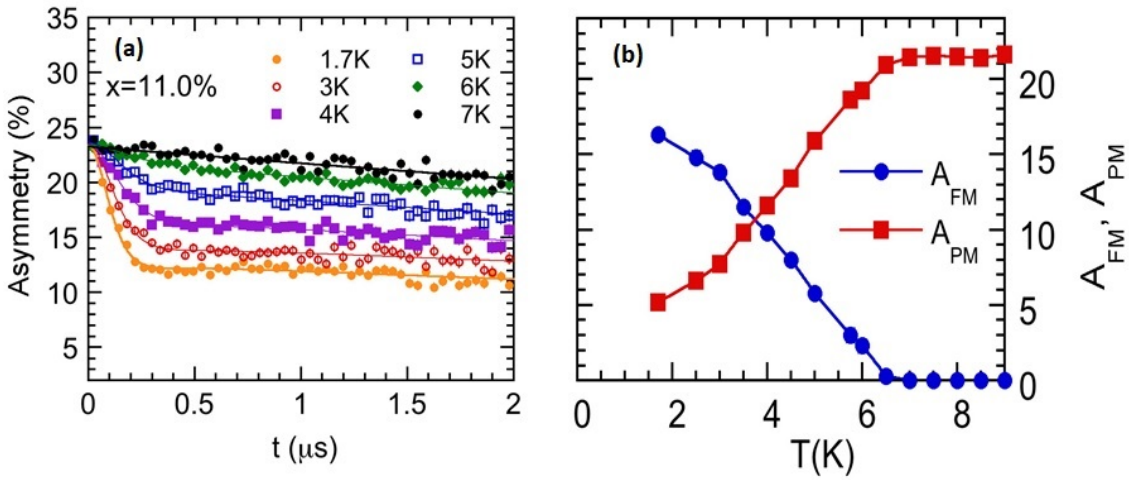

Figure 4.5: (a) Zero-field μSR asymmetry $A(t)$ vs time of $Ni_{1-x}V_x$ for $x = 11\%$. Symbols represent data taken at several temperatures. Solid lines represent fits of the form in Eq. 4.4 (b) Evolution of amplitudes of the FM component A_{FM} (blue symbols) and the PM component A_{PM} (red symbols) as a function of temperature T. From Ref. [2].

Data taken in longitudinal fields also exclude a dynamic KT form [2]. An alternative model that can describe multiple field distributions with different widths is required to account for the fast time dependence of $A(t)$. The Gaussian broadened Gaussian model with

$$P_{GBG}(t;\Delta,R,\nu) = \frac{1}{3}exp(-\frac{2}{3}\nu t) + \frac{2}{3}((1+R^2)/N)^{3/2}(1-(\Delta t)^2/N)exp(-\frac{1}{2N}(\Delta t)^2), \tag{4.4}$$

fits the data well [2](see Fig. 4.5(a) for R=0.8). $N = 1 + R^2 + R^2\Delta^2 t^2$, where $R = \Delta_w/\Delta_0$ gives the ratio of the widths of each Gaussian distributions (Δ_w) to the central

width (Δ_0), $\Delta_{eff} = \Delta = \sqrt{\Delta_w^2 + \Delta_0^2}$ is the effective field distribution width, and ν is the fluctuation rate. The temperature dependence of the amplitudes of the PM (red symbols) and the FM (blue symbols) component is shown in Fig. 4.5(b). The onset of A_{FM} indicates ferromagnetic order at $T_C \simeq 6.5K$ which is in agreement with the T_C obtained from magnetic measurements [1]. A_{FM} does not saturate and remains reduced towards the lowest temperature. At the lowest temperatures, a sizable paramagnetic contribution A_{PM} remains leading to a cluster fraction $f_{cl} = 1 - f_{FM}$ of $\sim 20\%$. This is an indication of the existence of fluctuating magnetic clusters that remain at low temperatures. The μSR-based cluster fraction ($f_{cl} = A_{PM}/(A_{PM}+A_{FM})$) is obtained for all x using Kubo-Toyabe and Gaussian broadened Gaussian models of $A(t)$ at the lowest temperature T.

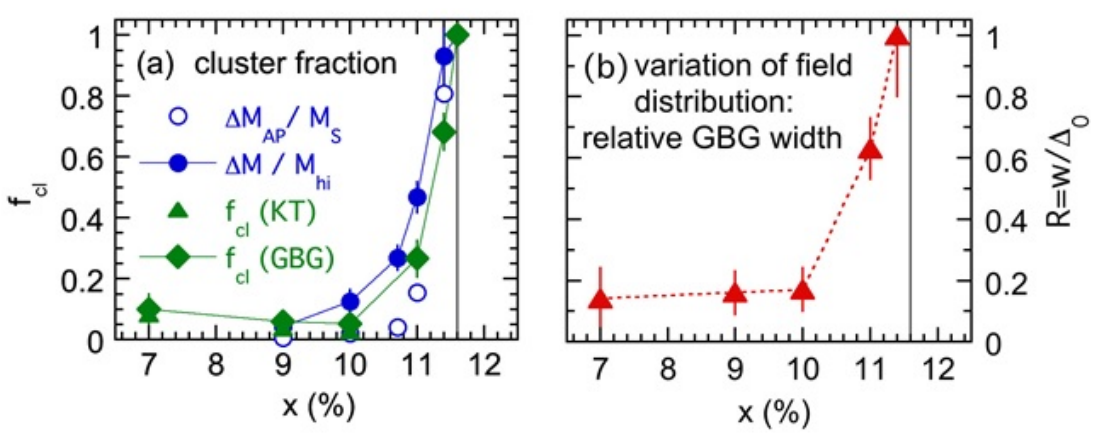

Figure 4.6: (a) Cluster fraction f_{cl} vs x from magnetization and μSR analysis. (b) Relative width R vs x of the Gaussian-broadened Gaussian (GBG) model. From Ref. [2].

As can be seen in Fig. 4.6(a), these cluster fractions (f_{cl}) are consistent with the

estimates obtained from magnetization data and show that clusters get more relevant close to the critical concentration. For consistency, all FM samples have been fitted with $P_{FM} = P_{GBG}$ at the lowest temperature. The relative GBG width, R, remains small for $x \leq 9\%$ confirming the KT form (with $R = 0$), and then increases towards x_c as the cluster fraction rises, indicating an increased magnetic inhomogeneity towards the quantum critical point (see Fig. 4.6(b)).

4.3 SANS results

Previous small angle neutron scattering (SANS) data have shown that the magnetic intensity seems to be too small to be measured in Ni-V with $x = 12\%$, a PM sample in the Griffiths phase regime. New SANS experiments at performed at a weak FM sample with $x = 11\%$ were successful and could resolve magnetic intensity. To extract the magnetic contribution (ΔI), we subtracted data collected at high field (B) or at high temperature (T) as nuclear background estimate (BG) from the total intensity (I). Fig. 4.7 shows the total intensity that is enhanced due to chemical disorder and the magnetic intensity with a fraction of about $1 - 10\%$. Such differences include large errors since the sample can move in between the two settings and the background (BG) can be temperature and magnetic field dependent. We recognize a clear temperature dependence in ΔI around $Q \simeq 0.05\mathring{A}^{-1}$ from $T_C = 7$K to lower temperatures. It looks promising that the remaining magnetic intensity at low temperatures is related to the magnetic cluster distribution. But, whether the increasing signal ΔI towards low Q is really magnetic or an artifact of the BG estimate has to be investigated further in a future experiment.

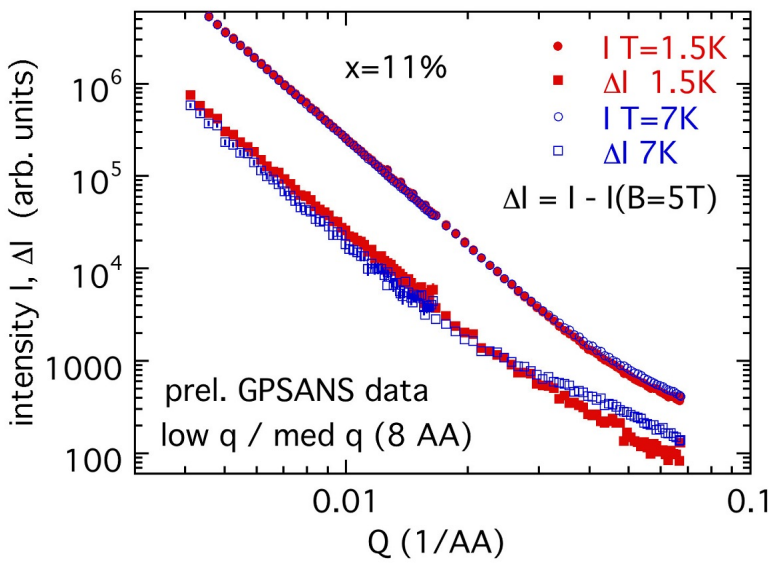

Figure 4.7: SANS intensity I of Ni-V for $x = 11\%$ as a function of scattering vector Q measured at different temperatures $T_C = 7$K and $T = 1.5$K. For ΔI, data at $B = 5$T are subtracted as background. Data collected on GPSANS at HFIR, ORNL.

For comparison, we investigated $x = 10\%$ sample, a stronger FM with $T_C = 47$K. The data is presented in Fig. 4.8 for unpolarized neutron beam on NG7 (large circles) and GPSANS (small circles). We subtracted the higher field data to extract the magnetic intensity. The magnetic intensity ΔI is reduced significantly for temperatures below T_C. Again, the steeper upturn of ΔI towards low Q remains to be checked carefully. In addition, we also tested a full polarized set up that was feasible and produced consistent data with sufficient statistics in the higher Q range $0.02\mathring{A}^{-1} \leq Q \leq 0.1\mathring{A}^{-1}$ (see Fig. 4.8). An estimate of spin flip data (SFc) (black squares) matches the unpolarized ΔI data (blue circles) for $T = 47$K.

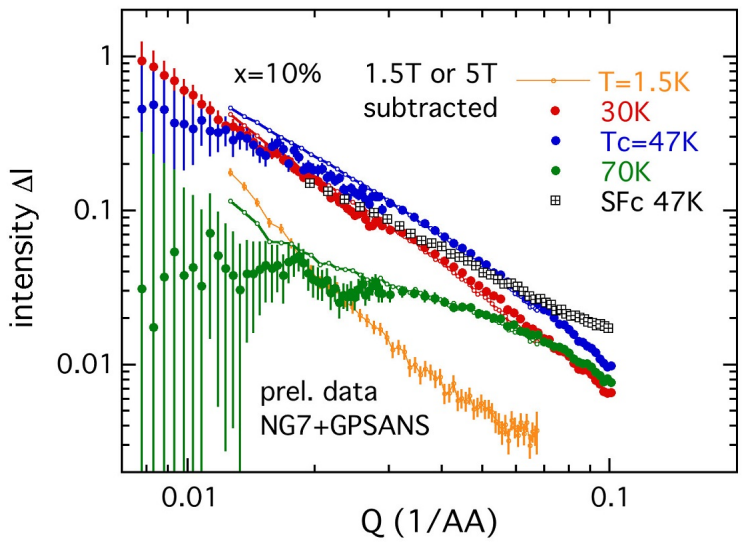

Figure 4.8: SANS intensity of $Ni_{1-x}V_x$ for $x = 10\%$ as a function of scattering vector Q measured at several temperatures. The high field data is subtracted as background. Data collected on GPSANS, ORNL (small circles) and on NG7 SANS, NIST (large circles).

A detailed magnetic cluster analysis is not possible yet. But, these initial measurements show that polarization analysis is feasible and can be extended towards lower Q and lower temperatures with better statistics. Further improvements to reduce the contribution of the sample holder are planned.

4.4 Discussion

In this chapter, I have presented evidence of fluctuating magnetic clusters in the d-metal alloy $Ni_{1-x}V_x$ on the ferromagnetic side of the quantum phase transition through a thorough μSR analysis of two FM samples. The non-universal power laws observed in the bulk magnetization data suggested a quantum Griffiths phase, that extended into the FM phase. But, the direct evidence of fluctuating magnetic clusters

was missing. μSR data could be modeled with simple fit-function in a wide concentration regime revealing an inhomogeneous FM ordered state. Analyzing the μSR data of two FM samples close to x_c revealed the coexistence of inhomogeneous magnetic order and magnetic clusters. These fluctuating magnetic clusters were identified by the PM contribution. While the asymmetry for $x = 10\%$ is well described by a static KT distribution function, a modification is needed such as nearly static GBG model to describe the field distribution at $x = 11\%$. For samples sufficiently close to the critical concentration x_c, the fluctuating clusters become more relevant consistent with the magnetization data. This provides the first convincing evidence for a quantum Griffiths phase on the FM ordered side of QPT. Resolving further details of the magnetic cluster distribution remains a challenge, but preliminary SANS measurements indicate that resolving magnetic intensities in the FM phase is feasible.

Chapter 5

Structural and magnetic study of CeRh-alloys

CePd and CePt are among the few ferromagnetic (FM) ordered Ce-alloys with a magnetic moment stemming from the localized f-electron in Ce^{3+}. The two binary alloys exhibit FM order close to $T_C \simeq 6$K [11, 27]. Chemical doping (replacing platinum (Pt) or palladium (Pd) by rhodium (Rh)) reduces T_C and leads finally to a nonmagnetic mixed valence state in CeRh [11, 48]. These compounds show indications of disordered quantum phase transitions but different scenarios were reported for the Pd- [11] and the Pt-systems [48].

To figure out the cause of these differences and the impact of disorder on the quantum phase transition in both f-electron compounds, I chose to study both systems ($CePd_{1-x}Rh_x$ and $CePt_{1-x}Rh_x$) at several Rh concentrations starting with a detailed structural investigation. The major part of this work involves the growth and characterization of several high quality polycrystalline samples at different Rh concentrations. Also magnetic ac-susceptibility measurements have been performed at a selected Rh concentration that are presented first before the major structure study. Major parts of this chapter are summarized in Ref. [70].

5.1 Magnetic ac-susceptibility

To check the quality of our samples and compare the magnetic property of the Pt- and the Pd-samples at low Rh concentration ($x = 0.2$), I performed ac- susceptibility measurements down to 4.2K in a He^4 cryostat (see Fig. 5.1). The FM transition is

clearly noticed by a steep upturn in $\chi(T)$ towards lower temperatures followed by a reduction within the FM state. The sharp maximum occurs at the same temperature ($T_C \simeq 6$K) for both compounds. The sharpness of the anomaly at the transition for both compounds shows that the substitution Pd/Rh or Pt/Rh does not affect the ferromagnetic transition at $x = 0.2$. Both samples, at low Rh concentration, show a similar response with almost the same transition temperatures that does not depend on the frequency (ν) of the applied field. The observed frequency dependence in the FM phase is not an indication of a spin glass or cluster glass phase since the actual transition temperature (T_C) does not change with ν. Here, we observe $\frac{\Delta T_C/T_C}{\Delta log\nu} < 0.005$. While for $x \geq 0.5$, $\frac{\Delta T_C/T_C}{\Delta log\nu} \geqslant 0.01$ was reported [48] as indication of a cluster glass transition.

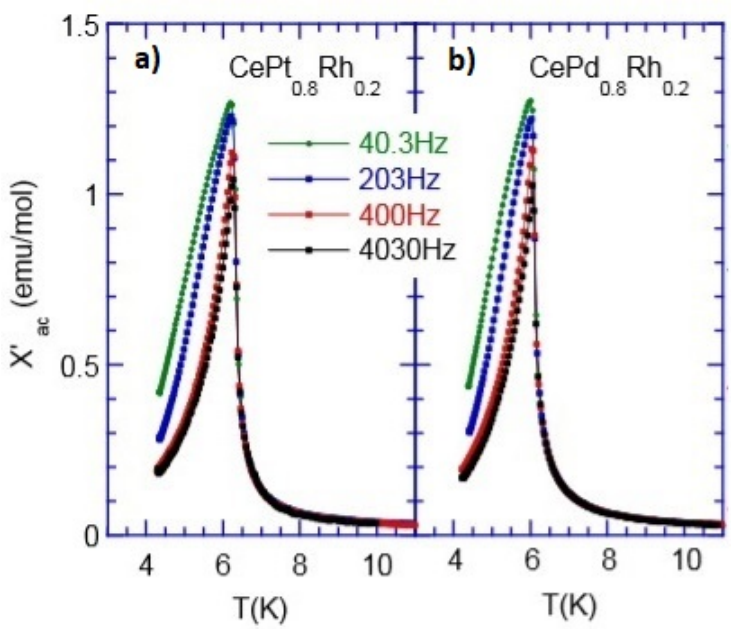

Figure 5.1: Low temperature magnetic ac-susceptibility of (a) $CePt_{0.8}Rh_{0.2}$ and (b) $CePd_{0.8}Rh_{0.2}$ for different frequencies of the driving field $B < 0.01$G.

The main structure characterization is revealed by a wide angle neutron diffraction experiment on NOMAD, at the SNS at 100K and 289K. In the following sections, I first check the main structure of our the samples by using EXPGUI analysis. The lattice constants and relevant parameters will be discussed and will be compared with other available published results. The pair distribution function (PDF) analysis allows a more detailed structural investigation since it is sensitive to short range correlations. Not only the local Ce-bond lengths can be traced as a function of composition in both compounds, but also the variance of bond lengths can be determined. In the next chapter, I investigate how to extract information about disorder and magnetic inhomogeneities from these structural studies using PDF analysis.

5.2 Structure analysis with EXPGUI

Rietveld analysis of the neutron powder diffraction data S(Q) using the EXPGUI program [59] shows that both systems, $CePd_{0.8}Rh_{0.2}$ (Pd-samples) and $CePt_{0.8}Rh_{0.2}$ (Pt-samples), crystallize in the orthorhombic CrB-type structure with space group Cmcm (#63) as expected. In this structure, the Ce atom is assigned to the "4c" crystallographic site $(0, y_{Ce}, 1/4)$ and the Rh and Pd/Pt atoms share the "4c" crystallographic site $(0, y_{Rh}, 1/4)$ with a given probability x according to the concentration of Rh [5].

The main orthorhombic CrB-type structure is shown in Fig. 5.2 in different planes. The blue spheres show the Ce-atoms and the red spheres show the Rh/Pt atoms in the Pt-samples or the Rh/Pd atoms in the Pd-samples on the shared site.

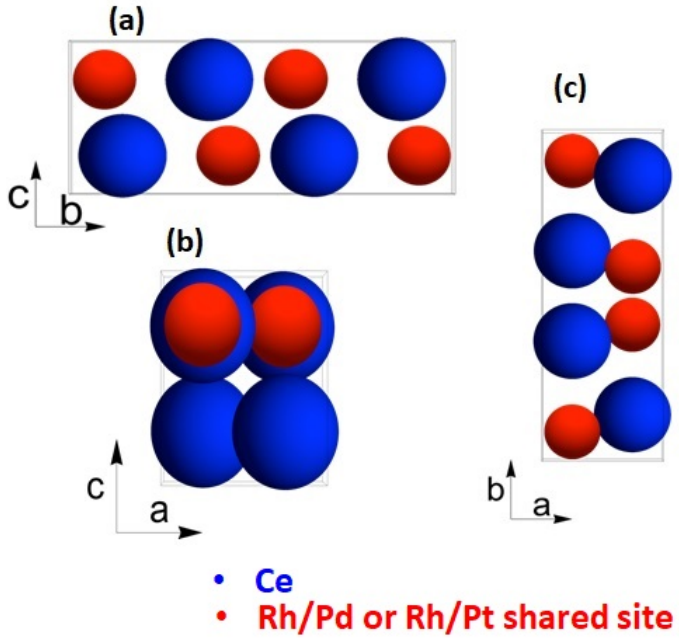

Figure 5.2: The CrB-type structure when viewed in different projections a) c-b plane b) c-a plane, and c) a-b plane. The blue spheres represent the Ce-atoms and the red spheres represent the Rh/Pt or Rh/Pd atoms on the shared sites.

Fig. 5.3 shows the structure function (S) plotted as a function of total time of flight (TOF) of both compounds at 100K for the lowest ($x = 0.2$) and the highest ($x = 0.8$) Rh concentrations. The difference between data (black symbol) and fit (red line) is shown by a green line at the bottom. The blue line underneath the peaks is the background fit function optimized for the lowest weighted profile R-factor (wRp) values. Additional peaks which do not belong to the CrB-structure have been noticed nearly for all concentrations in both compounds. Some of these additional peaks are indicated by blue arrows in Fig. 5.3.

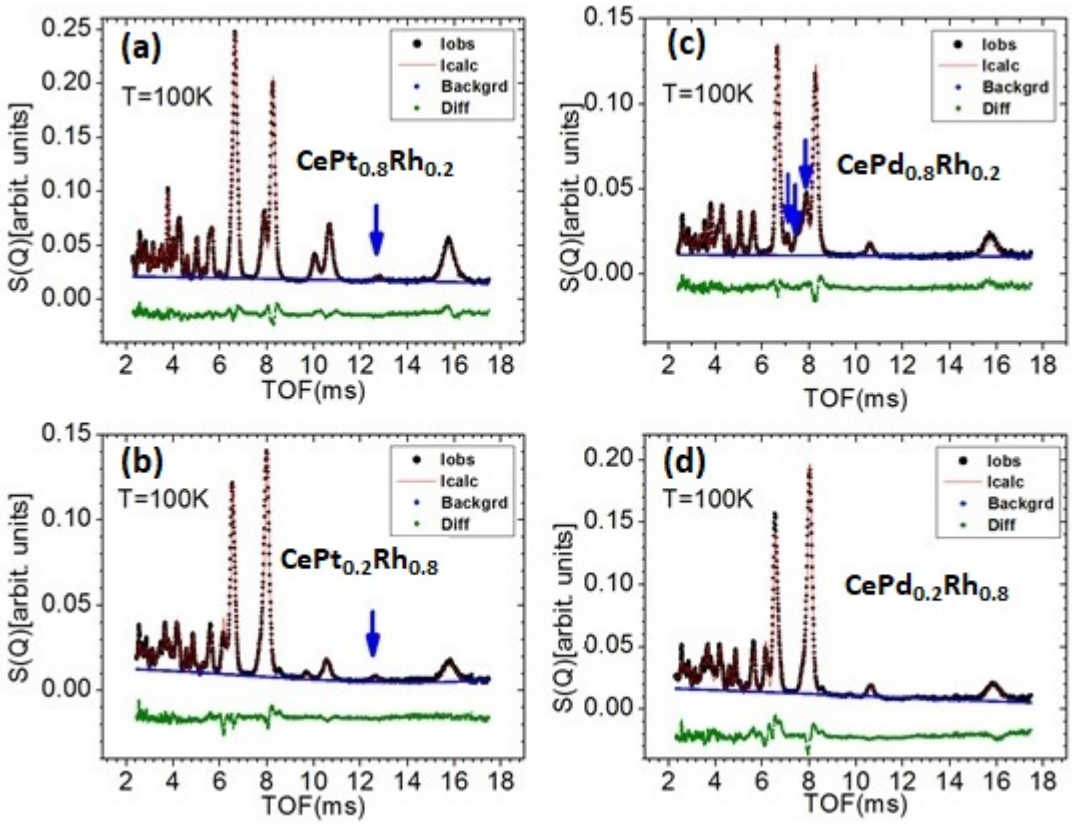

Figure 5.3: Structure function S of $CePd_{1-x}Rh_x$ and $CePt_{1-x}Rh_x$ for selected Rh concentrations, $x = 0.2$ and $x = 0.8$, at 100K as a function of total time of flight (TOF) reduced with EXPGUI. The black symbols show data and the red line represents the Rietveld fit. The difference between data and fit is shown by a green solid line at the bottom. Blue arrows show additional peaks from the identified minority phases of $Ce(Pt_{1-x}Rh_x)_2$ and Ce_3Pd_4.

Similar additional reflections were also observed in the X-ray powder diffraction pattern of CePt [71] but the origin was not explained. Gomez Sal et al. [6] suggested a distorted CrB-structure as secondary phase. In this work, we have successfully identified the additional structures for both the Pd- and the Pt-samples and details

of the structural parameters will be discussed in the subsequent sections.

To check the quality of our samples, we compare the lattice parameters of the main structure with other data. Table 5.1(a) presents our high temperature single-phase Rietveld analysis results of $CePd_{0.2}Rh_{0.8}$ with the results of $CePd_{0.15}Rh_{0.85}$ reported by Adroja et al. [5].

Table 5.1: Comparison of Rietveld analysis refined fit parameters of (a) single-phase $CePd_{0.15}Rh_{0.85}$ powder data obtained on GEM at 300K at ISIS reported by Adroja et. al [5] and our $CePd_{0.2}Rh_{0.8}$ powder data obtained on NOMAD at 289K at SNS and (b) CePt powder data obtained at 15K reported by Gomez Sal et. al [6] and our $CePt_{0.8}Rh_{0.2}$ powder data obtained on NOMAD at 100K at SNS.

(a)

$CePd_{1-x}Rh_x$		
x	0.85 [5]	0.80
T=300K		
$a(\AA)$	3.8801(8)	3.8902(9)
$b(\AA)$	10.9666(3)	10.9678(1)
$c(\AA)$	4.2381(1)	4.2696(1)
y_{Ce}	0.1376(1)	0.1368(4)
y_{Rh}	0.4091(1)	0.4118(4)
$u_{Ce}(\AA^2)$	0.0075(2)	0.0054(6)
$u_{Rh}(\AA^2)$	0.0176(3)	0.01727(8)
wRp(%)	4.8	7.33

(b)

$CePt_{1-x}Rh_x$		
x	0 [6]	0.20
T	15K	100K
$a(\AA)$	3.884(2)	3.903(6)
$b(\AA)$	10.845(5)	10.880(7)
$c(\AA)$	4.517(3)	4.484(7)
y_{Ce}	0.1362(10)	0.1387(6)
y_{Rh}	0.4128(7)	0.4130(5)
$u_{Ce}(\AA^2)$	—	0.008(6)
$u_{Rh}(\AA^2)$	—	0.009(1)
wRp(%)	—	5.97

Similarly, Table 5.1(b) compares $CePt_{0.8}Rh_{0.2}$ data at 100K (the lowest Rhodium concentration we have) with the refined lattice parameters obtained from CePt powder data at 15K from Ref. [6]. Although the Rh concentrations, the experimental settings, and the analysis methods are slightly different, it confirms that our samples compare well with other samples presenting similar and reproducible parameters. In Table 5.1(a), the slight increase in the lattice parameters of our Pd-sample is expected since the Rh concentration in our sample is reduced by $\sim 5\%$. Nevertheless, the lattice parameters of our Pt-sample in Table 5.1(b) are slightly bigger although the Rh concentration is higher by a significant amount $\sim 20\%$. This could be attributed to the fact that our measurement was taken at a higher temperature.

5.3 Structure of minority phases $Ce(Pt_{1-x}Rh_x)_2$ and Ce_3Pd_4

Both systems Ce-Pd and Ce-Pt can form a Ce_3T_4 phase (with T= Pd or Pt), but only Ce-Pt and also Ce-Rh can crystallize in a CeT_2 phase (with T= Pt or Rh). Focusing on these crystal structures of the neighbor phases in the phase diagram of Ce-Pt [71], Ce-Pd [72] and Ce-Rh [73] lead to a successful identification of the extra peaks. In $CePd_{1-x}Rh_x$, the best second phase is Ce_3Pd_4 for $x \leq 0.6$, in $CePt_{1-x}Rh_x$ the best second phase is $Ce(Pt_{1-x}Rh_x)_2$, that improves the fit of the data. The $Ce(Pt_{1-x}Rh_x)_2$ structure identified by EXPGUI in the Pt-samples is isostructural to the Cu_2Mg-type structure with space group $Fd\bar{3}m$ shown in Fig. 5.4(a). The blue spheres represent the Ce-atoms assigned to the "8b" and the red spheres show the Rh/Pt atoms assigned to the "16c" site that is shared with the probability of occupation given by the Rh concentration.

The structure of $CePt_2$ ($x = 0$) was initially identified by Zachariasen et al. [74] with a lattice constant $a = 7.714\mathring{A}$ and later confirmed by A. Janghorban et al. [71] based

on X-ray diffraction with a resulting lattice constant, $a = 7.741(4)\AA$. Our analysis with $0.2 \leqslant x \leqslant 0.8$ yield lattice constants that are smaller than $CePt_2$ but larger than CeR_2 ($a = 7.545\AA$) [73] consistent with the Rh concentration.

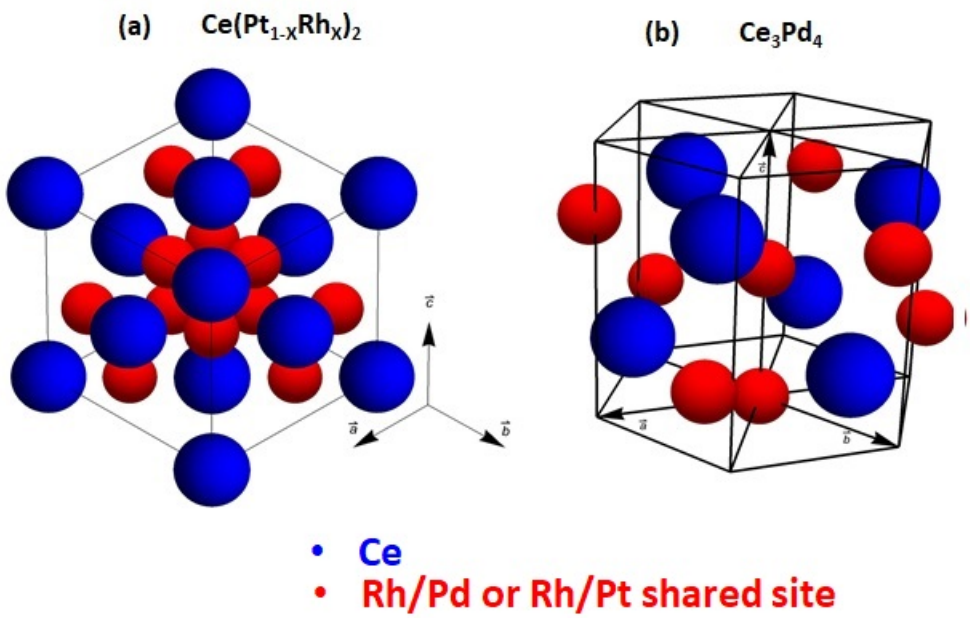

Figure 5.4: Structures of the minority phase (a) $Ce(Pt_{1-x}Rh_x)_2$ and (b) Ce_3Pd_4. Blue spheres show the Ce-atoms and the red spheres show (a) the Pt/Rh atoms and (b) the Pd/Rh atoms.

The Ce_3Pd_4 structure is identified in the Pd-samples. This phase is isostructural to the Pu_3Pd_4-type structure with space group $R\bar{3}$ as shown in Fig. 5.4(b). The blue spheres represent the Ce-atoms assigned to the "18f" site and the red spheres show the Pd-atoms assigned to "18f", "3a", and "3b" sites in the rhombohedral notation. See specific values and detailed information about the second phase fit parameters in the Appendix.

5.4 PDF analysis of $CePt_{1-x}Rh_x$ using PDFgui

To study the local structure of our samples, we focus mainly on the PDF analysis modeling the extracted PDF data using PDFgui [75]. As we discussed in Chapter 2, $G(r)$ allows us to study the local structure on different length scales by varying the maximum range value (r_{max}). The extra phases identified from our EXPGUI analysis are tested and verified by the results of our PDF analysis.

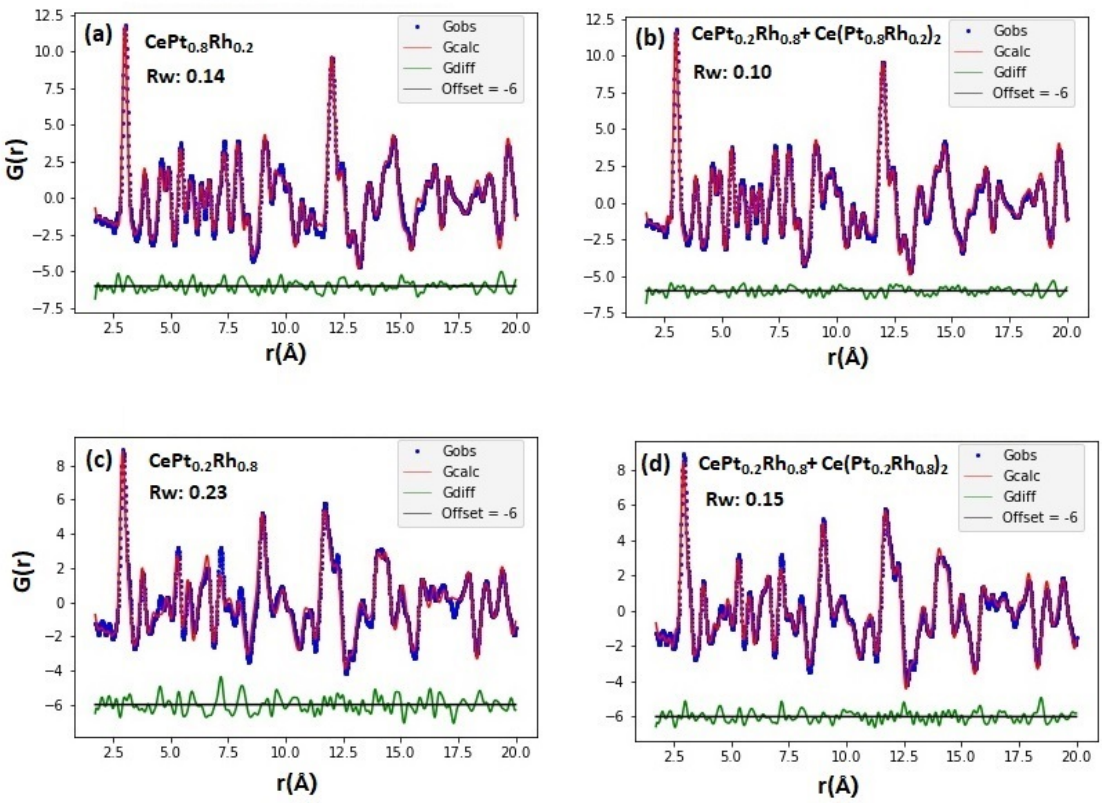

Figure 5.5: PDF of powder data of selected Pt-alloys at 100K on NOMAD with (a) single-phase fit & (b) two-phase fit for $CePt_{0.8}Rh_{0.2}$ and (c) single-phase fit & (d) two- phase fit for $CePt_{0.2}Rh_{0.8}$. The difference, Δ = data(blue symbols)-fit(red line), is shown by a wavy green line beneath the peaks with a black straight line showing the offset by 6 units.

Already, the single-phase fit modeling a CrB-structure describes the PDF data well. But, the introduction of a second phase as identified by EXPGUI significantly improves the weighted residual factor (Rw) for both the Pd- and the Pt-compounds for all concentration of Rh. Fig. 5.5(a) shows the reduced G(r) data at 100K and a single-phase fit of CrB-type structure for $CePt_{0.8}Rh_{0.2}$ within a fit range of $1.75\mathring{A} \leq r \leq 20\mathring{A}$. The instrumental parameters $Q_{damp} \simeq 0.018\mathring{A}^{-1}$ and $Q_{broad} \simeq 0.02\mathring{A}^{-1}$ are used throughout our analysis and more details about the instrumental parameters are available in the Appendix. The difference between data and fit results in a weighted residual factor (Rw) of ~ 0.14 with a single-phase fit. Fig. 5.5(b) demonstrates that the fit quality is improved and that Rw is reduced to ~ 0.10 by introducing a second phase $Ce(Pt_{1-x}Rh_x)_2$ with a small phase fraction $\sim 5\%$. A single-phase fit with Rw ~ 0.23 and a two-phase fit with a reduced Rw ~ 0.15 for $CePt_{0.2}Rh_{0.8}$ are presented in Figs. 5.5(c) and (d), respectively. We see that although the Rw value is improved by the introduction of a second phase, its value still remains significantly high at higher Rh concentration.

In Figs. 5.6(a) and (b), the red symbols indicate the Rw values based on the main phase fit with P_1 only, the blue symbols represent the reduced Rw values by introducing additional second phase (P_1+P_2). The green symbols show the Rw of the two-phase model introducing an additional parameter "spd" to model the effect of the finite nanoparticle size with a spherical shape factor. Only a slight reduction of Rw is noticed. Our results suggest that a finite nanoparticle size effect is negligible and does not need to be considered further in our analysis. The open symbols in Fig. 5.6(b) denote Rw for a two-phase model with a different second phase P_2. Rw for $x = 0.8$ is reduced if P_2 is $CeRh_2$, which is the same second phase the Rh-rich

Pt-samples. Figs. 5.6(c) and (d) display the fraction of the second phase (f_2) in the Pt- and Pd-compounds for all concentrations, respectively. The fraction of the second phase is defined as ($f_2 = \frac{s_2}{s_1+s_2}$), where s_1 and s_2 are the amplitude parameter "scales" for the main phase and the secondary phase in the PDFgui program, respectively.

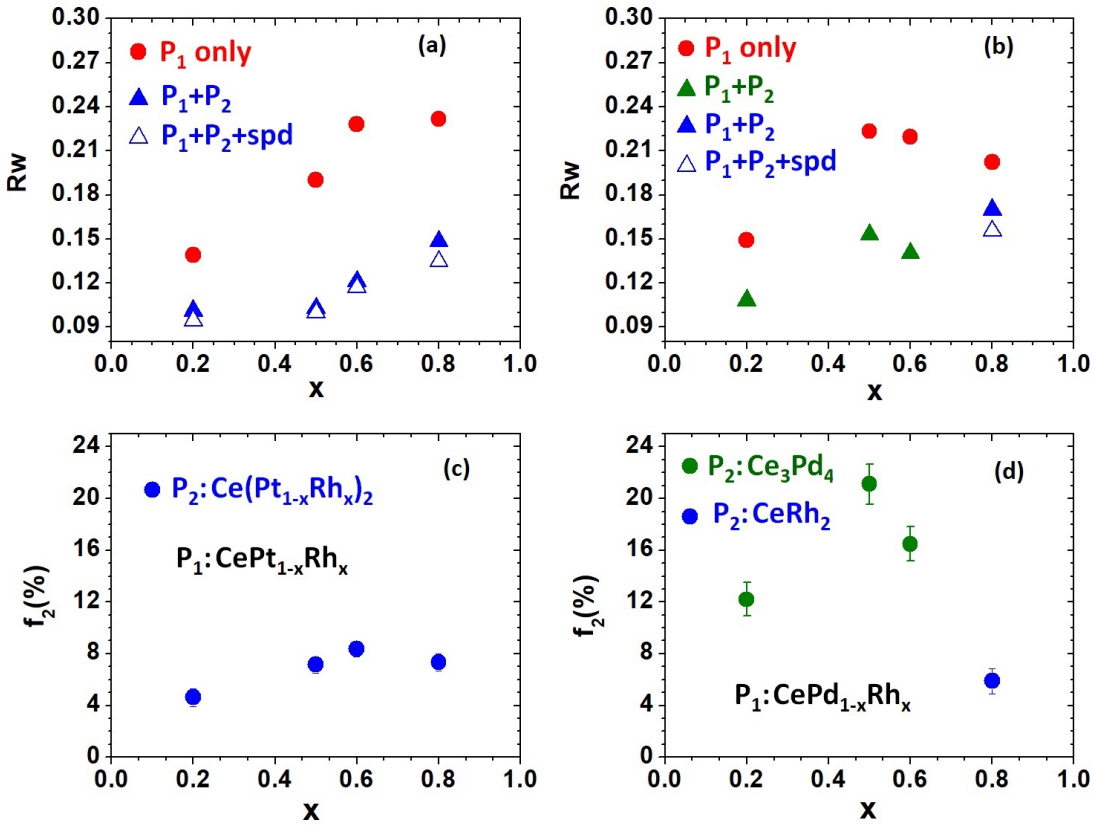

Figure 5.6: The weighted residual factor (Rw) from PDF analysis of (a) $CePt_{1-x}Rh_x$ and (b) $CePd_{1-x}Rh_x$ in fit range $1.75\AA \leq r \leq 20\AA$ at 100K. The red symbols show single-phase fit with P_1 only, blue symbols show two-phase fit with P_1+P_2, where P_2 is $CeRh_2$-type phase, and green symbols show two-phase fit with P_2=Ce_3Pd_4. Open symbols include additional parameter spd. The fraction of the second phase (f_2) in (c) $CePt_{1-x}Rh_x$ and (d) $CePd_{1-x}Rh_x$ as a function of Rh concentration x.

Fig. 5.6 gives an overview of the fit quality Rw of the PDF analysis using a single-phase or two-phase description as a function of Rh concentration x. Rw is reduced for all samples introducing a second phase. From our results, we see that the reduced G(r) data are well described with two phases with low weighted residual factors, Rw< 0.2. For $x = 0.2$, the best Rw value is reduced to ~ 0.10, indicating a good description. Rw is limited here as a result of the short Q_{max} cutoff due to Rh absorption. But, at the highest Rh concentration ($x = 0.8$), Rw remains higher ($\simeq 0.15$) even for the best two-phase fit indicating structural disorder. Before addressing the disorder in these compounds, the next chapter reports the extracted lattice parameters of the Pt- and Pd-alloy, respectively. The PDF analysis does not differ from the EXPGUI analysis. Also the parameters of the second phase are consistent and agree with published results [76]. More details are discussed in the next Chapters.

5.5 The lattice parameters of $CePt_{1-x}Rh_x$

The lattice parameters of the unit cell and the specific atomic positions in the main phase of $CePt_{1-x}Rh_x$ were determined consistently with PDFgui and EXPGUI. Fig. 5.7 and Fig. 5.8 illustrate the systematic variation of the lattice parameters of the main orthorhombic CrB-type structural phase of $CePt_{1-x}Rh_x$ with x at temperatures 100K and 289K. The lattice constant a slightly decreases and b does not change significantly towards the higher concentration (see Figs. 5.7(a) and (b)).

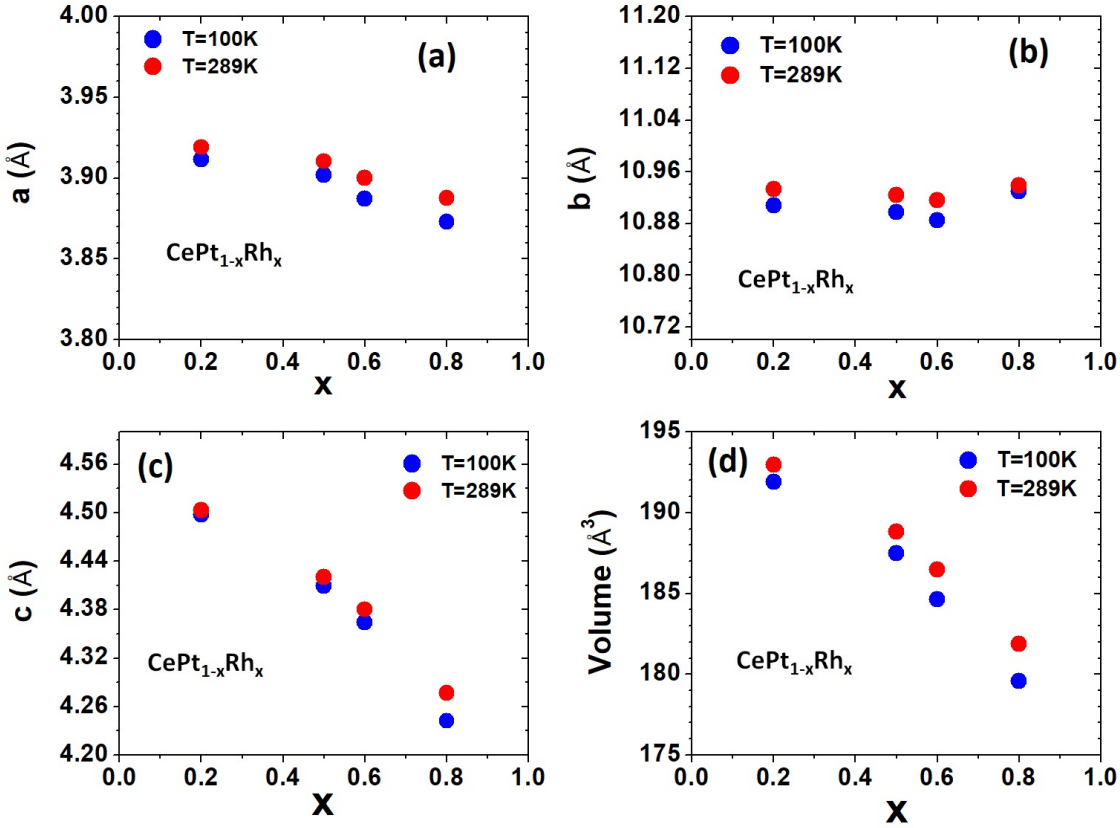

Figure 5.7: Refined lattice parameters of $CePt_{1-x}Rh_x$ vs x at $T = 100$K (blue circles) and $T = 259$K (red circles) are shown. (a), (b), and (c) show the lattice constants a, b, and c, respectively. (d) presents the unit cell volume, V.

However, the lattice constant c and, therefore, the unit cell volume decreases significantly as the Rh concentration increases (see Figs. 5.7(c) and (d)).

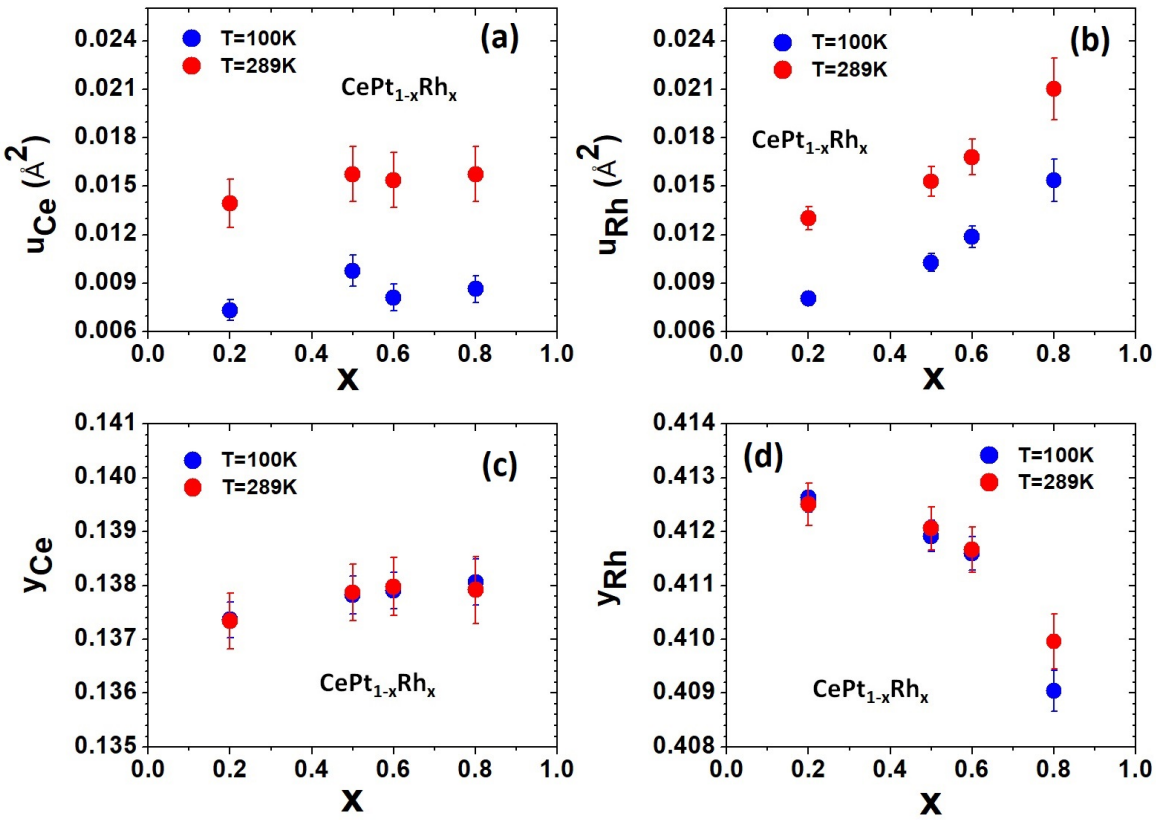

Figure 5.8: Refined parameters of $CePt_{1-x}Rh_x$ vs x at different temperatures, T = 100K (blue circles) and T= 259K (red circles): (a) and (b) show isotropic ADP of Ce, u_{Ce}, and of Rh/Pt site, u_{Rh}, respectively. (c) and (d) present the atomic position of Ce, y_{Ce}, and of the Rh/Pt site, y_{Rh}, respectively.

We note that the lattice constant c at 100K decreases with a rate ($\Delta c/c\Delta x$) of $\sim 12.5\%$ as the Rh concentration increases (as estimated from $x = 0.2 - 0.8$) which is significantly higher than the difference between the covalent radii of Rh and Pt ($\sim 3\%$) [37]. This indicates that the decrease in the lattice parameter c and hence the unit cell volume cannot be explained by considering only the difference between the

covalent radii of Rh and Pt. As expected, all the lattice constants increase with higher temperature. Figs. 5.8(a) and (b) show the isotropic atomic displacement parameters (ADP) of the Ce atom (u_{Ce}) and the Rh atom u_{Rh}, respectively. We see that both, u_{Ce} and u_{Rh}, increase with temperature as the dynamic atomic displacement parameter dominates at high temperature. On the other hand, u_{Rh} increases significantly with concentration unlike u_{Ce} which does not increase much with Rh concentration. It is worth noting that we considered the isotropic atomic displacement parameter ($\langle u_{iso}^2 \rangle$) only to limit the number of free parameters and avoid correlations. Although the "isotropic" u_{Ce} does not appear to change much, our preliminary results show that "anisotropic" u_{Ce} fit parameters change in specific directions employing single-phase model (not included here). As depicted in Figs. 5.8(c) and (d), the positions of the Ce atoms (y_{Ce}) and the Rh atoms (y_{Rh}) do not change notably with temperature and only y_{Rh} slightly decreases towards higher Rh concentration (with a slope $\Delta y/y\Delta x < 1\%$).

5.6 PDF analysis of $CePd_{1-x}Rh_x$ using PDFgui

Fig. 5.9(a) demonstrates the reduced G(r) data at 100K and a single-phase fit of CrB-type structure for $CePd_{1-x}Rh_x$ within a fit range $1.75\mathring{A} \leq r \leq 20\mathring{A}$. The difference between data and fit results in a weighted residual factor (Rw) ~ 0.15 with a single-phase fit. Fig. 5.9(b) shows the reduced Rw $\sim$ 0.11 by introducing a second phase Ce_3Pd_4 with a small phase fraction $< 20\%$ (see for example Fig. 5.6d). Fig. 5.9(c) shows a single-phase fit for $CePd_{0.2}Rh_{0.8}$ resulting in Rw $\sim$ 0.20 and Fig. 5.9(d) shows the improvement of the fit quality (Rw$\sim$ 0.17) by introducing an extra $CeRh_2$ phase in a small fraction $\sim 6\%$ (see Fig. 5.6(d)).

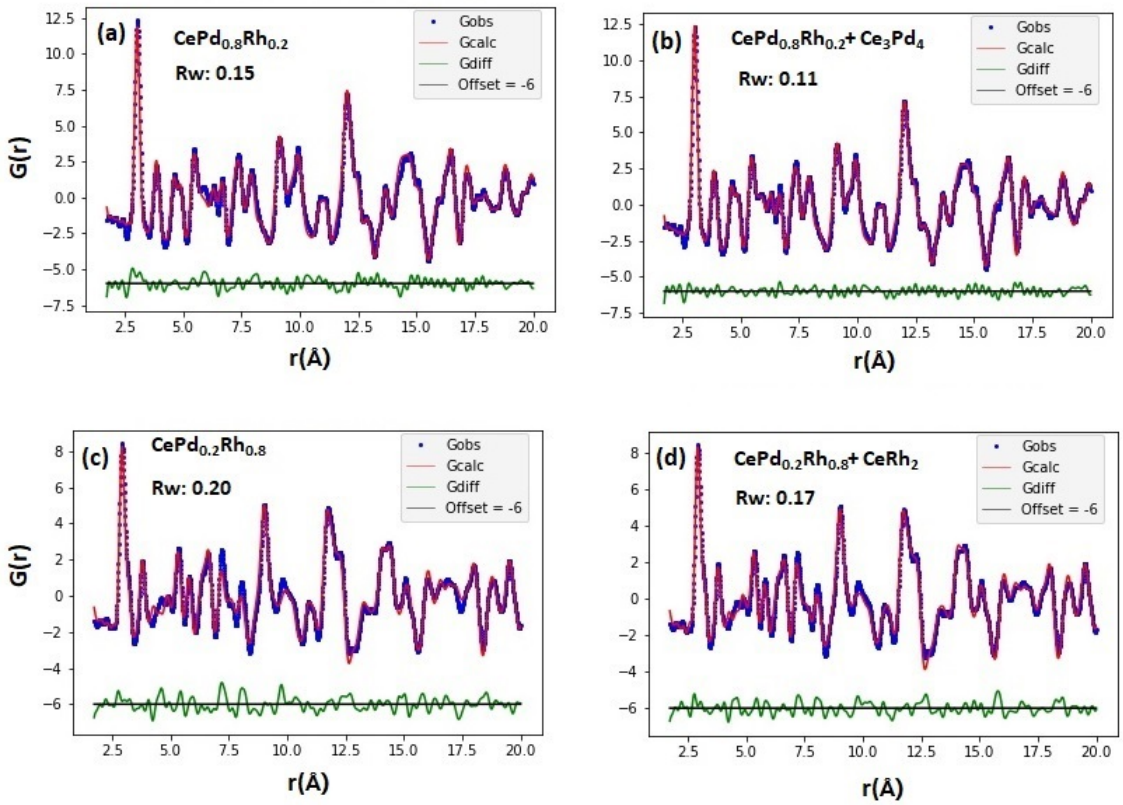

Figure 5.9: PDF of $CePd_{1-x}Rh_x$ at 100K with (a) single-phase fit & (b) two-phase fit of $CePd_{0.8}Rh_{0.2}$ and (c) single-phase fit & (d) two-phase fit of $CePd_{0.2}Rh_{0.8}$. The difference, Δ = data(blue symbols)-fit(red line), is shown by a wavy green line beneath the peaks with a black straight line showing the offset by 6 units.

The lattice parameters of the main phase are within error bars as compared to the results of a single-phase fit. Also the parameters of the second phase are consistent with published results [72]. Details of the structure parameters of the second phase will be given in the Appendix.

5.7 The lattice parameters of $CePd_{1-x}Rh_x$

Fig. 5.10 and Fig. 5.11 show the systematic variation of the lattice parameters of the main orthorhombic CrB-type structural phase of $CePd_{1-x}Rh_x$ with the Rh concentration at temperatures 100K and 289K. The lattice constant a of the Pd-samples does not change much with the concentration x. However, the lattice constant b slightly increases towards higher concentration ($< 1.5\%$).

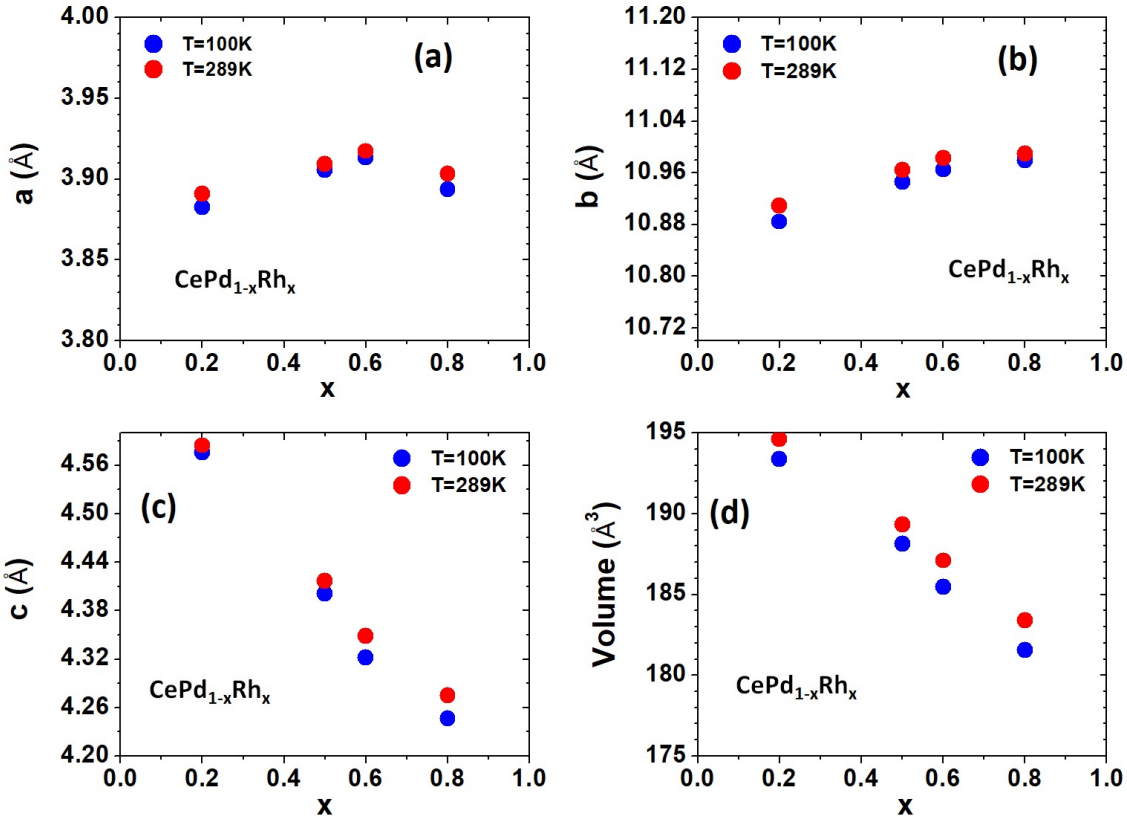

Figure 5.10: Refined lattice parameters of $CePd_{1-x}Rh_x$ vs x at $T = 100$K (blue circles) and $T = 259$K (red circles). (a), (b), and (c) show the lattice parameters a, b, and c, respectively. (d) presents the unit cell volume, V

The lattice constant c and, therefore, the unit cell volume of the Pd-samples decreases significantly as the Rh concentration increases. The lattice constant c at 100K decreases at a rate ($\Delta c/c\Delta x \sim 13\%$) as the Rh concentration increases which is significantly higher than the difference between the covalent radii of Rh and Pd ($\sim 2\%$) [37].

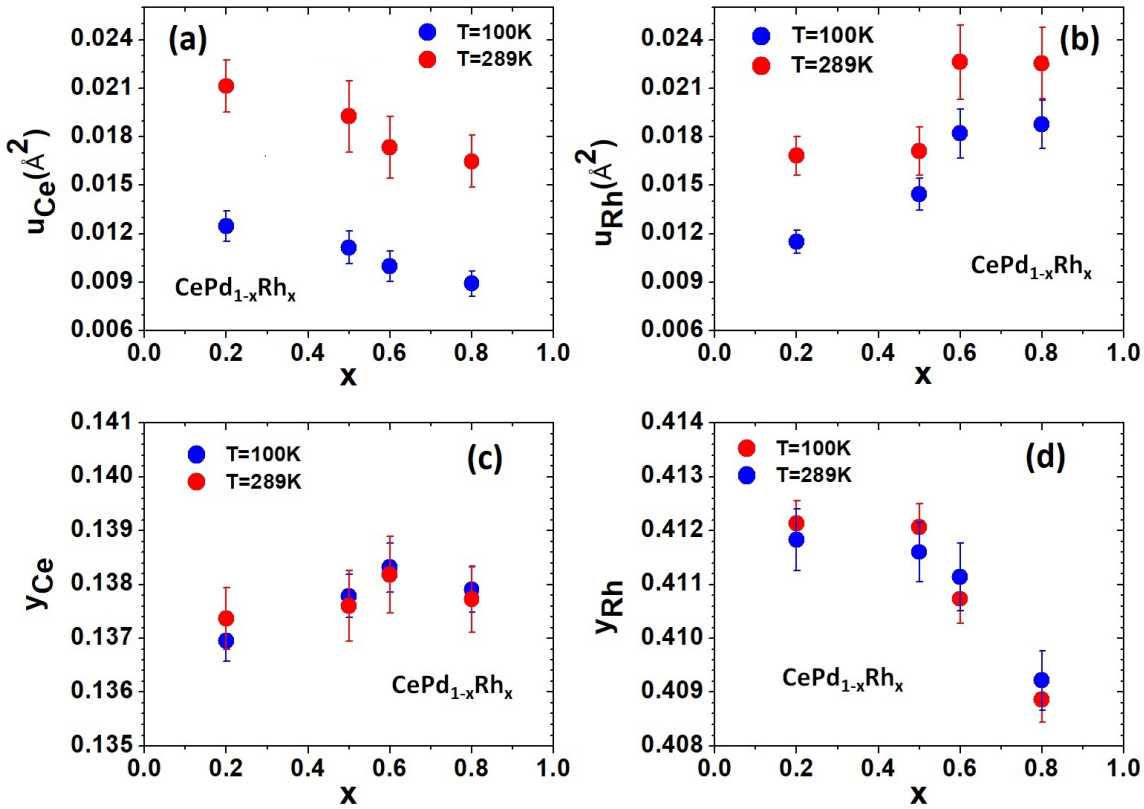

Figure 5.11: Refined parameters of $CePd_{1-x}Rh_x$ vs x at different temperatures, $T =$ 100K (blue circles) and $T =$ 289K (red circles). (a) and (b) show isotropic ADP of Ce, u_{Ce}, and of Rh/Pd site, u_{Rh}, respectively. (c) and (d) present the atomic position of Ce, y_{Ce}, and of the Rh/Pd site, y_{Rh}, respectively.

All the lattice constants except the atomic positions increase with temperature. Figs. 5.11(a) and (b) show the isotropic atomic displacement parameters (ADP) of the Ce atoms ($u_{Ce} =< u_{iso}^2 >$) and the Rh/Pd shared sites u_{Rh} of the Pd-samples, respectively. We see that both u_{Ce} and u_{Rh} increase with temperature as the dynamic ADP dominates at higher temperature. The isotropic ADP of the shared Rh/Pd site, u_{Rh}, increases significantly with Rh concentration unlike the isotropic ADP of the Ce atom u_{Ce} which does not change much with Rh concentration. Figs. 5.11(c) and (d) show that the positions of the Ce atoms (y_{Ce}) and the Rh/Pd atoms (y_{Rh}) do not change notably with temperature and only y_{Rh} slightly decreases towards higher Rh concentration (with a slope $\Delta y/y\Delta x \sim 1\%$).

5.8 Discussion

In this chapter, we have confirmed that all our samples crystallize in the orthorhombic CrB-type structure and that both samples with $x = 0.2$ show a FM phase transition at $T_C \sim 6$K. A small fraction of additional phases have been identified. The Pd- and the Pt-samples, in general, look similar. They display similar structural parameters of the main phase. The secondary phases are different for the Pd-samples (Ce_3Pd_4) and for the Pt-samples ($Ce(Pt_{1-x}Rh_x)_2$). The lattice constants a and b of the main phase as well as the atomic positions do not change much with concentration x for both compounds. Whereas, the lattice constant c and hence the unit cell volume decreases significantly towards higher concentration. The lattice constant c decreases at a rate of $\Delta c/c\Delta x \sim 13\%$ for the Pd-samples and at $\Delta c/c\Delta x \sim 12.5\%$ for the Pt-samples. This rate of change cannot be explained by Vegard's law,

$$c = c_0(1 - x\frac{\Delta r}{r}), \tag{5.1}$$

where $\frac{\Delta r}{r} \simeq 0.02$ (0.03) is the relative covalent radius difference between Pd (Pt) and Rh atoms, respectively. Moreover, it is shown that while the isotropic ADP of the Ce atom (u_{Ce}) does not change notably with concentration, the isotropic ADP of the shared Rh/Pd or Rh/Pt site (u_{Rh}) increases significantly towards higher x. With random occupation of two neighboring atoms with different sizes, we expect the variance of the bond length to show a maximum at $x = 0.5$.

In the next chapter, we will have a close look at the local Ce-environment by determining the different bond lengths and their variation with Rh concentration to explain these observed anomalies and to get to the origin of disorder in these systems.

Chapter 6

Origin of disorder in ferromagnetic CeRh-alloys

In the previous chapter, we have checked the structural quality of our samples and the variation of important parameters such as the lattice constants, the atomic positions, and the atomic displacement parameters with temperature and Rh concentration in both compounds. We have seen that the decrease of the lattice constant c with concentration could not be explained just by the introduction of a smaller Rh atom. In addition, the fact that the isotropic ADP of the shared Rh/Pd or Rh/Pt site increases beyond $x = 0.5$ requires a close look at specific bonds between different pairs of atoms. In this chapter, we will present the bond lengths between different pairs of atoms and their variance to probe the local Ce-environment and investigate the main causes for the magnetic inhomogeneities in our systems.

6.1 Investigation of the local Ce-environment

Using PDFgui, we have determined the bond lengths between different pairs of atoms from our PDF data taken at 100K for both the Pd- and the Pt-samples. In particular, we are interested in the local Ce-environment and investigate the evolution of the Ce-Rh and the Rh-Rh bond lengths with concentration in both the Pd- and the Pt-compounds. "Rh" indicates the Rh-site, that is actually filled with Pd/Pt or Rh atom depending on x. Figs. 6.1(a) & (b) present the evolution of specific bond lengths with concentration x. We see that Ce has seven nearest Rh neighbors with three different Ce-Rh bond lengths $L \sim 3\mathring{A}$. Also, the closest Rh-Rh bond length

$\sim 3\AA$ contributes to the first peak in $G(r)$.

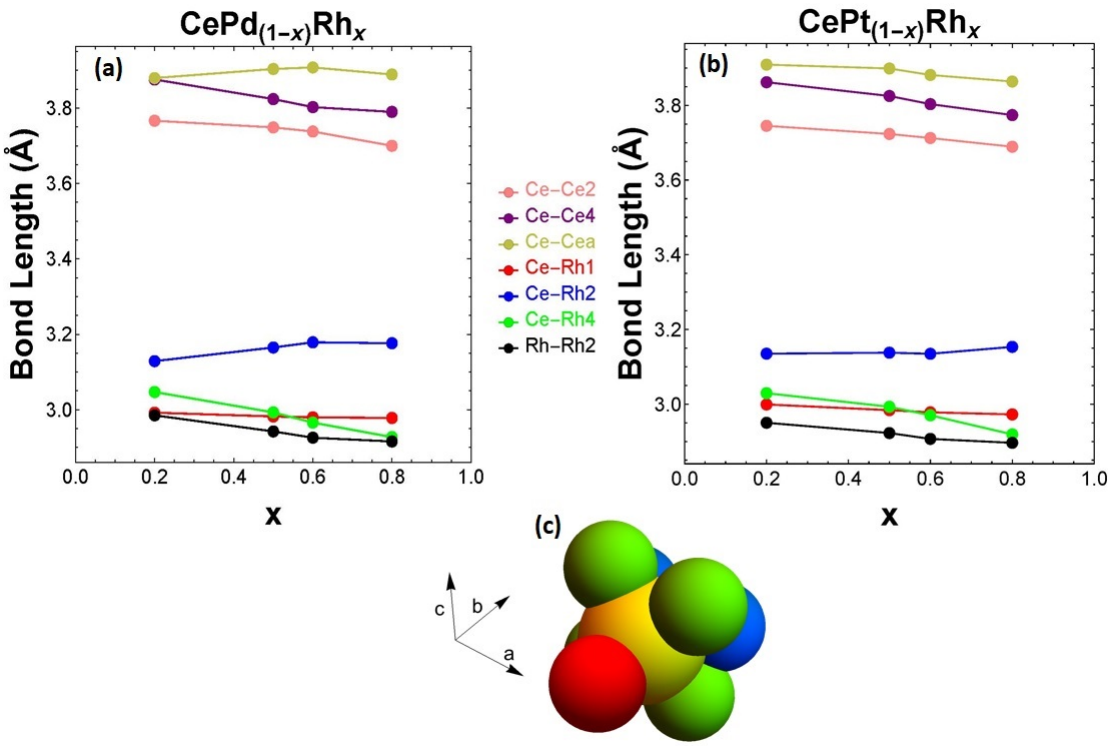

Figure 6.1: Variation of bond lengths between different pairs of atoms at 100K in (a) $CePd_{1-x}Rh_x$ and (b) $CePt_{1-x}Rh_x$. (c) displays the Ce-atom (yellow) and its seven nearest neighbors at different distances (different colors).

As can be seen in Figs. 6.1(a) & (b), the Rh-Rh bond length (black symbols) slightly decreases with concentration in both the Pd-samples and the Pt-samples with a relative slope $\Delta L/L\Delta x \sim 3-4\%$. The Ce-Rh4 bond length (green symbols), the distance between Ce and four Rh nearest neighbors, decreases strongly by $\sim 7\%$ for the Pd-samples and by $\sim 6.5\%$ for the Pt-samples. However, the Ce-Rh2 bond length, the distance between Ce and two Rh nearest neighbors (blue symbols), increases and creates a spread of bond lengths at higher concentrations. This is mainly the reason for the extra shoulder observed for $x = 0.8$ in the first peak of the PDF data (see

Figs. 5.5(c) & (d) and 5.9(c) & (d). We note here that the weak reduction of the Rh-Rh bond length and the larger reduction of the Ce-Rh4 bond length are the main reason for the strong reduction of the lattice constant c. The strong increase of the isotropic atomic displacement parameter u_{iso} with x can be explained by considering relevant bond lengths. As the bond length of a close atom pair is found through the peak position in $G(r)$, the bond length variance σ_{ij}^2 determines the peak width (besides instrumental contribution). The thermal motion and static displacement of both individual atoms contribute to the mean square relative displacement of atom pairs [77]

$$\sigma_{ij}^2 = u_i^2 + u_j^2 + corr \tag{6.1}$$

that are bond length variances for close neighbors. Using only isotropic ADP u_{iso} for each element and neglecting terms that are not simply x-dependent, such as the correlation term and u_{Ce}, we see that changes in ADP can be related to changes in bond lengths variance ($\Delta u_{Rh}^2 \sim \Delta\sigma_{Ce-Rh}^2$ and $\Delta u_{Rh}^2 \sim \frac{1}{2}\Delta\sigma_{Rh-Rh}^2$).

To get $\Delta\sigma_{ij}^2$ from the radius difference between Rh and Pd/Pt is straight forward. Assuming the smaller atom Rh has radius r and probability of occupation x with the larger atom, Pd/Pt, has radius R and probability of site occupation $1-x$, the average bond length is given by

$$\bar{d} = 2[(1-x)R + (x)r]. \tag{6.2}$$

The corresponding variance is

$$\sigma_{Rh-Rh}^2 = \bar{d^2} - (\bar{d})^2 = 2(R-r)^2 x(1-x). \tag{6.3}$$

On the other hand, evaluating the variance of the Ce-Rh bond lengths is more complicated. Locally, Ce can have a maximum of seven Rh nearest neighbors with similar

distances with a probability of occupation x each, and hence the probability is x^7 of finding all the seven Rh nearest neighbors. We know that the bond length in CeRh is very short (d). In the simplest model, we assign one long bond length (D) for all Ce-Rh bonds, if Ce has at least one Pd/Pt neighbor. For example, for a Rh concentration $x = 0.8$, about 21% of the Ce-atoms have seven Rh neighbors with short bond length (d), while $\sim 79\%$ of the Ce-atoms should have at least one Pd/Pt nearest neighbor with larger bond length (D). This mixture of two bond lengths creates a variance of

$$\sigma^2_{Ce-Rh} = (D-d)^2 x^7 (1-x^7). \tag{6.4}$$

The maximum value of $\sigma^2(x)$ is found at higher concentration, $x \sim 0.9$ than $x = 0.5$. If correlated motion is neglected, u_{iso} from each element contributes to the variance of bond lengths (see for example Eq. 2.7). Considering the contributions from atomic size differences, the variance of Ce-Rh bond lengths, and crystal defects, the fit function for the isotropic atomic displacement parameter u_{Rh} of the shared Rh/Pd or Rh/Pt-site can be written as

$$u_{Rh} = u_0 + u_1 x(1-x) + u_2 x^7 (1-x^7). \tag{6.5}$$

u_0, u_1, and u_2 are fit parameters proportional to the concentration independent crystal defect and thermal motion contributions, the square of the radius difference between Rh/Pd or Rh/Pt atoms, and the square of the difference between the shorter and the larger bond lengths, respectively as extracted from data. The expected values of these parameters are approximately $u_1 = \frac{d_0^2}{2}(\frac{R-r}{r})^2 \simeq 0.004\mathring{A}^2$ and $u_2 = d^2(\frac{D-d}{d})^2 \simeq 0.04\mathring{A}^2$. Using the experimental data, $d_0 \simeq 2.9\mathring{A}$ for the Rh-Rh bond length, $\frac{R-r}{r} = 0.03$ for the radius difference between Pt and Rh, $d = 3\mathring{A}$ for the Ce-Rh bond length, and $\frac{D-d}{d} = 0.065$ for the Ce-Rh bond length change.

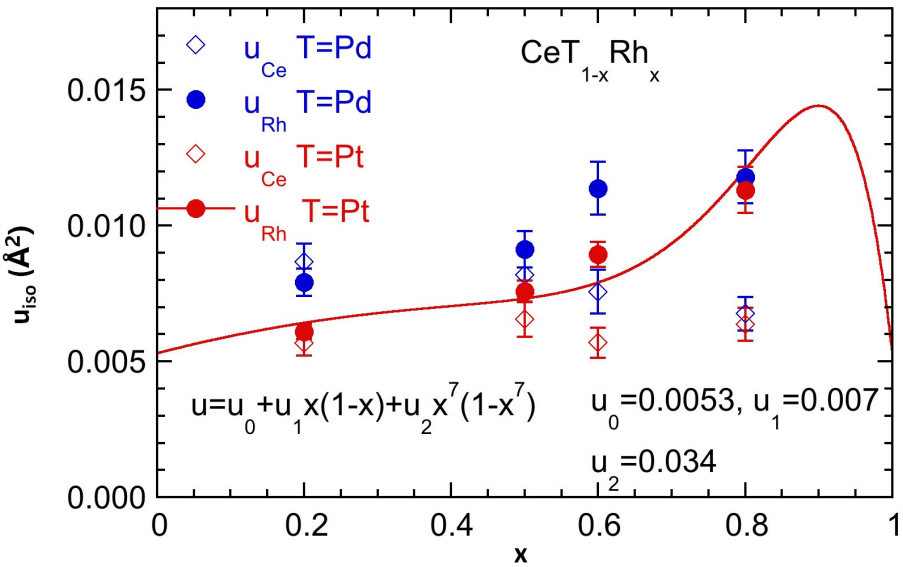

Figure 6.2: Isotropic ADP, u_{Rh} and u_{Ce} at 100K of $CePd_{1-x}Rh_x$ and $CePt_{1-x}Rh_x$ vs x, red line shows fit of $u_{Rh}(x)$ of Pt-samples.

Fig. 6.2 illustrates the evolution of the isotropic atomic displacement parameters (u_{iso}) with Rh concentration x for both $CePd_{1-x}Rh_x$ and $CePt_{1-x}Rh_x$ compounds. The corresponding fit function (red line) for $u_{Rh}(x)$ is included assuming seven Rh nearest neighbors are relevant for the shorter bond length. Eq. 6.5 suggests that the maximum isotropic ADP should occur at a higher concentration ($x \sim 0.9$) consistent with the results we obtained from our PDFgui analysis. The fit parameters u_1 and u_2 are also consistent with the expected values (within error bars). This confirms that this simple model with just two different bond lengths explains the increase of u_{Rh} beyond $x = 0.5$.

To investigate the local Ce-environment very closely, Figs. 6.3(a) and (b) compare three different models for the PDF data of the Pt- and the Pd- samples at the maximum Rh concentration ($x = 0.8$) at 100K within a very short fit range

$2\mathring{A} \leqslant r \leqslant 5.6\mathring{A}$, respectively. In both Figs. 6.3(a) and (b), the blue symbols represent the observed PDF data at 100K and the red line indicates the model with two different Ce-environments P_1(x)+P_1(1). The phase, P_1(1), is a pure CeRh phase with a Ce-environment with 100% Rh neighbors. The other phase, $P_1(x)$, is a $CeT_{0.2}Rh_{0.8}$ phase with T=Pd or Pt and a Ce-environment with an average of 80% Rh neighbors. This model results in the lowest weighted residual factor in both the Pt-compound (Rw = 5.6%) and the Pd-compound (Rw = 5.4%). See for example the difference in the data and fit indicated by a red line shifted down 4 units underneath the peaks shown in Figs. 6.3(a) and (b). The green line in Fig. 6.3(a) indicates a two-phase fit for the Pt-sample (with P_1=$CePt_{0.2}Rh_{0.8}$ and P_2=$Ce(Pt_{0.2}Rh_{0.8})_2$) resulting in Rw = 7.8%. In Fig. 6.3(b), the green line shows two-phase model (P_1+P_2) for the Pd-sample with (P_1=$CePd_{0.2}Rh_{0.8}$ and P_2=$CeRh_2$) with a residual weighted factor, Rw= 10.6%. The difference between the data and the two-phase fit, in both compounds, is indicated by a green wavy line shifted by 5 units below the peaks. A single-phase model (P_1) is also included for comparison indicated by a black line in both figures. The difference between data and a single-phase fit are represented by a wavy black line shifted down by 6 units resulting in a residual weighted factor values, Rw=11.3% for the Pt-alloys and Rw=12.4% for the Pd-alloys, respectively.

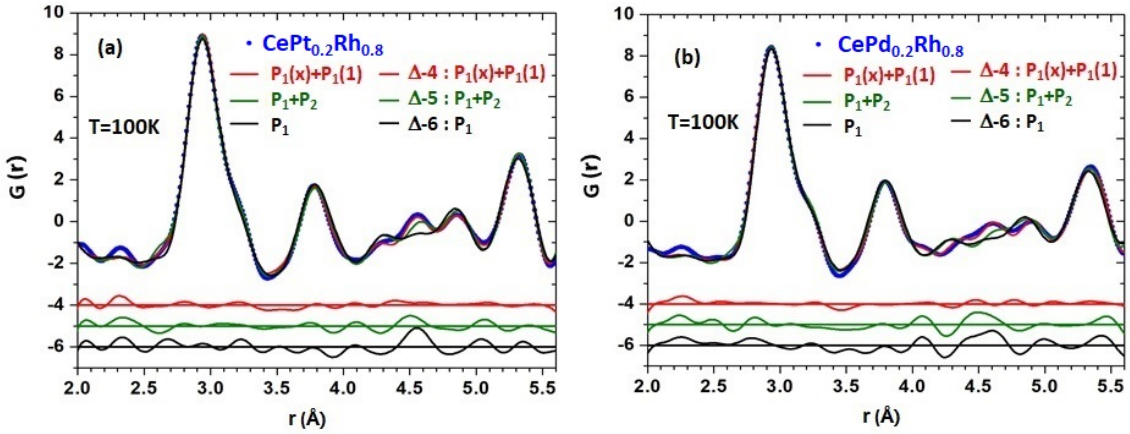

Figure 6.3: PDF of data (blue circles) at 100K of $CeT_{0.2}Rh_{0.8}$ for (a) T=Pt and (b) T=Pd with fit range $2\mathring{A} \leq r \leq 5.6\mathring{A}$. The red lines show a model with two different Ce-environments $(P_1(x) + P_1(1))$ where $P_1(x)$ is $CeT_{0.2}Rh_{0.8}$ and $P_1(1)$ is CeRh. The two-phase fit $(P_1 + P_2)$ and the single-phase fit (P_1) are marked by a green and black lines, respectively, where P_1 is $CeT_{0.2}Rh_{0.8}$ and P_2 is $Ce(Pt_{0.2}Rh_{0.8})_2$ in (a) and $CeRh_2$ in (b). The differences, Δ = data-fit are shown below with the same color.

This is a clear indication of two different local Ce-environments (Ce with mixed Rh and Pt/Pd neighbors with a probability given by the Rh concentration and another environment where Ce is completely surrounded by seven Rh atoms). The expected fraction of Ce atoms surrounded by seven Rh atoms at $x = 0.8$ is $0.8^7 \simeq 21\%$. The observed fraction of Ce atoms with seven Rh nearest neighbors from our best fit in Figs. 6.3(a) and (b) of $\sim 13\% - 24\%$ surprisingly matches the expected value.

6.2 Discussion

In this chapter, we have seen that the large reduction of the lattice parameter c and the increase in the isotropic ADP with x are mainly due to the Ce-Rh bond lengths variation in addition to the atomic size difference between Rh and Pd/Pt

atoms.

Assuming a simple model of two different bond lengths in $CePd_{1-x}Rh_x$ and $CePt_{1-x}Rh_x$ (short bond length d for Ce with seven Rh neighbors and longer bond length D if one or more of the seven Rh atoms are replaced by Pt/Pd), our prediction of the variation of the isotropic ADP (u_{Rh}) with the concentration of Rh matched the observed results using PDF analysis. For example, we successfully showed that the isotropic ADP of the Rh-site increases beyond ($x = 0.5$) and its maximum value is in the same order of magnitude as the value obtained from our PDF analysis. Isotropic atomic displacement parameter (u_{iso}) from PDFgui reflects variance of bond lengths. Sharp increase of $u_{iso}(x)$ for $x > 0.7$ signals that the number of nonmagnetic Ce atoms with Rh neighbors with shorter bond lengths become more relevant as the main cause for disorder.

By taking advantage of the power of the PDF analysis in controlling the length scale of interest, we investigate the local Ce-environment of our samples at the maximum Rhodium concentration ($x = 0.8$) by comparing different models within fit range $2\mathring{A} \leqslant r \leqslant 5.6\mathring{A}$. The model with Ce having two different local environments (i.e. Ce completely surrounded by seven Rh atoms and Ce with 20% chance having one or more Pt/Pd neighbors) gives superior result than even the two-phase model. This indicates that at higher Rh concentration, Ce has different local environment leading to substantial magnetic inhomogeneity and disorder.

In CeRh, strong hybridization makes Ce mixed valent (non-magnetic with effective valence of 3.2 instead of 3.0) [78]. This is recognized by seven "short" Ce-Rh bonds in our PDF analysis. Whereas, in CePt or CePd, weaker hybridization leaves the local f-electron with its magnetic moment less affected. If one or more of the seven

Rh neighbors of Ce is replaced by Pt/Pd, the bond lengths get longer and the Ce regains its magnetic moment.

In both the Pd- and the Pt-systems, at higher Rh concentration, the magnetic disorder is manifested by having different local Ce-environment as shown in Figs. 6.3(a) and (b). The tendency of the Pd-samples showing Griffiths phase [43] and the fact that the Pt-samples show cluster glass phase [19] towards the higher Rh concentration needs further magnetic and structural investigations.

Chapter 7

Summary and outlook

This dissertation presents a detailed study of the structural and magnetic properties of selected ferromagnetic alloys which can be driven to a paramagnetic phase by chemical substitution. The goal was to unravel the interplay between chemical and magnetic disorder close to a ferromagnetic quantum phase transition. I chose two series of alloys, the d-metal alloy $Ni_{1-x}V_x$ and the f-metal alloys $CePd_{1-x}Rh_x$ and $CePt_{1-x}Rh_x$, that presents signs of a disordered ferromagnetic quantum phase transitions.

In the first part of this thesis, I presented conclusive experimental evidence of a quantum Griffiths phase, expected for "disordered" quantum phase transition, in the d-metal alloy Ni-V. Such quantum Griffiths phase was recognized by magnetization data first on the paramagnetic side, later on the ferromagnetic side of the quantum phase transition. I applied the complementary method, μSR, and successfully extracted the relevant magnetic cluster contribution. This μSR analysis yields a similar cluster fraction consistent with the magnetization data and confirms that dynamic clusters are present close to the quantum critical point.

To trace the origin of these magnetic clusters and their distribution in $Ni_{1-x}V_x$, I investigated the chemical structure in detail on a powder sample. The structure characterization of our samples including the Ce-alloys was determined on data collected on NOMAD, a high resolution neutron powder diffractometer at the Spallation Neutron Source (SNS). I used in particular the local pair distribution function (PDF) as

the powerful tool to probe local atomic environments and discriminate between short range order and random displacements of the atoms. The PDF analysis confirmed that our Ni-V powder sample crystallize in the expected fcc-phase with random occupation of V and Ni. Comparison with alternative models (ordered phase models and V-cluster model) show that fcc-lattice is the best model when V and Ni are occupying the fcc-lattice sites at random. This indicates that the magnetic clusters we observed in our magnetic and μSR measurements are not created due to chemical clustering. Instead, they are formed from a random distribution of V atoms in the fcc-lattice.

The second part of my thesis focuses on the f-metal alloys $CePd_{1-x}Rh_x$ and $CePt_{1-x}Rh_x$. The ac-susceptibility and the structural data from the PDF analysis do not show any significant differences between the Pd- and the Pt-samples. For $x = 0.2$, they both show a sharp FM transition at $T_C \simeq 6$K. They crystallize in the same CrB-type structure with similar lattice parameters. However, small amount of different additional phases have been identified for the Pd-samples (Ce_3Pd_4) and for the Pt-samples ($Ce(Pt_{1-x}Rh_x)_2$).

Anomalies in the x-dependence of lattice parameters and atomic displacement parameters (ADP) could be resolved that are signs of disorder. A simple model of different bond lengths can explain the observed structural properties and the origin of magnetic inhomogeneities. For both compounds, we observed that the unit cell volume (in particular the c-axis) shrinks very rapidly towards higher Rh concentration and the isotropic ADP of the shared Rh and Pd/Pt site (u_{Rh}) increases beyond $x = 0.5$ rather than showing a maximum in the middle ($x = 0.5$). These are clear indications that the Ce-environment does not change homogeneously as the relevant coupling of f-electrons with the conduction electron mediated by the hybridization with the

direct neighbors might not result in the same Kondo temperatures for all Ce-atoms. The steady increase of $u_{Rh}(x)$ cannot be explained simply by the different Rh-Pd/Pt bond lengths expected with random Rh distribution. These changes are directly related to a strong variation in the bond lengths of the direct Ce-neighbors.

Like in CeRh, Ce with only Rh neighbors hybridizes strongly leading to a non-magnetic mixed-valent Ce state with a very short bond length. Other Ce with at least one Pt/Pd neighbor with a weaker hybridization are recognized with a longer bond. A simple model assuming two different bond lengths explains the change of variance with the given statistics assuming only random Rh occupation. We can even fit directly a narrow local environment of a pure CeRh phase and a mixed $CeT_{1-x}Rh_x$ (with T= Pd or Pt) with the expected statistics, confirming that local "impurities" of nonmagnetic Ce are created through random Rh occupation. We see that the strong bond lengths variation caused by random Rh occupation leads to a distribution of local Kondo temperatures and different magnetic environments. The strong magnetic inhomogeneities are responsible for a disorder-driven quantum phase transition. The tendency of the Pd-samples showing a Griffiths phase [43] and the fact that Pt-samples show a cluster glass phase [19] towards higher Rh concentrations needs further magnetic and structural investigation. We revealed that these magnetic impurities are related to stress and therefore responsible for further distortions. These might differ from Pd to Pt-system. We successfully demonstrated that magnetic disorder in CeRh-alloys can be accessed through local structural distortions.

However, there are still open questions that remain to be answered. The local structure of the main phase remains similar in the Pd- and Pt-system. The PDF analysis could be more sophisticated by comparing the evolution of "anisotropic"

ADP parameters in both systems since it can shed light on the magnetic anisotropy of the local Ce-sites. Magnetization $M(T, H)$ and resistivity $\rho(T, H)$ data on "single" crystals in different magnetic field (H) directions (and current directions) along crystallographic axes can also show global preferred spin directions and electronic (coupling) anisotropies. A study of crystalline electric field (CEF) excitation through neutron scattering could reveal the local anisotropy. A "magnetic" pair distribution function (mPDF) analysis would be the next challenge to investigate the local magnetic structure of our samples.

Gaining the direct information about the cluster size distribution in our Ni-V system was one of our goals in this project. We performed small angle neutron scattering experiments on NG7 SANS at NIST (with polarized and unpolarized neutron beam) and on GPSANS at HFIR, ORNL (with unpolarized neutron). Our preliminary results show that the small magnetic intensity can be resolved for samples on the FM side and a polarization analysis is feasible. The high background signal remains a major problem for low Q . Additional measurements with a broader scattering vector (Q) range at lower temperature look promising to reveal more details of the magnetic cluster distribution in Ni-V close to the quantum critical point.

Appendix A

Important instrument and lattice parameters

A.1 NOMAD specifications

Beam line	1B
Moderator	decoupled poisoned supercritical hydrogen
Moderator-to-sample distance	19.5 m
Sample-to-detector distance	$0.5 - 3m$
Wavelength range	$0.1 - 3\mathring{A}$
Momentum transfer range	$0.04 - 100\mathring{A}^{-1}$
Detector angular range	$3 - 175^0$ scattering angle
Initial range	4.0 steradian
Full detector complement	8.2 steradian
Flux on sample	$\sim 1 \times 10^8$ neutrons $cm^{-2}sec^{-1}$
Q_{broad}	$0.0191822\mathring{A}^{-1}$
Q_{damp}	$0.017659\mathring{A}^{-1}$

For more details see Ref. [4]

A.2 Lattice parameters of second phase $Ce(Pt_{1-x}Rh_x)_2$

x	a($\mathring{A}$)	$u_{Ce}(\mathring{A}^2)$	$u_{Rh}(\mathring{A}^2)$	δ_1	scale
0.2	7.62187	0.00440	0.00766	2.52	0.06
0.5	7.58643	0.00555	0.00744	2.40	0.10
0.6	7.56568	0.00623	0.00653	2.30	0.11
0.8	7.54369	0.00580	0.00697	2.00	0.10

Table A.1: PDF refined fit parameters of $Ce(Pt_{1-x}Rh_x)_2$ data obtained on NOMAD at 100K with fit range $r_{max} = 20\mathring{A}$, $Q_{max} = 24\mathring{A}^{-1}$, $Q_{damp} \simeq 0.018\mathring{A}^{-1}$, and $Q_{broad} \simeq 0.02\mathring{A}^{-1}$

A.3 Lattice parameters of second phase Ce_3Pd_4

x	a($\mathring{A}$)	$u_{Ce}(\mathring{A}^2)$	$u_{Pd}(\mathring{A}^2)$	δ_1	scale
0.2	8.08417	0.01335	0.00268	1.5	0.19
0.5	8.0391	0.02569	0.00433	1.5	0.34
0.6	7.9446	0.00738	0.00588	1.5	0.23
0.8	7.6087	0.02726	0.00724	1.5	0.07

Table A.2: PDF refined fit parameters of Ce_3Pd_4 data obtained on NOMAD at 100K with fit range $r_{max} = 20\mathring{A}$, $Q_{max} = 24\mathring{A}^{-1}$, $Q_{damp} \simeq 0.018\mathring{A}^{-1}$, and $Q_{broad} \simeq 0.02\mathring{A}^{-1}$. The second phase used for $x = 0.8$ is $CeRh_2$.

A.4 Periodic table of selected metallic elements

Element	Electronic configuration	Atomic mass(g/mol)
Ni	$[Ar]3d^8 4s^2$	58.69
V	$[Ar]3d^3 4s^2$	51.94
Ce	$[Xe]4f^1 5d^1 6s^2$	140.12
Pt	$[Xe]4f^{14} 5d^9 6s^1$	195.08
Pd	$[Kr]4d^{10} s^1$	106.42
Rh	$[Kr]4d^8 s^1$	102.91

References

[1] S. Ubaid-Kassis, T. Vojta, and A. Schroeder: Quantum Griffiths phase in the weak itinerant ferromagnetic alloy $Ni_{1-x}V_x$. *Phys. Rev. Lett.* **104**:(2010) 066402.

[2] R. Wang, A. Gebretsadik, S. Ubaid-Kassis, A. Schroeder, T. Vojta, P. J. Baker, F. L. Pratt, S. J. Blundell, T. Lancaster, I. Franke, J. S. Möller, and K. Page: Quantum Griffiths phase inside the ferromagnetic phase of $Ni_{1-x}V_x$. *Phys. Rev. Lett.* **118**:(2017) 267202.

[3] A. Schroeder, R. Wang, P. J. Baker, F. L. Pratt, S. J. Blundell, T. Lancaster, I. Franke, and J. S. Möller: Probing the magnetic phases in the Ni-V alloy close to the disordered ferromagnetic quantum critical point with μSR. *J. Phys. Conf. Series* **551**:(2014) 012003.

[4] Jörg Neuefeind, Mikhail Feygenson, John Carruth, Ron Hoffmann, and Kenneth K. Chipley: The Nanoscale Ordered Materials Diffractometer NOMAD at the Spallation Neutron Source SNS. *Nuclear Instruments and Methods in Physics Research Section B: Beam Interactions with Materials and Atoms* **287**:(2012) 68 – 75.

[5] D. T. Adroja, A. D. Hillier, J.-G. Park, W. Kockelmann, K. A. McEwen, B. D. Rainford, K.-H. Jang, C. Geibel, and T. Takabatake: Muon spin relaxation study of non-Fermi-liquid behavior near the ferromagnetic quantum critical point in $CePd_{0.15}Rh_{0.85}$. *Phys. Rev. B* **78**:(2008) 014412.

[6] J. C. Gomez Sal, J. I. Espeso, J. R. Fernandez, J. A. Blanco, and J. R. Carvajal: Crystallographic study and magnetic structures of $CeNi_xPt_{1-x}$ and diluted related compounds. *Solid State Communications* **87**:(1993) 863 – 868.

[7] S. Sachdev: Quantum phase transitions. *Physics World* **12**:(1999) 33.

[8] L. D. Landau: On the theory of the Fermi liquid. *Soviet Physics JETP* **35**:(1959) 70–74.

[9] H. v. Löhneysen, A. Rosch, M. Vojta, and P. Wölfle: Fermi-liquid instabilities at magnetic quantum phase transitions. *Rev. Mod. Phys.* **79**:(2007) 1015–1075.

[10] G. R. Stewart: Non-Fermi-liquid behavior in d- and f-electron metals. *Rev. Mod. Phys.* **73**:(2001) 797–855.

[11] J. G. Sereni, T. Westerkamp, R. Küchler, N. Caroca-Canales, P. Gegenwart, and C. Geibel: Ferromagnetic quantum criticality in the alloy $CePd_{1-x}Rh_x$. *Phys. Rev. B* **75**:(2007) 024432.

[12] M. Brando, D. Belitz, F. M. Grosche, and T. R. Kirkpatrick: Metallic quantum ferromagnets. *Rev. Mod. Phys.* **88**:(2016) 025006.

[13] C. Pfleiderer, G. J. McMullan, S. R. Julian, and G. G. Lonzarich: Magnetic quantum phase transition in MnSi under hydrostatic pressure. *Phys. Rev. B* **55**:(1997) 8330–8338.

[14] M. Uhlarz, C. Pfleiderer, and S. M. Hayden: Quantum phase transitions in the itinerant ferromagnet $ZrZn_2$. *Phys. Rev. Lett.* **93**:(2004) 256404.

[15] T. Vojta: Rare region effects at classical, quantum and nonequilibrium phase transitions. *Journal of Physics A: Mathematical and General* **39**:(2006) R143.

[16] D. L. Cox and A. Zawadowski: Exotic Kondo effects in metals: Magnetic ions in a crystalline electric field and tunnelling centres. *Advances in Physics* **47**:(1998) 599–942.

[17] E. Miranda and V. Dobrosavljevi: Disorder-driven non-Fermi liquid behaviour of correlated electrons. *Reports on Progress in Physics* **68**:(2005) 2337.

[18] E. D. Bauer, V. S. Zapf, P.-C. Ho, N. P. Butch, E. J. Freeman, C. Sirvent, and M. B. Maple: Non-Fermi-Liquid behavior within the ferromagnetic phase in $\mathrm{URu}_{2-x}\mathrm{Re}_x\mathrm{Si}_2$. *Phys. Rev. Lett.* **94**:(2005) 046401.

[19] I. Kawasaki, D. Nishikawa, H. Hidaka, T. Yanagisawa, K. Tenya, M. Yokoyama, and H. Amitsuka: Magnetic properties around quantum critical point of $\mathrm{CePt}_{1-x}\mathrm{Rh}_x$. *Physica B: Condensed Matter* **404**:(2009) 2908 – 2911.

[20] L. T. Backzewski: Magnetism in rare-earth-transition metal systems. magnetization reversal and ultra-high susceptibility in sandwiched thin films based on rare-earth and cobalt alloys. *Acta Physica Polonica A* **83**:(1993) 629–641.

[21] M. Cyrot, D. Gignoux, F. Givord, and M. Lavagna: Magnetism of the rare earth, 3d – Theoretical review. *Journal de Physique Colloques* **40**:(1979) C5–171–C5–176.

[22] S. Doniach: The Kondo lattice and weak antiferromagnetism. *Physica B+C* **91**:(1977) 231 – 234.

[23] J. Kondo: Resistance Minimum in Dilute Magnetic Alloys. *Progress of Theoretical Physics* **32**:(1964) 37–49.

[24] J. Kroha: Interplay of Kondo effect and RKKY interaction. *The Physics of Correlated Insulators, Metals, and Superconductors* **7**:(Jülich, 2017) 12.1–12.27. DOI `http://www.cond-mat.de/events/correl17`.

[25] P. Alekseev, A. Menushenkov, J.-M. Mignot, K. Nemkovski, A. Yaroslavtsev, and D. Kozlenko: Long Range Order and Spin-Fluctuations in Strongly Correlated Electron System with Valence Instability. *Physics Procedia* **71**:(2015) 303 – 307.

[26] E. Miranda, V. Dobrosavljevic, and G. Kotliar: Kondo disorder: a possible route towards non-Fermi-liquid behaviour. *Journal of Physics: Condensed Matter* **8**:(1996) 9871.

[27] D. Gignoux and J. C. Gomez-Sal: Competition between the Kondo effect and exchange interactions in the $CeNi_xPt_{1-x}$ compounds. *Phys. Rev. B* **30**:(1984) 3967–3973.

[28] T. Vojta: Phases and phase transitions in disordered quantum systems. In A. Avella and F. Mancini, editors, *Lectures On The Physics Of Strongly Correlated Systems XVII*. AIP Publishing, Melville, 2013, 188–247.

[29] D. Nozadze: *Quantum Phase Transitions In Disordered Magnets*. Ph.D. thesis, Missouri University Of Science and Technology, 2013.

[30] M. Vojta: Quantum phase transitions. *Reports on Progress in Physics* **66**:(2003) 2069.

[31] H. E. Stanley: *Introduction to Phase Transitions and Critical Phenomena*. Oxford Science Publications, 1987.

[32] A. J. Millis: Effect of a nonzero temperature on quantum critical points in itinerant fermion systems. *Phys. Rev. B* **48**:(1993) 7183–7196.

[33] A. B. Harris: Effect of random defects on the critical behavior of Ising models. *Journal of Physics C: Solid State Physics* **7**: 1671.

[34] T. Vojta: Quantum Griffiths effects and smeared phase transitions in metals: theory and experiment. *J. Low Temp. Phys.* **161**:(2010) 299.

[35] R. B. Griffiths: Nonanalytic Behavior Above the Critical Point in a Random Ising Ferromagnet. *Phys. Rev. Lett.* **23**:(1969) 17–19.

[36] T. Vojta and J. Schmalian: Quantum Griffiths effects in itinerant Heisenberg magnets. *Phys. Rev. B* **72**:(2005) 045438.

[37] N. W. Ashcroft and N. D. Mermin: *Solid State Physics*. Saunders, 1976.

[38] S. Julian: The normal states of magnetic d and f transition metals. *J Phys.: Conds. Matt.* **8**:(1996) 9675–9688.

[39] A. J. Schofield: Non-Fermi liquids. *Contemporary Physics* **40**:(1999) 95–115.

[40] P. Fulde: Introduction to the theory of heavy fermions. *Journal of Physics F: Metal Physics* **18**:(1988) 601.

[41] J. Friedel: Metallic alloys. *Nuovo Cimento* **7**:(1958) 287–311.

[42] A. Gebretsadik, R. Wang, A. Alyami, J.-G. Lussier, A. Schroeder, and K. Page: Study of chemical disorder in $Ni_{1-x}V_x$. *to be published* .

[43] M. Brando, T. Westerkamp, M. Deppe, P. Gegenwart, C. Geibel, and F. Steglich: Quantum Griffiths phase in $CePd_{1-x}Rh_x$ with $x \simeq 0.8$. *Journal of Physics: Conference Series* **200**:(2010) 012016.

[44] V. Shaginyan, E. Kirichenko, and V. Stephanovich: Quantum critical point in $CePd_{1-x}Rh_x$ ferromagnet. *Physica B: Condensed Matter* **403**:(2008) 755 – 757.

[45] A. P. Pikul, N. Caroca-Canales, M. Deppe, P. Gegenwart, J. G. Sereni, C. Geibel, and F. Steglich: Non-Fermi-liquid behaviour close to the disappearance of ferromagnetism in $CePd_{1-x}Rh_x$. *Journal of Physics: Condensed Matter* **18**:(2006) L535.

[46] D. Adroja, J.-G. Park, K.-H. Jang, H. Walker, K. McEwen, and T. Takabatake: Study of non-Fermi-liquid behaviour near the ferromagnetic quantum critical point in $CePd_{0.15}Rh_{0.85}$. *Journal of Magnetism and Magnetic Materials* **310**:(2007) 858 – 860.

[47] J. Larrea J., M. B. Fontes, A. D. Alvarenga, E. M. Baggio-Saitovitch, T. Burghardt, A. Eichler, and M. A. Continentino: Quantum critical behavior in a CePt ferromagnetic Kondo lattice. *Phys. Rev. B* **72**:(2005) 035129.

[48] I. Kawasaki, K. Tenya, M. Yokoyama, and H. Amitsuka: Quantum critical phenomena of ferromagnetic $CePt_{1-x}Rh_x$. *Physica B: Condensed Matter* **403**:(2008) 1284 – 1286.

[49] M. Deppe, P. Pedrazzini, N. Caroca-Canales, C. Geibel, and J. Sereni: Investigations of $CePd_{1-x}Rh_x$ single crystals located near a ferromagnetic quantum critical point. *Physica B: Condensed Matter* **378-380**:(2006) 96 – 97.

[50] S. Ubaid-Kassis: *Magnetization and Transport Study of Disordered Weak Itinerant Ferromagnets*. Ph.D. thesis, Kent State University, 2009.

[51] D. S. Sivia: *Elementary Scattering Theory For X-ray and Neutron Users*. Oxford University Press, 2011.

[52] G. Shirane, S. M. Shapiro, and J. M. Tranquada: *Neutron Scattering with a Triple-Axis Spectrometer*. Cambridge University Press, 2002.

[53] A. P. Hammersley, S. O. Svensson, and A. Thompson: Calibration and correction of spatial distortions in 2D detector systems. *Nucl. Instr. Meth.* **12**:(1994) 312–321.

[54] T. Heitmann and W. Montfrooij: *Practical Neutron Scattering at a Steady State Neutron Source*. Mizzou Media, 2012.

[55] T. Proffen, K. L. Page, M. E. Sylvia, C. Bjorn, T. W. Darling, and J. A. TenCate: Atomic pair distribution function analysis of materials containing crystalline and amorphous phases. *Zeitschrift für Kristallographie - Crystalline Materials* **220**:(2005) 1002–1008.

[56] T. Proffen, S. J. L. Billinge, T. Egami, and D. Louca: Structural analysis of complex materials using the atomic pair distribution function - a practical guide. *Zeitschrift für Kristallographie - Crystalline Materials* **218**:(2003) 132–143.

[57] C. L. Farrow, P. Juhas, L. J. W., D. Bryndin, E. S. Bozin, J. Bloch, T. Proffen, and S. J. L. Billinge: *PDFgui user Guide*, 2 edition, 2016. DOI `http://stacks.iop.org/0953-8984/19/335219`.

[58] A. C. Larson and R. B. V. Dreele: General Structure Analysis System (GSAS). *Los Alamos National Laboratory Report* :(2000) LAUR 86–748.

[59] B. H. Tobby: EXPGUI, a graphical user interface for GSAS. *J. Appl. Cryst* **34**:(2001) 210–213.

[60] S. J. Blundell: Spin-polarized muons in condensed matter physics. *Contemporary Physics* **40**:(1999) 175–192.

[61] P. Dalmas de Reotier and A. Yaouanc: Muon spin rotation and relaxation in magnetic materials. *Journal of Physics: Condensed Matter* **9**:(1997) 9113.

[62] A. Yaouanc and P. Dalmas de Reotier: Muon spin rotation, relaxation, and resonance: Applications to condensed matter. *Int. Ser. Monogr. Phys.* **147**:(2011) 1–486.

[63] F. L. Pratt: WIMDA: a muon data analysis program for the Windows PC. *Physica B: Condensed Matter* **289-290**:(2000) 710 – 714.

[64] R. S. Hayano, Y. J. Uemura, J. Imazato, N. Nishida, T. Yamazaki, and R. Kubo: Zero- and low-field spin relaxation studied by positive muons. *Phys. Rev. B* **20**:(1979) 850–859.

[65] F. Bölling: Ferro- und paramagnetisches Verhalten in den Mischkristallen des Nickels mit Vanadium, Rhodium und Platin im Temperaturbereich von 14° bis 1000^oK . *Phys. Kondens. Mater.* **7**:(1968) 162–184.

[66] J. Smith, O. Carlson, and P. Nash: The Ni-V (Nickel-Vanadium) system. *Journal of Phase Equilibria* **3**:(1982) 342–348.

[67] T. Proffen, T. Egami, S. Billinge, A. Cheetham, D. Louca, and J. Parise: Building a high resolution total scattering powder diffractometer – upgrade of NPD at MLNSC. *Appl. Phys. A* **74**:(2002) s163–s165.

[68] H. A. Moreen, R. Taggart, and D. H. Polonis: Ni_8X phases in the systems Ni-V, Ni-V-Nb, and Ni-V-Ta. *Journal of Materials Science* **6**:(1971) 1425–1432.

[69] R. Wang, S. Ubaid-Kassis, A. Schroeder, P. J. Baker, F. L. Pratt, S. J. Blundell, I. F. T. Lancaster, J. S. Möller, and T. Vojta: Evidence for magnetic clusters in $Ni_{1-x}V_x$ close to the quantum critical concentration. *Journal of Physics: Conference Series* **592**:(2015) 012089.

[70] A. Gebretsadik, J.-G. Lussier, A. Schroeder, and K. Page: Structural disorder study of Ce(Rh, T) across the ferromagnetic quantum phase transition. *to be published* .

[71] A. Janghorban, M. Lomello-Tafin, J.-M. Moreau, and P. Galez: The phase diagram of the Ce–Pt system. *Intermetallics* **18**:(2010) 2208.

[72] H. Okamoto and T. B. Massalski: Binary alloy phase diagrams requiring further studies. *Journal of Phase Equilibria* **15**:(1994) 500–521.

[73] A. Palenzona, F. Canepa, and P. Manfrinetti: Phase diagram of the Ce-Rh system. *Journal of Alloys and Compounds* **194**:(1993) 63 – 66.

[74] W. Zachariasen: *Acta Cryst* **2**:(1949) 388–390.

[75] C. L. Farrow, P. Juhas, J. W. Liu, D. Bryndin, E. S. Bozin, J. Bloch, T. Proffen, and S. J. L. Billinge: Pdffit2 and pdfgui: computer programs for studying nanostructure in crystals. *J. Phys. Condens. Matter* **19**:(2007) 335219.

[76] G. Barberis, B. Roden, P. Weidner, L. Gupta, D. Davidov, and I. Felner: Intermediate valence effects in the magnetic behaviour of $Ce(Pt_{1-x}Rh_x)_2$ laves phase compounds. *Solid State Communications* **42**:(1982) 659 – 665.

[77] I.-K. Jeong, R. H. Heffner, M. J. Graf, and S. J. L. Billinge: Lattice dynamics and correlated atomic motion from the atomic pair distribution function. *Phys. Rev. B* **67**:(2003) 104301.

[78] J. Lawrence: Intermediate valence metals. *Modern Physics Letters B* **22**:(2008) 1273–1295.